

Conceptual Design Report

Hall C 12 GeV/c Upgrade

Hall-C Collaboration

November 27, 2002

Hall C 12 GeV Upgrade Conceptual Design Report

J.R. Arrington, K. Hafidi, R.J. Holt, D.H. Potterveld, P.E. Reimer
Argonne National Laboratory, Argonne, IL

C. Carlson, M. Finn, C.F. Perdrisat, J. Roche
College of William and Mary, Williamsburg, VA

P. Markowitz, J. Reinhold, M. Sargsyan
Florida International University, Miami, FL

O.K. Baker, M.E. Christy, P. Gueye, C.E. Keppel, L. Tang, A.R. Uzzle
Hampton University, Hampton, VA

I. Niculescu
James Madison University, Harrisonburg, VA

A. Afanasev, P. Brindza, R. Carlini, R. Ent, H.C. Fenker, M. Fowler, M.K. Jones
S.R. Lassiter, A.F. Lung, D.J. Mack, D.G. Meekins, W. Melnitchouk, A. Radyushkin,
G. Smith, W.F. Vulcan, B. Wojtsekhowski, S.A. Wood, C. Yan
Jefferson Lab, Newport News, VA

D. Dutta, H. Gao
Massachusetts Institute of Technology, Cambridge, MA

J. Cha, J.A. Dunne
Mississippi State University, Mississippi State, MS

V. Punjabi
Norfolk State University, Norfolk, VA

A. Ahmidouch, S. Danagoulian, A. Gasparian
North Carolina A&T, Greensboro, NC

P. Stoler
Rensselaer Polytechnic Institute, Troy, NY

D. Gaskell, E.R. Kinney
University of Colorado, Boulder, CO

A. Nathan
University of Illinois, Urbana-Champaign, IL

P. Bosted
University of Massachusetts, Amherst, MA

E.J. Brash, G. Huber
University of Regina, Regina, SK, Canada

J. Mammei
University of Texas-El Paso, El Paso, TX

D. Crabb, D.B. Day, P. McKee, O.A. Rondon, G. Warren
University of Virginia, Charlottesville, VA

H.P. Blok

Vrije Universiteit, Amsterdam, Netherlands

A. Aghalaryan, R. Asatryan, H. Mkrtchyan, S. Stepanyan, V. Tadevosyan
Yerevan Physics Institute, Yerevan, Armenia

Contents

1	Introduction	1
2	Executive Summary	3
2.1	Physics Overview	3
2.2	Summary of Experimental Equipment	13
2.2.1	Small Angles and Large Momenta at High Luminosity	13
2.2.2	Precision Cross Section Measurements and L-T Separations	15
2.2.3	Background Rejection and Particle ID	16
2.2.4	Summary	16
3	Physics Motivation and Examples	17
3.1	Introduction	17
3.2	Transition from Hadronic to Partonic Structure	17
3.2.1	pQCD and Constituent Scaling	17
3.2.2	Helicity Conservation	20
3.3	Structure Functions	21
3.3.1	F_1 and F_2 at Low Q^2 and Moderate x	22
3.3.2	Structure Functions at Higher x and Quark-Hadron Duality	23
3.3.3	Spin Structure Functions	25
3.3.4	Semi-Inclusive Duality and Factorization	27
3.4	Exclusive Reactions and Generalized Parton Distributions.	29
3.4.1	High t Structure Functions and GPD's	30
3.4.2	Low t GPDs	32
3.5	The Nucleus as a Laboratory	33
3.5.1	Color Transparency	33
3.5.2	$x > 1$ and Superfast Quarks	34
3.5.3	Nuclear Broadening	36
3.6	Search for New Physics	37
4	Spectrometer Systems	40
4.1	Overview	40
4.2	The High Momentum Spectrometer	41
4.3	The Super High Momentum Spectrometer	44
4.3.1	Overview	44
4.3.2	The SHMS Magnets and Structural Design	44

4.3.2.1	General	44
4.3.2.2	Q1 at 8.6 T/m	46
4.3.2.3	QD30 Superconducting Magnet for the SHMS	47
4.3.2.4	Magnet DC Power and Energy Dump System	49
4.3.2.5	Magnet Control System	52
4.3.2.6	Support Structure	53
4.3.2.7	Spectrometer Motion System	53
4.3.2.8	Shield House	54
4.3.2.9	SHMS Cryogenic System	55
4.3.2.10	SHMS Vacuum Systems	56
4.3.3	SHMS Optics and Monte Carlo	57
4.3.4	SHMS Performance (Resolution/Acceptance)	65
4.3.5	SHMS Detector Systems	72
4.3.5.1	Wire Chambers	72
4.3.5.2	Quartz Čerenkov Hodøscope	76
4.3.5.3	Particle Identification	78
4.3.5.4	Focal Plane Polarimeter	89
4.3.5.5	Trigger, Data Acquisition, and Online Computing	89
4.3.5.6	Stand-Alone (Third-Arm) Calorimeter	92
5	Ancillary Equipment	93
5.1	Beam Line	93
5.1.1	Overview	93
5.1.2	Absolute Beam Energy Measurements at 12 GeV	93
5.1.3	Beam Position and Current Monitoring at 12 GeV	94
5.1.4	Beam Raster	95
5.1.5	Møller Polarimeter	96
5.1.6	Compton Polarimeter	97
5.1.7	Polarized Target Chicane	98
5.2	Target Systems and Infrastructure	99
5.2.1	Cryogenic Targets	99
5.2.2	Solid Targets	100
5.2.3	Scattering chamber	100
5.2.4	Solid Polarized H and D Target	101
5.2.5	Conceptual Design for a Polarized ^3He Target in Hall C	102
5.2.6	General Hall Infrastructure	105
Bibliography		106
Appendices		
A	Detailed Cost Estimates	109
B	Project Timeline	110
C	List of Figures	111

D List of Tables	114
E Projected Physics Results (available in Internal Report Only)	115

Chapter 1

Introduction

At a 12-GeV Jefferson Lab, Hall C will provide the only magnetic spectrometer, the Super High Momentum Spectrometer (SHMS), powerful enough to detect charged particles with momenta approaching that of the highest energy beam. Together with its companion, the existing High Momentum Spectrometer (HMS), this will make Hall C the only facility in the world capable of studying (deep) exclusive reactions at the highest momentum transfers, $Q^2 \simeq 15$ (GeV/c)², with appropriate high luminosity. By extension, only Hall C will be able to fully exploit semi-exclusive reactions in the critical region where the electroproduced hadron carries almost all of the energy transfer.

At such high beam energies secondary particles are boosted into the forward detection hemisphere. Therefore, the SHMS is designed to achieve angles down to 5.5°, and up to 25°. The SHMS will have a solid angle of 2-4 msr, and a large momentum and target acceptance. The existing HMS complements SHMS well, with a solid angle of up to 10 msr, an angular range between 10.5° and 90°, and a maximum momentum of 7.3 GeV/c.

Hall C's magnetic spectrometer pair will be rigidly connected to a central pivot which permits both rapid, remote angle changes and reproducible rotation characteristics which simplify accurate measurements, including Rosenbluth-type separations. From its inception, the SHMS momentum and target acceptances were designed to be both large and nearly uniform, allowing for both fast and accurate data collection. The SHMS could operate at an unprecedented luminosity of 10^{39} electron-atoms/s/cm², with a 40% momentum acceptance.

The large momentum acceptance, in combination with the large luminosity, will enable the measurement of the smallest cross sections, and allow for a complete map of the nucleon's response from elastic scattering to deep inelastic scattering. The latter will greatly facilitate studies in the transition region from hadronic to quark-gluon degrees of freedom, including a novel determination of the spin and flavor dependence of low-energy quark-hadron duality and hadronization. The final product of these experiments will be a precise determination of the lowest moments of quark distributions for $Q^2 \leq 10$ (GeV/c)², both spin- and flavor-dependent, providing a direct connection with Lattice QCD calculations.

Hall C will also retain its general infrastructure to offer collaborations an opportunity to do one-of-a-kind experiments, with dedicated experimental setups. Already at 6 GeV, the experimental program in Hall C will provide for the capability of 2-kW cryogenic target running, the use of an \approx 100-msr electromagnetic calorimeter, and a focal-plane polarimeter suited for both HMS and SHMS operation at 12 GeV. Examples of key physics shown in the

remainder of this document assume beam times ranging between one and three months.

Chapter 2

Executive Summary

2.1 Physics Overview

Three decades after the establishment of QCD as the theory of the strong nuclear force, understanding how QCD works remains one of the great puzzles in nuclear physics. One major challenge arises from the fact that the degrees of freedom observed in low-energy phenomenology (mesons and nucleons) are totally different from those appearing in the QCD Lagrangian (current quarks and gluons). The remarkable and unique feature of QCD at large distance — quark confinement — prevents the individual quark and gluon constituents of the nucleon from being removed and examined in isolation.

The property of QCD known as asymptotic freedom, in which quarks interact weakly at short distances, allows one to calculate hadronic observables at high energies perturbatively in terms of expansions in the strong coupling constant, α_s . This has made possible precise characterizations of deep inelastic lepton scattering from hadrons. The resulting structure functions are naturally described by the momentum distributions of quarks and gluons in the infinite momentum frame. These experiments first revealed the existence of quarks and, indirectly, gluons in the nucleon, and have now determined the quark-gluon momentum and helicity distributions in great detail. Perturbative QCD is crucial in extracting these distributions, but is useless for the deeper challenge of calculating the experimental distributions from first principles, or for understanding the wide range of applicability of a simple quark level description of deep inelastic scattering.

A major aim of the 12-GeV experiments in Hall C is to provide detailed snapshots of the nucleon structure at various levels of resolution. Deep inelastic scattering provides the highest level of resolution, mapping the probability for finding the various constituents (partons) in a hadron as a function of x , the fraction they carry of the hadron's overall momentum. Our current knowledge of the regime $x \approx 1$, where a single constituent is responsible for the entire, or, in a nucleus, *more than the entire*, momentum of the proton, is totally inadequate. At the same time, lower resolution, but more global, snapshots will be provided by measuring elastic and transition form factors, which describe the overall distribution of charge and magnetism of nucleons and baryonic resonances. Here, the quarks and gluons are found to interact with one another exceedingly strongly, such that their individual identities are obscured. Thus, to make substantial progress in understanding strongly interacting matter

requires detailed knowledge of the structure of the basic building blocks of hadrons and nuclei, and to understand the connection of this structure to the current quarks and gluons appearing in the QCD Lagrangian.

A recent experiment at Jefferson Lab found the charge and magnetization distributions in the proton to be drastically different. This very clear and startling discovery has stimulated new theoretical attempts to describe the nucleon form factors. These measurements need to be extended to higher momentum transfer to see if this dramatic and unexpected difference continues to the highest resolution attainable at 12 GeV. It is important to note the flexibility of the Hall C experimental setup here: the HMS focal-plane polarimeter will be installed in the SHMS to reach the highest values of momentum transfer squared, $Q^2 = 14$ (GeV/c) 2 .

Figure 2.1 shows one example of an exclusive scattering measurement of the lowest-lying excited state of the nucleon, the delta (Δ) resonance. Many modern QCD-inspired models attempt to describe the detailed structure of this state. At low energies, the Δ resonance is excited predominantly by magnetic dipole radiation, with electric quadrupole excitation becoming significant at higher energies. An accurate measurement of the contribution of this quadrupole excitation of the nucleon is of great importance in understanding the nature of the forces between the quarks. In fact, at the very highest energies this quadrupole excitation is expected to be dominant! Figure 2.1(left) shows the Q^2 range of measurements of the magnetic nucleon-delta transition form factor, whereas Fig. 2.1(right) shows the ratio of quadrupole to magnetic dipole strength of this transition, under the assumption that this ratio remains small ($\ll 1$).

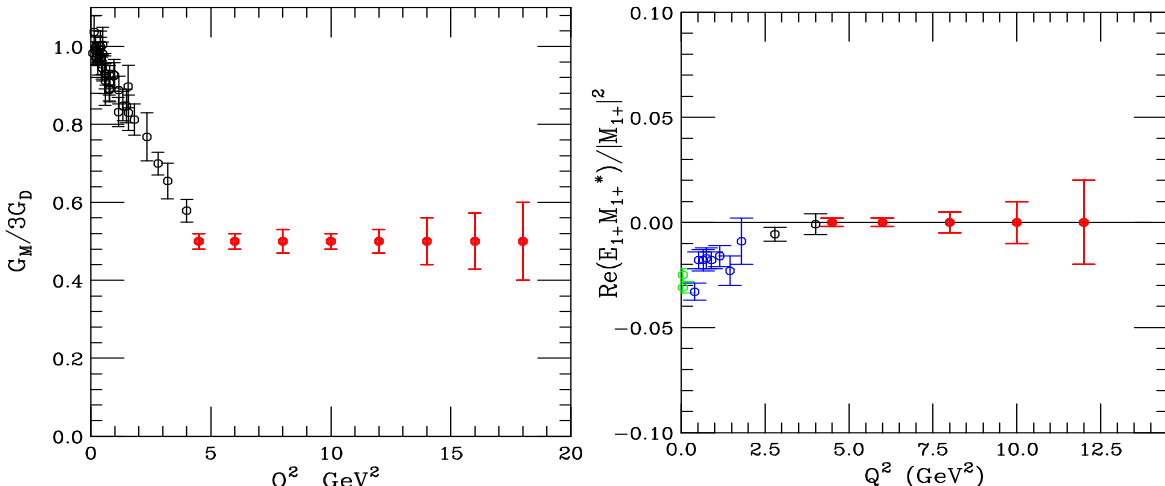


Figure 2.1: Left: The Magnetic Form Factor of the Nucleon-Delta Transition, scaled by the dipole form factor $G_D = 1/(1 + Q^2/0.71)$. Red circles are projected data using the HMS-SHMS magnetic spectrometer combination. Right: The ratio of electric quadrupole to magnetic dipole strengths for the excitation of the delta resonance. Green circles are photoexcitation data (Mainz and BNL), blue circles are JLab-CLAS data, black circles are JLab-Hall C data, and red circles show the projected range and uncertainties for JLab-Hall C.

A significant theoretical advance in describing the quark-gluon structure of hadrons is the identification of *Generalized Parton Distributions* (GPDs). Probed primarily in exclusive measurements, the GPDs describe hard scattering processes that involve the correlations

between partons. This new formalism offers an exciting bridge between elastic and deep inelastic scattering: in different kinematic limits of the GPDs, one recovers the familiar elastic form factors and deep inelastic structure functions of the nucleon. Clearly, a mature description of the partonic substructure of the nucleon, beyond the naive picture of collinear non-interacting quarks, must involve a description of these partonic correlations. Indeed, Fourier transforms of the GPDs can be related to impact parameter dependent parton distributions, which offers the prospect of obtaining a full, three-dimensional snapshot of the nucleon. Further, GPDs have a direct connection to the presently unknown parton orbital angular momentum, which is an essential contribution to the total spin of the nucleon. Experimentally, exclusive scattering measurements at large Q^2 and small t (the momentum transfer squared between the initial and final hadron), — so-called deep-exclusive scattering — are just beginning. On the other hand, exclusive form factor-type measurements at large t are well within reach at 12 GeV. The unique capabilities of Hall C at 12 GeV — a large final-state momentum at small scattering angle, coupled with high luminosity — will make possible the highest- Q^2 reactions for single charged particle detection.

The parton distributions under scrutiny in deep inelastic scattering give detailed information on the probability to find partons with longitudinal momentum fraction x . In contrast, form factors constitute $\langle x^n \rangle$ moments of GPDs, and access both the transverse and longitudinal parton distributions. The program of exclusive measurements possible in Hall C at 12 GeV will unambiguously provide data to the highest Q^2 for the pion form factor, the proton electric and magnetic form factors, the $N \rightarrow \Delta$ and $N \rightarrow S_{11}$ transitions (the S_{11} is the negative parity partner of the nucleon), and Real Compton Scattering. The latter process, $\gamma p \rightarrow \gamma p$, constitutes the $\langle x^{-1} \rangle$ moment of the same GPD constraining the Dirac form factor F_1 (which is the $\langle x^0 \rangle$ moment). Presently, precise measurements above Q^2 of a few $(\text{GeV}/c)^2$ are only available for the proton magnetic form factor.

Hall C will not be able to completely map out the GPDs at all values of x , as this would require a far higher-energy high-luminosity facility. Thus, complete information on the exact role of orbital angular momentum may not be possible yet. However, Hall C will be able to deliver the following important GPD constraints:

- Nucleon elastic and transition form factors up to $Q^2 \simeq 15 (\text{GeV}/c)^2$,
- Real Compton Scattering up to $s \simeq 20 \text{ GeV}^2$,
- Exclusive pion and kaon electroproduction up to $Q^2 \simeq 10 (\text{GeV}/c)^2$, including precise longitudinal-transverse separations and spin-dependent measurements.

The various processes constraining GPDs will provide an important spin-isospin filter. The unique role of nucleon-resonance transition form factors is that they isolate different isospin combinations of GPDs. In hard electroproduction of mesons, the spin of the produced meson dictates the type of GPD involved. This gives access to polarized parton densities without the need for target polarization. Finally, the flavor dependence of the GPDs can be studied by comparing, *e.g.*, charged pion and kaon electroproduction from the proton, leaving the residual state as either a neutron or a Λ . To scrutinize the GPDs constitutes an ambitious but rewarding goal of the future electron scattering program!

In addition, Hall C will deliver checks on the validity of the factorization proofs associated with the experimental access to GPDs, by both verifying the Q^2 -dependence of longitudinal

and transverse cross sections, and hunting for the appearance of Color Transparency. Color Transparency states that the mesons produced in the hard scattering process should have wave functions close to their asymptotic form. In this condition, the two quarks, each of which would normally interact very strongly with nuclear matter, form an object that passes undisturbed through the nuclear medium. A similar phenomenon occurs in QED, where an e^+e^- pair of small size has a small cross section determined by its electric dipole moment. In QCD, a $q\bar{q}$ or qqq system can act as an analogous small color dipole moment.

Hall C would allow for searches for Color Transparency in the $A(e,e'\pi)$ reaction up to $Q^2 = 14 \text{ (GeV/c)}^2$, well above the threshold of $Q^2 \approx 5\text{-}10 \text{ (GeV/c)}^2$ which is considered sufficient for the applicability of the factorization proofs. In addition, in the $A(e,e'p)$ reaction, Color Transparency searches are possible up to $Q^2 = 18 \text{ (GeV/c)}^2$, considerably beyond the $Q^2 \simeq 12 \text{ (GeV/c)}^2$ threshold where $A(p,2p)$ experiments at BNL see an enhancement (and subsequent decrease) in nuclear transparency.

Although firm predictions from perturbative QCD for the parton distributions in the asymptotic limit exist, they are not very revealing and rather uninteresting from the nucleon structure point of view. Similarly, there are firm predictions from perturbative QCD for the behavior of hadronic form factors at large Q^2 (where the form factors directly measure quark distribution amplitudes), although the scale at which this behavior should become visible is *a priori* unknown (*e.g.*, the ratio in Fig. 2.1(right) is expected to become unity in the asymptotic limit). A deeper understanding of hadron structure will rather come with the determination of the dynamics that drive the transition from long distance scales (low Q^2 , where confinement dominates and the interaction is strong) to short distance scales (high Q^2 , where the quarks act as if they are free), which will provide a far richer catalog of strong interaction phenomena. The pion is the simplest QCD system available for study of this nonperturbative to perturbative behavior in the *preasymptotic* region, and is the best hope for seeing this transition experimentally.

One of the highest priorities for the Hall C program is then to pin down the pion form factor F_π as accurately as possible, to values of Q^2 greater than 6 (GeV/c)^2 . Since F_π is manifested in the longitudinal pion electroproduction cross section, one must carry out a longitudinal-transverse separation, and project as closely as possible to the *non-physical* pion pole. The high momentum pions will be detected at very forward angles by the SHMS spectrometer. Figure 2.2 shows how the proposed 12-GeV Upgrade can explore this transition.

In the preasymptotic region, one also expects to witness interference effects between short-distance and long-distance scale processes. This interference effect is termed QCD oscillations, and is analogous to the QED effect of Coulomb-nuclear interference observed in low-energy charged-particle scattering. In QCD, the hard-scattering amplitude interferes with a long-distance process due to soft gluon radiation. This effect is speculated to explain the striking oscillation observed around the predicted quark counting rule behavior in high energy proton-proton and pion-proton scattering. It may also be related to the production of charm resonance states. There is enormous interest in confirming whether such oscillations are a general feature of QCD (a similar phenomenon could be the cause of the rise and subsequent decrease of the $A(p,2p)$ transparency results discussed earlier). The exclusive pion photoproduction process can be mapped out to $s = 22 \text{ GeV}^2$, transcending the region below and above the charm production threshold, as illustrated in Fig. 2.3.

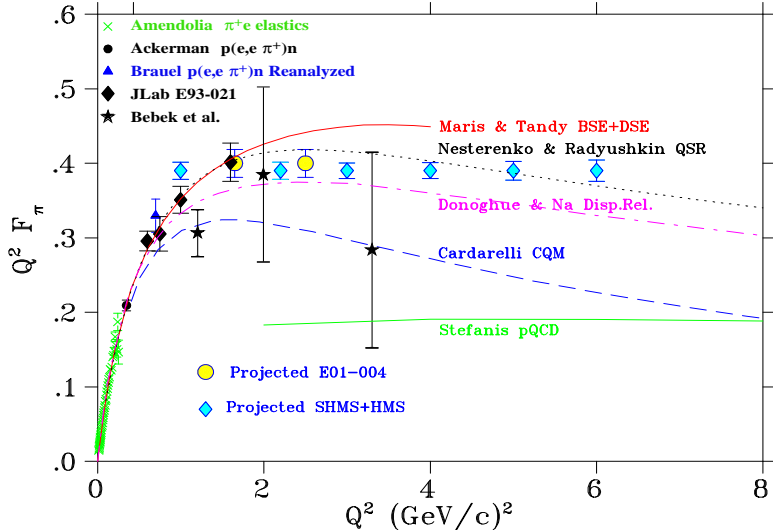


Figure 2.2: Projections for Measurements of the π^+ Elastic Form Factor with the HMS-SHMS Combination, ranging from confinement-dominated to perturbative-dominated quark-gluon dynamics. Green crosses denote results from elastic pion-atomic electron scattering. Recent Hall C data are denoted by filled diamonds. Blue diamonds denote 12-GeV projections. The curves represent model calculations of this transition.

The onset of the preasymptotic region can also be studied using the notion of quark-hadron duality. In principle, QCD should describe the physics of hadrons and nuclei over all distance scales: quark-hadron duality implies that all physical phenomena must be described in terms of complementary, complete sets of quark-gluon or hadronic states. Through asymptotic freedom, the behavior of structure functions at high energies can be understood in terms of electron scattering from free quarks. At lower energies the effects of confinement become more visible, and the structure functions become dominated by the production of a small number of nucleon resonances. One would naively expect the steep Q^2 dependence of the nucleon-resonance transition form factors (see also Fig. 2.1(left)) to produce large deviations from the asymptotic freedom limit. However, recent experiments in Hall C have demonstrated that, when averaged over an appropriate energy range, the hadronic cross section nevertheless coincides with the naive quark level result. Therefore, quark-hadron duality also addresses the central issue of how the transition from strongly interacting matter to perturbative QCD is realized.

A 12-GeV beam in Hall C will make accessible the broad kinematic region required to map out both the resonance and deep inelastic regimes requisite to a number of inclusive duality and structure function studies. Presently, little to no inclusive spectra in the resonance region exist above $Q^2 \approx 8$ $(\text{GeV}/c)^2$, data which will be easily obtainable in Hall C at 12 GeV, where the structure function F_2 can be measured to $Q^2 \simeq 20$ $(\text{GeV}/c)^2$. Longitudinal-transverse separated data, necessary to determine the F_1 and F_L structure functions individually, will be available up to $Q^2 = 12$ $(\text{GeV}/c)^2$. Further, spin-dependent data will be available up to $Q^2 = 10$ $(\text{GeV}/c)^2$.

In combination with the existing inclusive scattering data accumulated over the last thirty

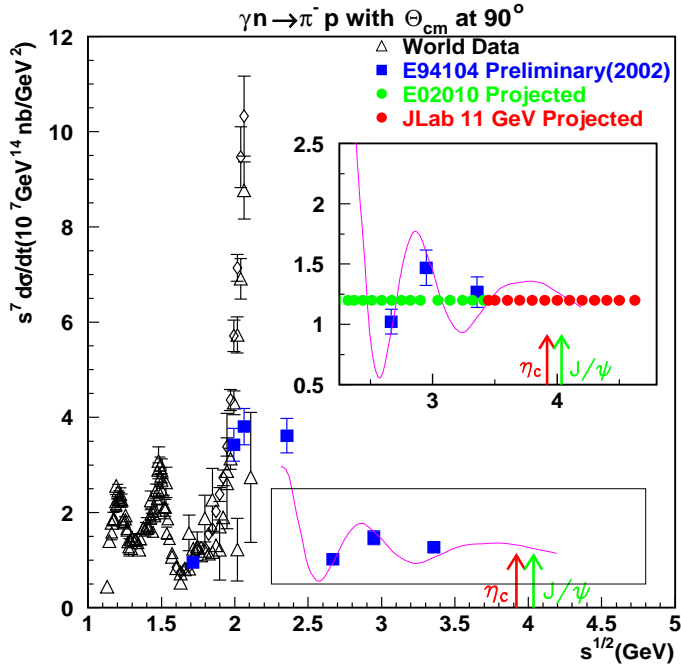


Figure 2.3: Projections for Measurements of the $\gamma n \rightarrow \pi^- p$ Process at a Center-of-Mass Angle of 90° . The HMS-SHMS combination is required to measure the high-momentum pion and proton. Open triangles are the existing world data. Blue squares are preliminary JLab data. The green (red) circles show the range possible with a 6-GeV (12-GeV) JLab beam energy. The purple oscillatory curve shows the anticipated effect of QCD oscillations. The arrows indicate the threshold of charm production.

years at various high-energy lepton-scattering laboratories in the world, which have typically emphasized the low x region, these data can be used to obtain moments of all polarized and unpolarized structure function data with unprecedented precision, up to $Q^2 \simeq 10$ (GeV/c) 2 . Fig. 2.4 shows the quality of the data for the lower moments of $F_2^p - F_2^n$ that will be accessible in Hall C, compared with recent Lattice QCD calculations. The advent of multi-Teraflops computing will enable these moments to be calculated over the next few years with $\sim 5\%$ accuracy. Advances in Lattice techniques, combined with the increased computing power, will in addition enable the individual F_2^p and F_2^n structure function moments to be evaluated. By accessing smaller quark masses, the new generations of lattice simulations will also remove the large systematic uncertainty currently associated with the chiral extrapolation of the lattice moments. Comparisons of the experimental moments with those calculated on the lattice over a range of Q^2 between ≈ 1 and 10 GeV 2 will allow one to determine the size of higher twist corrections and the role played by quark-gluon correlations in the nucleon.

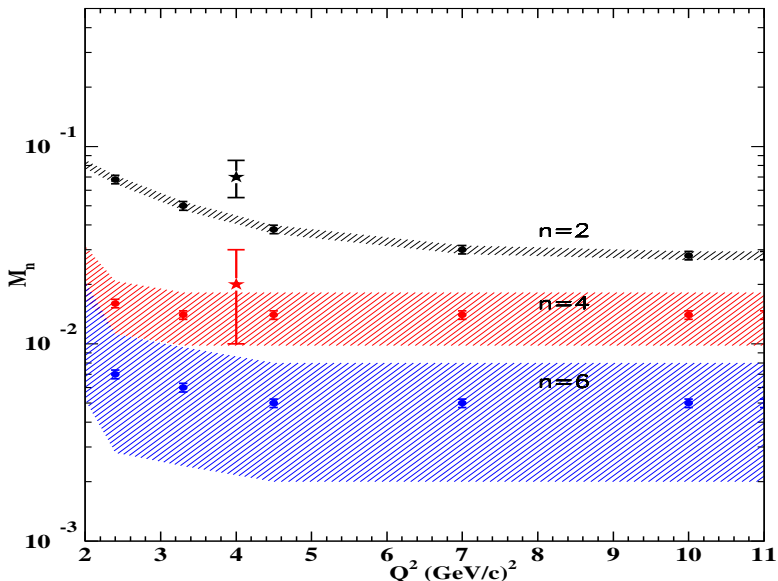


Figure 2.4: Lowest Moments of the Structure Function Difference $\int_0^1 x^{n-2} (F_2^p - F_2^n) dx$ for $n = 2$ (black), 4 (red), and 6 (blue), as a function of Q^2 . Lattice QCD calculations (stars) are added at $Q^2 = 4$ (GeV/c) 2 for $n = 2$ (black) and 4 (red). Experimental moments without including JLab data are indicated as hatched areas. The 12-GeV program will obtain precise moments for $Q^2 \leq 10$ (GeV/c) 2 , for all polarized and unpolarized (e,e') structure functions.

A revolutionary application of duality would be to render accessible the region of very high x , which has not been attainable in any other experiment. The region of $x \approx 1$ is an important testing ground for mechanisms of spin-flavor symmetry breaking in the valence quark distributions of the nucleon. Presently, little or no polarization data exists in the region of $x > 0.5$, where the valence quarks, which give the overall charge and baryon number of the nucleon, are dominant. Using appropriate averaging over resonances, this region can be precisely mapped out up to $x \approx 0.9$.

It is vital for our understanding of duality and its practical exploitation that the spin

and flavor dependence of duality be established empirically. The latter would also allow a more detailed investigation of fragmentation functions, providing another snapshot of nucleon structure. These fragmentation functions map how a struck quark evolves into a hadron (hadronization). This process also appears in an astrophysical context, as part of the transition from a deconfined state of free quarks and gluons in the Big Bang into stable protons, providing the seeds for nuclear synthesis. At present, our understanding of the hadronization process is rudimentary at best.

Close and Isgur predict that one may expect hadronization and approximate duality to work at $Q^2 < 3 \text{ (GeV/c)}^2$ and relatively low energy transfer, well within the range of the JLab at 12-GeV kinematics. However, it is only possible to investigate this prediction by selecting electroproduced pions or kaons with energies close to the energy transfer. The HMS-SHMS setup is optimally suited to answer these questions experimentally.

In addition to experiments involving free hadrons, nuclear targets will play an important role in that the nucleus both uniquely provides a filter for investigating the substructure of hadrons via the phenomenon of Color Transparency (mentioned earlier), and a localized higher nuclear density region that may give rise to distortions of the nucleon substructure.

At extremely high temperature or density, matter is expected to undergo a phase transition wherein quarks and gluons are no longer confined within hadrons and instead form a quark-gluon plasma. While ordinary nuclear densities are well below the expected phase transition, local fluctuations in density can occur within nuclei when nucleons are close together. Measurements for $x > 1$ at extremely high Q^2 no longer probe the nucleon distributions, but instead measure the distribution of “superfast” quarks within nuclei. As these superfast quarks carry a momentum fraction larger than a single nucleon would be expected to carry, they can only occur when multiple nucleons share momentum. By extracting the distribution of superfast quarks within nucleon clusters, we can look for the onset of deconfinement which may manifest itself as nucleon “swelling” – the merging of two nucleons into a 6-quark cluster as one approaches the phase transition.

In this respect, studies at JLab at 12 GeV will nicely complement the study of the high-temperature region of the phase diagram of nuclear matter (planned at RHIC via relativistic heavy-ion collisions and at the LHC in proton-proton collisions) with the exploration of the low-temperature, high-density phase (see Fig. 2.5). Experimentally, one can only access this region at large values of x and Q^2 . Such large x distributions, *e.g.*, at $x = 2$ and $Q^2 = 10 \text{ (GeV/c)}^2$, involve the extreme tails of the quark distribution functions, and very small cross sections, which can be accessed at a beam energy of 12 GeV only with the high luminosity and good acceptance and resolution properties of the Hall C detector package.

In addition to mapping out the transition to deconfinement as one approaches chiral restoration, Hall C will also probe the behavior of cold, dense hadronic matter (up to 3-4 times nuclear matter densities in the region where nucleons overlap). This is also the region of temperature and density relevant to understanding the equation of state of neutron stars and to the study of the possible transition from neutron stars to “quark stars”.

Finally, a 12-GeV upgrade will allow for a search for physics beyond the Standard Model. Parity-violation experiments are under way or planned at SLAC and JLab in electron scattering reactions with other electrons (SLAC-E158) or with protons (JLab-QWeak). The results of these measurements could reveal the existence of previously unobserved heavy particles which may be responsible for the parity-violating character of the weak interaction. Alter-

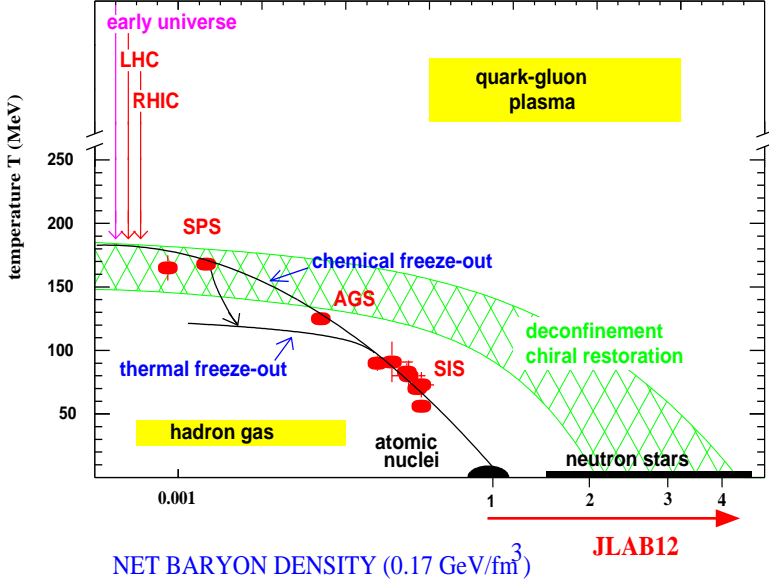


Figure 2.5: Phase Diagram for Nuclear Matter.

natively, they could test for the presence of another symmetry, termed “supersymmetry”, which predicts the existence of a very heavy partner particle for each of the currently known elementary particles.

The Hall C infrastructure in existence or planned for a series of 6-GeV experiments, beam polarimetry with $<1\%$ uncertainty and a 2-kW cryotarget capability, in combination with the large target length and momentum acceptances of HMS and SHMS, would allow for a search for physics beyond the Standard Model in deep inelastic scattering from a deuterium target. The experiment would search for deviations from the predicted variation (running) of the weak mixing angle θ_W with Q^2 .

Presently, there are only a few measurements of $\sin^2 \theta_W$ away from $Q^2 = M_Z^2$. The proposed deep inelastic scattering parity violation (DIS-Parity) experiment is complementary to both the planned SLAC-E158 and JLab-QWeak experiments in its sensitivity to extensions of the Standard Model. A combination of these measurements would give a beautiful experimental illustration of our understanding of the running of this electroweak coupling constant. Figure 2.6 shows the present and projected results of measurements of $\sin^2 \theta_W$ as a function of Q .

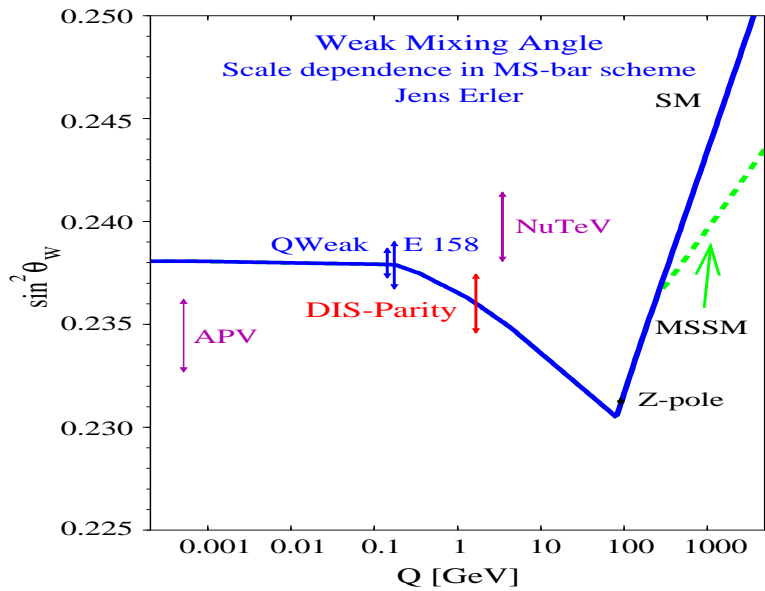


Figure 2.6: The Running of $\sin^2 \theta_W$ Shown as a Function of Q . The proposed combined statistical and systematic precision of the deep inelastic scattering parity violation experiment at JLab (DIS-Parity) is shown in red. Also shown are the existing Atomic Parity Violation (APV) Cesium data and neutrino DIS (NuTeV) measurements, along with expected uncertainty of the approved JLab-QWeak and ongoing SLAC-E158 Møller experiments.

2.2 Summary of Experimental Equipment

Rapid scientific advances require apparatus with forefront capabilities. The JLab community has made dramatic scientific advances since 1995 when multi-GeV, high current, CW electron beams became available for the first time. To use these beams effectively, high power cryotargets and large magnetic spectrometers were constructed. Subsequently, polarized beam and polarized targets greatly expanded the physics reach of the facility. Specialized stand-alone detectors such as vector and tensor polarimeters, electromagnetic calorimeters, and neutron TOF walls further enriched the program.

The JLab upgrade will increase the maximum beam energy in Hall C to 10.9 GeV. High beam current, polarized beam, polarized targets, and stand-alone detectors will still be available, as will be the immense expertise associated with the corresponding support groups. The existing High Momentum Spectrometer (HMS) will also be available. With a maximum momentum of over 7 GeV/c, an angle range of 10°-90°, and the largest acceptance of any existing focusing spectrometer in the multi-GeV regime, the HMS is ready for the upgrade. If 10.9-GeV beam were available now, the HMS could immediately begin a program of single-arm (e, e') measurements at high Q^2 and high x_B . The missing piece of forefront technology is a second high energy magnetic spectrometer for coincidence studies.

With the increase in average beam energy of the upgrade, reaction products will generally move to smaller angles and have higher momenta. Furthermore, QED tells us that the cross sections will generally be smaller, and errors in reconstruction of the \vec{q} -vector must be even more tightly controlled. Particle identification becomes more difficult because most reaction products are moving close to the speed of light.

With the above facts in mind, we have designed a new spectrometer, a complementary companion to the existing HMS, called the Super High Momentum Spectrometer (or SHMS). With this new spectrometer, Hall C will possess both the luminosity and flexibility to carry out a “must do” physics program of small cross section, ($e, e' \text{hadron}$) coincidence experiments in which the hadron carries a large fraction of the beam energy.¹

2.2.1 Small Angles and Large Momenta at High Luminosity

We have optimized the SHMS design to reach scattering angles as small as 5.5° at the full beam momentum in order to access a rich program of high z hadron electroproduction. The prototype experiments in this group are the measurement of the **charged pion form factor** and the search for **color transparency in $A(e, e' p)$** . These two experiments set the minimum angle and maximum momentum requirements, respectively, of the SHMS. Other important experiments which could be run in the same configuration are listed in Table 2.1. Because the small scattering angles are achieved by using a large drift between the target and the first quadrupole, the solid angle in this Small Solid Angle (SSA) configuration is a modest 2 msr. However, the acceptances in momentum and projected target length are very large. The detector package will be instrumented for 30 cm in Y_{target} and a 40% momentum bite. Up to 50 cm of useful Y_{target} acceptance is available if an experiment can provide the larger focal plane instrumentation.

¹This is also referred to as the high z region, where $z = E_{\text{hadron}}/\nu$ and ν is the electron energy loss. “Hadron” here refers to an essentially stable particle like a π^\pm , k^\pm , p, d, etc.

Table 2.1: The Hall C Experimental Program at 12 GeV and the Associated Apparatus Requirements.

Experiment	Reaction	Kinematic Regime	Configuration e-h	Comments
Coincidence:				
Charged Pion Form Factor	$N(e, e' \pi^\pm) N$	low $-t$, scan Q^2	HMS•SHMS(SSA)	L-T separation
Soft-Hard Factorization Tests	$N(e, e' \pi^\pm) N$	fix (x_B, t) , scan Q^2	"	L-T separation
Polarized GPD's \tilde{E} and \tilde{H}^a	$N(e, e' \pi^\pm) N$	fix (x_B, t)	"	polarized H and 3He ,
Color Transparency I	$A(e, e' \pi^\pm)$	scan Q^2	"	L-T separation helpful
Color Transparency II	$A(e, e' p)$	quasi-free, scan Q^2	"	L-T separation helpful
Hadronization Factorization Test	$N(e, e' \pi^\pm) N$	fix (x_B, z)	"	beam momentum protons
Baryon Transition Form Factors	$p(e, e' p) \pi^0$	fix W , scan θ_{cm} , Q^2	HMS•SHMS(LSA)	good proton resolution
Exclusive π^- Photoproduction	$d(\gamma, \pi^- p) p_s$	fix s , scan θ_{cm} , and fix θ_{cm} , scan s	"	high momentum π, p
Nuclear Filtering	$A(\gamma, \pi^- p)$	fix θ_{cm} , scan s	"	high momentum π, p
Proton Electric Form Factor	$p(e, e' p)$	scan Q^2	Big Cal•HMS or SHMS(LSA)	FPP, EM calorimeter
Exclusive π^0 Photoproduction	$p(d(\gamma, p\pi^0)$	fix s , scan θ_{cm} , and fix θ_{cm} , scan s	Big Cal•HMS	EM calorimeter
Singles:				
Superfast Quarks	$A(e, e') X$	high x_B and Q^2	SHMS(SSA)+HMS	small cross-section
Unpolarized Structure Functions	$p, d(e, e') X$	scan x_B, Q^2	"	L-T separation
PV DIS Standard Model Test	$d(e, e') X$	moderate x_B and Q^2	SHMS(LSA)+HMS	$\leq 1\%$ Q^2 determination,
Spin Structure Functions	$\vec{p}, \vec{d}(e, e') X$	scan x_B and Q^2	"	$\leq 1\%$ accuracy beam polarimetry,
Exclusive π^+ Photoproduction	$p(\gamma, \pi^+) n$	scan s, θ_{cm}	"	2 kWatt LD_2 Cryotarget
Inclusive π^-/π^+ Photoproduction	$d(\gamma, \pi^\pm) X$	fix s, θ_{cm}	"	polarized H and D, Chicane
				hadron photoproduction
				hadron photoproduction

^aContingent upon results of Soft-Hard Factorization Tests

By moving the magnet and detector string closer to the target on a linear track, we will be able to double the solid angle to 4 msr (the Large Solid Angle or LSA configuration). The LSA configuration allows the SHMS to accommodate experiments which require high momentum capability yet which prefer to trade-off small angle coverage and maximum momentum for increased solid angle. The prototype experiments for this configuration are the **baryon transition form factor** and **proton electric form factor** programs.

While the transition between the SSA and LSA configurations could be made in hours, this would probably only be done once per block of experiments. The spectrometer offsets would have to be redetermined, and it is also likely that the optics reconstruction would have to be reoptimized (due to millimeter-level changes in the relative alignment of the magnets). The latter is a particularly time-consuming process for large acceptance devices employing high order optics.

The ability to make measurements at high luminosity is important for a physics program which strives to measure increasingly smaller cross sections. Except for polarized targets, which have serious beam current limitations, the majority of experiments will be able to take the maximum available beam current.

2.2.2 Precision Cross Section Measurements and L-T Separations

Because cross sections in electron scattering experiments change rapidly with momentum transfer, it is critical to know the absolute beam energy and scattering angle. The beam energy will be determined to $\pm 0.05\%$ using the upgraded 3C arc. The nominal spectrometer angles, determined by surveyed marks on the floor, should reflect the true scattering angle within a few milliradians. Small angle offsets between the nominal spectrometer angle and the true scattering angle are measured using over-determined $e + p$ elastic scattering. The hard-coupling of the SHMS to a central pivot means that, like the present HMS, these small angle offsets will be reproducible. Furthermore, angles can be changed in *minutes*, and time-consuming surveys of the spectrometer are not normally required, even after significant angle changes. Because of this, at the start of the **parity violation in deep inelastic scattering (PVDIS)** experiment, the absolute angles of the HMS and SHMS will already be known at the milliradian level, and this can be improved with further dedicated $e + p$ elastic scattering measurements.

The SHMS was designed from the outset for precision measurement of cross sections. For a relatively large momentum bite of $\pm 10\%$ and Y_{target} acceptances of 15 cm, the SHMS acceptance is flat within a few percent. (The acceptance of the existing HMS is almost as impressive.) The two mentioned critical features, hard-coupling to the pivot and the large, flat acceptances, mean that the HMS-SHMS pair will become the premier instrument in the world for making L-T separations at multi-GeV beam energies. The ability to perform L-T separations is not only critical for the charged pion form factor measurement, but for any experiment which seeks to access GPD information in pseudoscalar meson electroproduction.

The vast majority of experiments at JLab could be successfully carried out with an accuracy of 1 mrad in scattering angle and 0.1% in momentum. The SHMS is designed to provide resolution consistent with these needs, but with careful calibration it is of course possible to obtain accuracy better than the resolution. We believe the resolution of the SHMS is nearly optimal for the planned physics program.

2.2.3 Background Rejection and Particle ID

Hall C obtained extensive experience in making low signal/noise measurements during the $x > 1$ and deuteron photodisintegration experiments. Important lessons learned were the value of hermetic shielding of the detector hut, a clean trigger for hadrons, and constraining the fitted reconstruction matrix elements so as not to map tracks from outside of the acceptance back into the acceptance. As in the present Hall C analysis code, detector pixel hits can be correlated with wire chamber tracking information, providing PID information for each track in the case of multiple tracks. These lessons have been (or will be) applied to the design of the SHMS and will be critical for future aggressive high x_B and high energy hadron photoproduction measurements. A permanent shield house will completely encapsulate the detector hut and the large QD magnet. The lowest level trigger, a coincidence between the S1 and S2 hodoscopes, will be insensitive to low energy backgrounds because at least one of the hodoscope arrays will be constructed of quartz rather than scintillator.

Electron detection in experiments at **high x_B** such as the $x > 1$ experiment will be very clean. In addition to tracking information there will be at least 7 hits in the detector stack: 2 scintillator elements, 2 quartz Čerenkov elements, 2 gas Čerenkov telescopes, and an electromagnetic calorimeter. Mis-identification of pions as electrons due to the production of knock-on electrons will be minimized since the atmospheric pressure gas Čerenkov can be the first detector element seen by the scattered particles, and the thickness of the hodoscope preceding the second gas Čerenkov will be minimized as well.

Hadrons are more difficult to cleanly detect and identify than electrons; they (or their daughters) also have the ability to penetrate through the Tungsten collimator and meters of steel or concrete shielding. Hadrons do not produce light as efficiently as electrons in lead glass, and they will only trigger a gas Čerenkov at very high momenta. Nevertheless, for the SHMS **exclusive pion photoproduction** measurements, in addition to tracking information there will always be at least 5 hits in the detector stack: 2 scintillator elements, 2 quartz Čerenkov elements, and a heavy gas Čerenkov telescope. The HMS will have similar capability after installing a quartz Čerenkov in front of the lead-glass calorimeter.

2.2.4 Summary

At 12 GeV, the SHMS will provide access to qualitatively new regions of phase space (small scattering angles and large momenta) which would not be accessible to the existing HMS. This complementarity makes possible measurements at high luminosity for a wide range of exclusive and semi-exclusive reactions. As a core-spectrometer facility for the 12-GeV program, the SHMS will possess the ability to efficiently make clean and accurate measurements with excellent particle identification over the full momentum range.

Chapter 3

Physics Motivation and Examples

3.1 Introduction

In this section we expand on the basic physics motivation of the Hall C upgrade program as outlined in the executive summary section. In doing so, we maintain continuous connection with the basic themes of our program: the transitions from hadronic to quark-gluon degrees of freedom, and from the soft (long range) to the hard (short range) structure of the nucleon. We propose to obtain a three dimensional picture of the nucleon in its full complexity. We also explore hadronic structure and interactions within the nuclear medium. Finally, we present an opportunity to help elucidate the question of the evolution of the weak mixing angle θ_W .

3.2 Transition from Hadronic to Partonic Structure

3.2.1 pQCD and Constituent Scaling

At very high momentum transfer (Q^2 , or $-t$), exclusive reactions are expected to access the small spatial configurations consisting only of the valence quarks, which perturbatively exchange the minimum number of gluons necessary to keep the entire hadron intact. Our goal is not so much to reach this asymptotic *hard* state, but to observe the evolution to it from the more complex and interesting hadronic structures.

A well known signature for the onset of perturbative QCD (pQCD) is *constituent scaling*. The reaction for which pQCD is expected to manifest this at the lowest momentum transfer is in elastic scattering from the charged pion, since the pion has the simplest valence quark structure. There has been a large number of calculations of the pion form factor, F_π , which predict its magnitude and Q^2 dependence [1, 2, 3, 4, 5]. In one extreme the calculations involve purely perturbative mechanisms utilizing simple valence quark distributions which either have asymptotic shapes or those based upon QCD sum rules. Other calculations add higher non-perturbative configurations in various ways. The most recent theoretical studies of the charged pion form factor F_π seem to indicate that these hard exclusive processes may be expected to become important by $Q^2 \sim 5$ (GeV/c) 2 . To date, the most accurate measurements of F_π have been carried out in Hall C to a maximum Q^2 of around 1.6 (GeV/c) 2

[6]. Not surprisingly, these results do not exhibit the $1/Q^2$ scaling predicted by pQCD. One of the highest priorities for the Hall C program is to measure F_π as accurately as possible to the highest Q^2 possible, which will be possible to values greater than 6 (GeV/c)^2 . The goal is to observe the transition to constituent scaling, and also to pin down the magnitude of the cross section, which constrains valence non-perturbative models, and their higher twist corrections. Since F_π is manifested in the longitudinal cross section, one must carry out a Rosenbluth separation, and project as closely as possible to the *non-physical* pion pole. The combination of the SHMS and HMS spectrometers is ideal for such a separation. The high momentum pions will be detected at very forward angles by the SHMS spectrometer, in coincidence with the electrons detected in the HMS spectrometer. Results of various theoretical calculations are shown in Fig. 3.1.

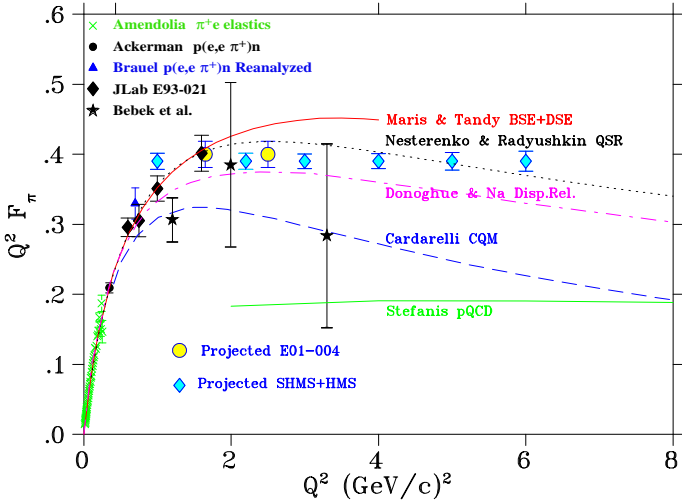


Figure 3.1: The π^+ Form Factor. Recent Hall C data are denoted by black diamonds. Blue diamonds denote 12-GeV projections. Other available data are shown as well. The curves are the results of theoretical calculations.

For the case of baryons, constituent scaling is expected at higher Q^2 than for F_π . However, there is a great deal of contradictory data regarding the transition to this behavior, and where exactly it begins [7]. Some experiments, such as the proton magnetic form factor G_{Mp} , exhibit a “precocious” scaling at momentum transfers as low as a few $(\text{GeV}/c)^2$. Others show that expected quark counting rules are not yet satisfied at more moderate momentum transfers. Recent JLab experiments have given rise to vigorous speculation about the mechanisms involved in these disparate measurements.

For example, in the $p \rightarrow S_{11}(1535)$ transition, the helicity conserving amplitude is expected to scale with Q^2 as $Q^3 A_{1/2} \rightarrow \text{constant}$. Experiments at the current JLab energy do not show the onset of constituent scaling up to $Q^2 \sim 3.5 \text{ (GeV/c)}^2$. With the 12-GeV upgrade, the maximum obtainable Q^2 will be almost 15 $(\text{GeV}/c)^2$. In this measurement, the electron is detected by the HMS in coincidence with the protons in the SHMS from the $S_{11} \rightarrow p + \eta$ decay channel, and the η is reconstructed via its missing mass. The SHMS is ideally suited for the detection of the recoil protons since they emerge at a forward angle with high momentum. Likewise, the leading amplitude in the $p \rightarrow \Delta(1232)$ does not show any indication of the onset of scaling. Another example which is not so clear is the result of the Hall C experiment on deuteron photodisintegration, which, curiously, exhibits scaling at nucleon emission angle of 90° for photon energy as low as 1 GeV, and may exhibit scaling at larger nucleon emission angles for high k_t . The onset of scaling for deuterium is expected

to be at even higher t than for single nucleons.

At higher W , the phenomena of exclusive pion photoproduction shows a rich and interesting behavior both as functions of s and t . For example, the exclusive π^+ cross section has been known for a long time to roughly follow the $1/s^7$ behavior predicted by the constituent counting rules, as shown in the left side of Fig. 3.2, and the t dependence appears scale very well with the s . However, there is an observed oscillation around the $1/s^7$ dependence whose origin is not yet understood, but speculated to be an interference effect between long and short distance phenomena [8]. This effect is analogous to Coulomb-nuclear interference in low-energy charged-particle scattering, a QCD analog of a QED effect. In this case, a hard-scattering amplitude interferes with a long-range part due to soft gluon radiation (Coulombic part). It is expected to be a general QCD phenomenon, and the s and t dependence will be studied with greater range and improved statistical accuracy in Hall C out to $s \approx 22$ (GeV)². Moreover, it will be possible to measure exclusive π^- (shown on the right hand side of Fig. 3.2) photoproduction from the neutrons inside nuclear targets. The coincident $D(\gamma, \pi^- p)$ measurements require two spectrometers capable of reaching high momenta of about 6.5 GeV/c, making these measurements ideal for the HMS-SHMS spectrometer pair in Hall C. In addition, π^0 photoproduction will also be measured using a spectrometer for proton detection in coincidence with the large in-place calorimeter for detection of the π^0 decay photons. The higher energy π^0 data will extend the range of s from the current maximum of 9 GeV² to 22 GeV², with good statistical precision. The necessary high luminosity for all of these measurements will be achieved by using a bremsstrahlung photon beam and LH2 and LD2 targets.

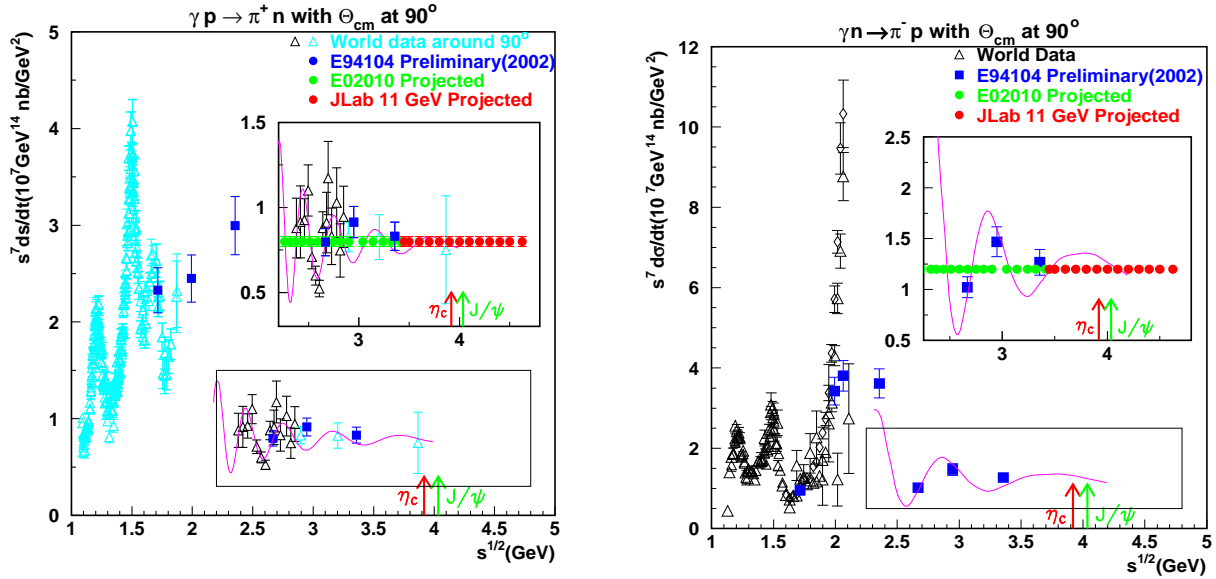


Figure 3.2: The Scaled Cross Section $s^7 d\sigma/dt$ for the reactions $p(\gamma, \pi^+)n$ (left) and $n(\gamma, \pi^-)p$ (right) at $\theta = 90^\circ$, vs s . The existing data are shown in comparison to the 11-GeV projected data in the top inserts, and preliminary new data in the bottom inserts. Note that the new high energy data will straddle the $c\bar{c}$ and J/ψ thresholds.

3.2.2 Helicity Conservation

Although constituent scaling is a necessary condition for the onset of pQCD, it is not sufficient, and other non-perturbative processes appear to be able to account for the *scaling-like* phenomena at realistically achievable momentum transfers. One of the primary signatures of the onset of the hard pQCD processes is helicity conservation. The reactions which have tested helicity conservation at JLab were: the measurements of the ratio of elastic scattering form factors $Q^2 F_{1p}/F_{2p}$, which is expected to approach a constant with increasing Q^2 ; the electric to magnetic multipole amplitude ratio E_{1+}/M_{1+} for the $p \rightarrow \Delta$ transition, which is expected to approach unity with increasing Q^2 ; and the transverse recoil polarization of wide angle Compton scattering. None of these reactions at current JLab kinematics have yet displayed pQCD behavior, but it is expected that they will at an energy-upgraded JLab.

Current measurements of the elastic form factor ratio $\mu G_{Ep}/G_{Mp}$ reach a maximum Q^2 of about 5.6 (GeV/c) 2 , as shown in Fig. 3.3 [9]. These data depict an unexpected and markedly different Q^2 dependence for the two form factors, in contrast to the constant pQCD prediction for the ratio. For the measurement in Hall C with the energy upgrade it is estimated that a maximum Q^2 of 14 (GeV/c) 2 can be reached with good precision, as also shown in Fig. 3.3. The experiment will use either the HMS or SHMS spectrometer, equipped with the same focal plane polarimeter, to measure the momentum of the recoiling proton, and the polarization transfer. The scattered electrons will be detected in a large existing electromagnetic calorimeter. Only the SHMS spectrometer could achieve the highest Q^2 point.

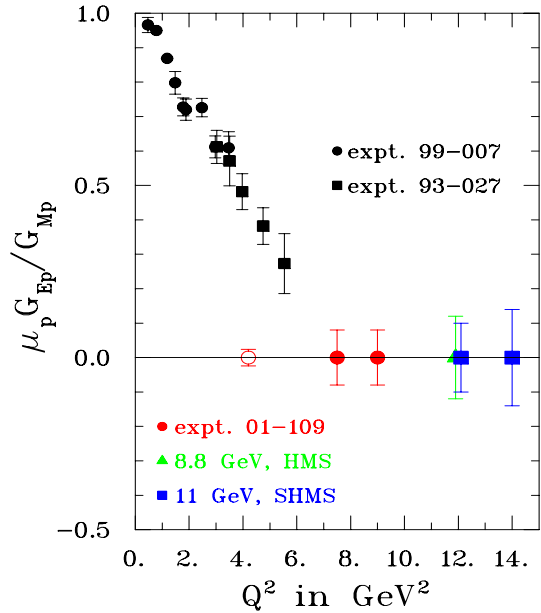


Figure 3.3: Existing and Approved JLab Measurements of the ratio $\mu G_{Ep}/G_{Mp}$, out to $Q^2 \approx 5.6$ (GeV/c) 2 , and the projected $Q^2 = 12$ and 14 -(GeV/c) 2 data in Hall C with electron beam energy of 11 GeV (statistical uncertainties only).

At low Q^2 , the $p \rightarrow \Delta$ transition must be spin flip and therefore helicity non-conserving, reflected in the present value near zero of the E_{1+}/M_{1+} dipole ratio shown in Fig. 3.4. In high Q^2 pQCD electron-quark scattering, however, helicity must be conserved and this measurement must tend toward unity. The $p \rightarrow \Delta$ transition, therefore, provides a dramatic testing ground for the transition from hadronic to partonic degrees of freedom, as depicted by the curve on the left hand side of Fig. 3.4. The new Hall C measurements should extend

the limits of this measurement from the current value of 4 (GeV/c)^2 to $\approx 12 \text{ (GeV/c)}^2$. This experiment measures the high momentum, forward angle recoil proton from the decay of the Δ with the SHMS, and the electron with HMS. The emerging π^0 is then reconstructed by missing mass. Finally, in wide-angle Real Compton Scattering the longitudinal recoil momentum asymmetry A_{LL} measured at JLab at $-t = 4 \text{ GeV}^2$ is of the opposite sign as expected by pQCD. At the upgraded Hall C we expect to extend these measurements to much higher $-t$.

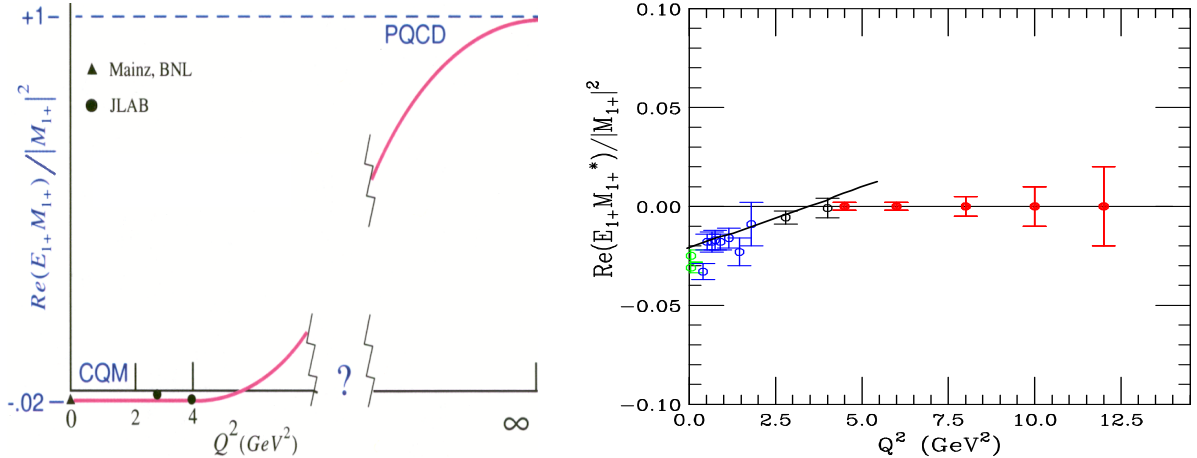


Figure 3.4: The Ratio of Electric Quadrupole to Magnetic Dipole Strength for the $p \rightarrow \Delta$ transition. Left: The curve indicates the low Q^2 region of helicity non-conserving spin flip transition, consistent with the current data (points), as well as the unknown region where $E_{1+}/M_{1+} \rightarrow 1$ in the pQCD limit. Right: The same ratio, as measured (green from Mainz and BNL, blue from JLab CLAS, black from JLab Hall C), and as projected for JLab Hall C at 11 GeV (red). The curve comes from an analysis of the world's unpolarized and polarized electroproduction data with the MAID dynamical isobar model [10, 11]. These authors state that the ratio shows a “clear tendency to cross zero, and becomes positive with increasing Q^2 . This is a possible indication of a very slow approach to the PQCD region.”

3.3 Structure Functions

There are several examples in nature where a force can appear to have a different behavior depending on the distance over which it acts. The Coulomb force between the electrons and the nucleus of an atom has a strength that falls off with the square of the distance between these charges, while at larger distances electrically neutral atoms attract each other via Van der Waals forces which fall off as the sixth power of the distance between them. Yet, the apparently different Coulomb and Van der Waals forces are manifestations of the same fundamental theory of electromagnetism. Similarly, the strong nuclear force which confines the quarks in hadrons can be calculated via QCD at short distance scales. But, we have not thus far been able to describe from QCD the forces at distances comparable to the size of hadrons. To obtain a complete picture of hadronic matter and the binding forces

thereof, then, it is necessary to measure structure functions over as large a range of disparate kinematics as possible.

3.3.1 F_1 and F_2 at Low Q^2 and Moderate x

The fundamental nucleon structure function F_2 may be studied in the transition region between distances comparable to, and small with respect to, the size of the proton using Q^2 as a measure of the wavelength of the virtual photon probe. This quantity has been measured over several orders of magnitude in Q^2 and x_{Bj} , and is well understood at high Q^2 in terms of logarithmic scaling violation. However, at low Q^2 , there are almost no data in the region $Q^2 < 1 \text{ (GeV/c)}^2$ and $0.005 < x_{Bj} < 0.2$. Moreover, data at low Q^2 and very low x_{Bj} from DESY indicate that F_2 falls proportionally to Q^2 . The latter behavior is a reflection of fundamental symmetries and conservation laws. At its most basic level, the F_2 structure function parameterizes the coupling between a point-like photon and a charged quark. Conservation of the electromagnetic current that generates the photon requires F_2 to vanish as the virtuality of the photon goes to zero. With the energy upgrade, we will be able to map out this important region which has not previously been accessible. Figure 3.5 indicates the relevant Q^2, x region accessible to an energy-upgraded Hall C, where the small angle spectrometer is particularly important. The data extend to a region of relatively high W where the Q^2 drop-off in F_2 has been observed.

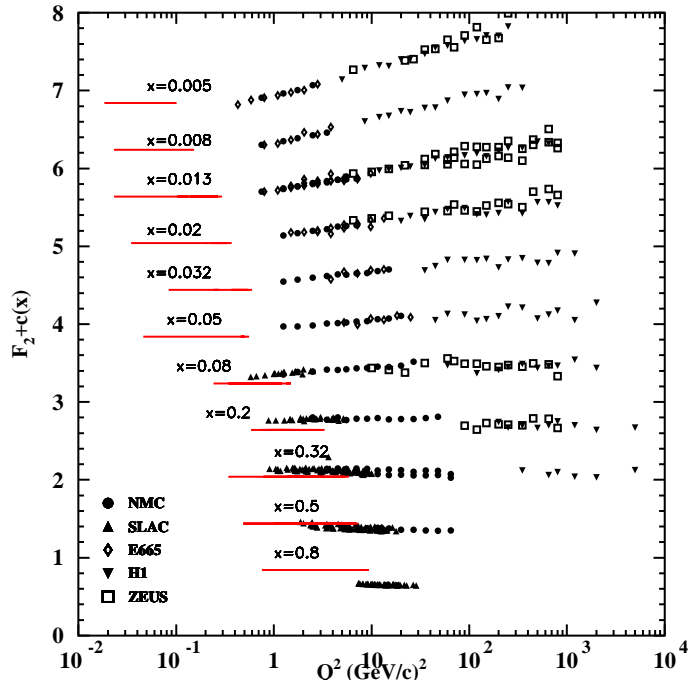


Figure 3.5: The Kinematic Regions Covered by Global Measurements of the Structure Function F_2 from various laboratories (data) compared to the region to be covered in Hall C at 11-GeV (kinematics indicated by red lines).

Measuring the complete set of unpolarized structure functions (R and F_2 , or F_1 and F_L) in inclusive electron scattering requires a separation of the cross section into longitudinal and transverse components. In the quark parton model, F_2 is the sum of quark and anti-quark distributions multiplied by x and weighted with the square of the electric charges of the quarks, while F_L is predicted to be zero for spin-1/2 partons (in agreement with higher

Q^2 measurements). In QCD, F_L acquires a non-zero value due to gluon radiation, which is proportional to the strong coupling constant α_s , with possibly sizeable higher order corrections in perturbation theory. The experimental situation for measurements of this structure function, as well as the corresponding R and F_1 structure functions, is far worse than that for F_2 , with a particular paucity of data at larger x_{Bj} .

With a 6-GeV beam, the measurement of separated structure functions at low and moderate values of Q^2 is limited to $Q^2 < 6 \text{ (GeV/c)}^2$. With an 11-GeV beam and the Hall C spectrometers, this range can be doubled and separated cross sections obtained out to $Q^2 = 12 \text{ (GeV/c)}^2$. Moreover, the precision possible for $4 < Q^2 < 6 \text{ (GeV/c)}^2$ can be significantly improved due to the extended ϵ range made possible by the larger beam energy as depicted in the right hand side of Fig. 3.6 for $x = 0.8$. Projected measurements (in blue for 6 GeV and pink for 11 GeV) at a fixed $x = 0.8$ of $R = \sigma_L/\sigma_T$, the ratio of longitudinal to transverse cross section, are shown in the left hand side of Fig. 3.6. The surrounding lines indicate the total statistic and systematic uncertainties possible, a substantial improvement to the existing data set shown in red. Data of this quality would be obtained for numerous such bins in x , allowing for the experimental extraction of all unpolarized structure function moments out to $Q^2 = 10 \text{ (GeV/c)}^2$. This is of particular interest since these moments are now calculable on the lattice.

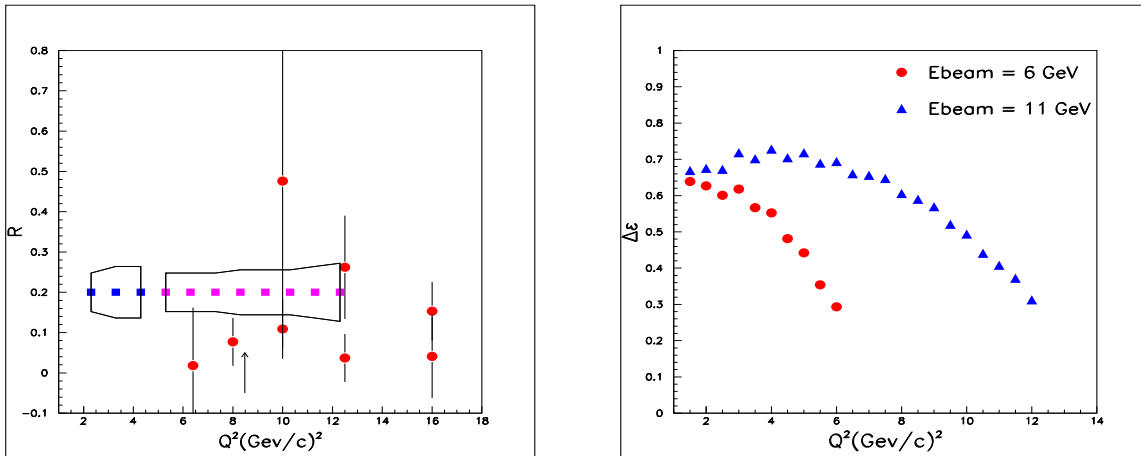


Figure 3.6: Left: projected measurements (blue for 6, pink for 11 GeV) at $x = 0.8$ for R , the longitudinal to transverse cross section ratio. The surrounding lines indicate the total uncertainty possible, as compared to the existing data set (red). The arrow corresponds to the Q^2 at which $x = 0.8$ corresponds to $W^2 = 4 \text{ GeV}^2$. Right: The range in ϵ available for Rosenbluth separations at $x = 0.8$ as a function of Q^2 .

3.3.2 Structure Functions at Higher x and Quark-Hadron Duality

While at present we cannot describe the structure and interactions of hadrons directly utilizing the quark and gluon degrees of freedom of QCD, we know that in principle it should just be a matter of convenience in choosing to describe a process in terms of quark-gluon or hadronic degrees of freedom. This principle is referred to as *quark-hadron duality*, and

means that one can use either set of complete basis states to describe physical phenomena. At high energies, where the interactions between quarks and gluons become weak and quarks can be considered asymptotically free, an efficient description of phenomena is afforded in terms of quarks; at low energies, where the effects of confinement make strongly-coupled QCD highly non-perturbative and the final state is guaranteed to be made of hadrons, it is more efficient to work in terms of collective degrees of freedom, the physical mesons and baryons. The duality between quark and hadron descriptions reflects the relationship between confinement and asymptotic freedom, and is intimately related to the nature of the transition from non-perturbative to perturbative QCD.

Although the duality between quark and hadron descriptions is formally exact in principle, how this reveals itself specifically in different physical processes and under different kinematic conditions is the key to understanding the consequences of QCD for hadronic structure. The phenomenon of duality is in fact quite general in nature and can be studied in a variety of processes, such as $e^+e^- \rightarrow$ hadrons, or semi-leptonic decays of heavy quarks. In electron–nucleon scattering, duality links the physics of resonance production to the physics of scaling, historically called Bloom-Gilman duality[12].

Figure 3.7 depicts recent Bloom-Gilman duality results from Hall C [13] for the proton F_2 structure function, as a function of the Nachtmann scaling variable ξ . At larger ξ , and therefore larger x and Q^2 , the resonance data agree very well on average with the deep inelastic parameterization from NMC [14], here shown at a fixed $Q^2 = 5$ (GeV/c) 2 . It was a surprise that the deep inelastic curve describes both the average resonance strength and Q^2 dependence so well, to better than 10%, to Q^2 values as low as ≈ 1 (GeV/c) 2 . At very low Q^2 , (< 0.8 (GeV/c) 2), however, it has been observed that the average resonance behavior takes a valence-like shape [15]. As discussed above, the low Q^2 regime is a region which may be explored at an 11-GeV Hall C facility.

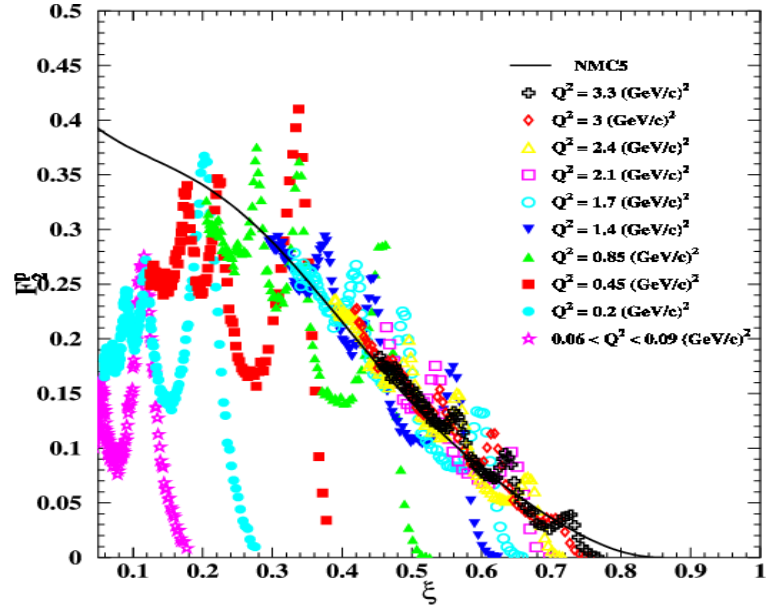


Figure 3.7: Duality Data from Hall C, depicting both the agreement in average strength and Q^2 dependence of the resonances and deep inelastic regimes for $Q^2 > 0.8$ (GeV/c) 2 , and the valence-like average shape of the lower Q^2 resonance data.

Bloom-Gilman duality can be formulated in the language of an operator product expansion (OPE) of the moments of structure functions, in which contributions are organized

according to powers of $1/Q^2$. The leading terms are associated with free quark scattering, and are responsible for the scaling of the structure function. The $1/Q^2$ terms involve interactions between quarks and gluons and hence reflect elements of confinement dynamics. Duality measurements have been explained in terms of a weak Q^2 dependence of the low moments of F_2 . This is interpreted within the OPE as indicating that the non-leading, $1/Q^2$ -suppressed, higher twist interaction terms do not play a major role even at low Q^2 ($\approx 1 \text{ GeV}^2$)[16].

While the OPE formalism allows us to organize hadronic observables in terms of an asymptotic expansion, it does not tell us *a priori* why certain matrix elements are small or cancel. This can only be addressed via numerical solutions of QCD, or from experiment. Since the details of quark–hadron duality are process dependent, there is no reason to expect the accuracy to which it holds and the kinematic regime where it applies to be similar for different observables. In fact, there could be qualitative differences between the workings of duality in spin-dependent structure functions and spin-averaged ones, or for different hadrons — protons compared with neutrons, for instance.

It is important to point out a revolutionary application of duality: if the workings of the resonance—deep-inelastic interplay are understood, the region of very high x , which has not been attainable in any other experiment, will be accessible. The region of $x \approx 1$ is an important testing ground for mechanisms of spin-flavor symmetry breaking in the valence quark distributions of the nucleon. In addition, with nuclear targets it would permit measurement of the nuclear medium modification of the nucleon structure function (nuclear EMC effect) at large x , where the deviation from unity of the ratio of nuclear to nucleon structure functions is largest, and sensitivity to different nuclear structure models greatest.

An 11-GeV beam in Hall C will make accessible the broad kinematic region required to map out both the resonance and deep inelastic regimes requisite to a number of inclusive duality and structure function studies, with the HMS and SHMS spectrometers allowing for L/T separation measurements which require a wide range in scattered electron energy and angle. There exist little to no inclusive spectra in the resonance region above $Q^2 \approx 8 \text{ (GeV/c)}^2$, data which will be easily obtainable in Hall C at 11 GeV where F_2 can be measured to $Q^2 > 15 \text{ (GeV/c)}^2$. Also, as previously noted, L/T separated data will also be available out to $Q^2 = 12 \text{ (GeV/c)}^2$ and can be used to obtain moments of all unpolarized structure function data.

In combination with the existing inclusive scattering data, typically emphasizing lower values of x , the 12-GeV data can be used to obtain moments of all unpolarized structure function data with unprecedented precision, up to $Q^2 \simeq 10 \text{ (GeV/c)}^2$. It is precisely these moments that are calculated in Lattice QCD. Figure 3.8(left) shows the quality of data for the lower moments of $F_2^p - F_2^n$ that will be accessible in Hall C, with recent Lattice QCD calculations [17]. It is anticipated that there will be dramatic progress in the latter calculations over the next decade.

3.3.3 Spin Structure Functions

Spin structure function studies possible at an 11-GeV JLab Hall C include both extensions of deep inelastic measurements into the region of the nucleon resonances to make a detailed exploration of duality, and measurements of the spin asymmetry $A_1 = (g_1 - (Q^2/\nu^2)g_2)/F_1$ at

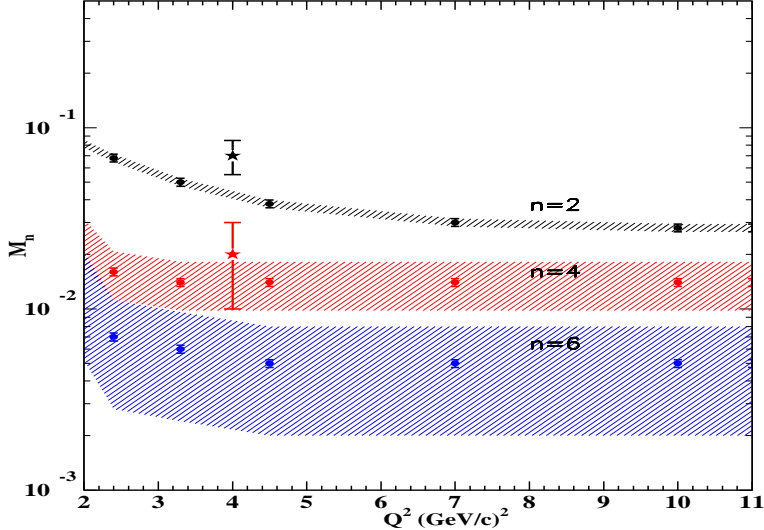


Figure 3.8: Lowest Moments of the Structure Function Differences $\int_0^1 x^{n-2} (F_2^p - F_2^n) dx$ (left) and $\int_0^1 x^{n-2} (g_1^p - g_1^n) dx$ (right), for $n = 2$ (black), 4 (red), and 6 (blue), as a function of Q^2 . Lattice QCD calculations (stars) are added at $Q^2 = 4$ (GeV/c) 2 for $n = 2$ (black) and 4 (red). Experimental moments without including JLab data are indicated as hatched areas. The 12-GeV program will obtain precise moments for $Q^2 \leq 10$ (GeV/c) 2 , for all polarized and unpolarized (e, e') structure functions.

x near 1. Data for this asymmetry are now available only up to $x \leq 0.85$, and only for a few values of Q^2 . At present, no conclusive evidence for quark-hadron duality in spin-dependent inclusive electron scattering has been demonstrated yet. An additional complication is that the existing data does not deconvolute g_1 and g_2 (or A_1 and A_2) in the nucleon resonance region. This can only be done with independent spin-dependent measurements with the target spin parallel (A_{\parallel}) and perpendicular (A_{\perp}) to the momentum transfer vector. Such measurements should be performed at nearly constant value of Q^2 , to facilitate studies of quark-hadron duality, and extraction of the polarized structure function moments of QCD. The spectrometer required for these measurements needs to be capable of detecting high momentum, forward angle scattered particles with enough resolution to obtain resonance spectra, all possible with the HMS-SHMS combination.

Solid or gaseous polarized targets that can operate at beam currents corresponding to luminosities of ≥ 100 Hz/nb, and effective beam and proton target polarizations of 80% (40% for deuteron or ^3He targets) will be available for spin structure function and moment measurements. Figure 3.9 shows the expected uncertainties in the experimental asymmetry A_{\parallel} for a possible measurement on a proton target at $Q^2 = 8$ (GeV/c) 2 , plotted as a function of the invariant mass. The projected data are plotted at a fixed arbitrary value (of 0), and represent the results of a two-week experiment. A similar measurement of A_{\perp} requires only a small amount ($\approx 10\%$) of this beam time.

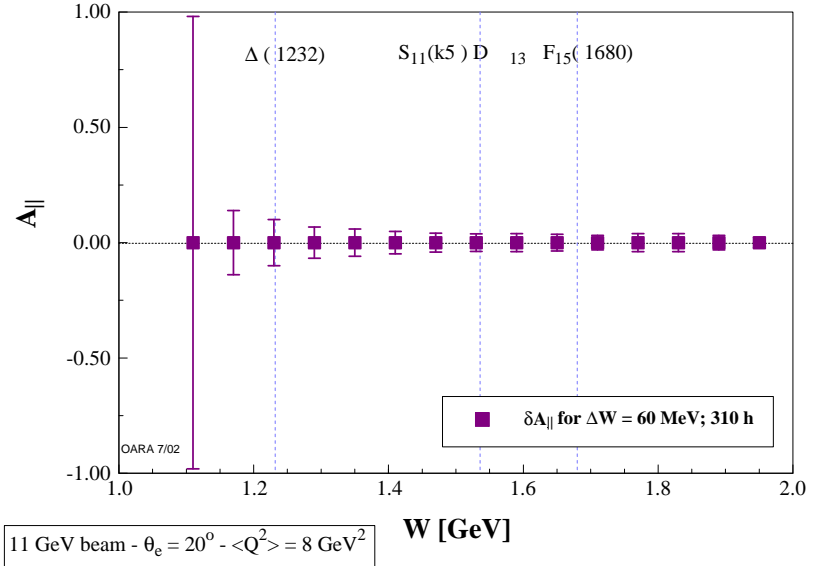


Figure 3.9: Expected Uncertainties for an 11-GeV Measurement of A_{\parallel} in the $\vec{H}(\vec{e}, e')$ reaction at $Q^2 = 8$ $(\text{GeV}/c)^2$ in the nucleon resonance region.

3.3.4 Semi-Inclusive Duality and Factorization

Hadronization describes the process how a quark involved in a high-energy scattering reaction evolves into the hadron that is detected. Initial investigations of the hadronization process were by electron-positron annihilation and deep inelastic scattering. In the former case, data from $e^+e^- \rightarrow hX$ show that a distinct function $D(z)$ may have developed for $z \geq 0.5$ at $W = 3$ GeV. The region extends to $z \approx 0.2$ for $W = 4.8$ GeV, and to $z \approx 0.1$ for $W = 7.4$ GeV. For $z > 0.3$, fragmentation functions have been obtained from data on $ep \rightarrow e'\pi^\pm X$ at $E = 11.5$ GeV, with $3 < W_x < 4$ GeV [18].

In deep inelastic scattering, high energies were used to separate the hadrons originating from the struck quark from those hadrons originating from the spectator quarks, by means of a large interval in rapidity. Recently, it has been argued that it is possible to reach such kinematic separation also at lower energies, **provided** one selects electroproduced pions or kaons with energies close to the energy transfer [19].

Given such a rapidity gap, the cross section may, just as in the asymptotic energy limit, under certain conditions still factorize into a structure function, giving the probability to find a quark in the nucleon, and a quark \rightarrow meson fragmentation function, or the probability that the quark hadronizes into the detected meson M . Such pre-asymptotic factorization conditions have been suggested to be related to the concept of quark-hadron duality[20]. The flavor dependence of duality can be determined through semi-inclusive meson production, by tagging specific mesons in the final state to identify individual quark species.

Close and Isgur predict that one may expect factorization and approximate duality to work at $Q^2 < 3$ GeV^2 and relatively low energy transfer, well within the range of the JLab at 12-GeV kinematics. Hints of such a behavior have been reported in Cornell data at similar energies. The extent to which factorization applies at lower energy is an open question, and the signatures of duality in the resonance region of semi-inclusive scattering need to be investigated. It is imperative that both of these questions be answered experimentally, and the HMS-SHMS setup at 12-GeV beam energy is optimally suited for this. This is

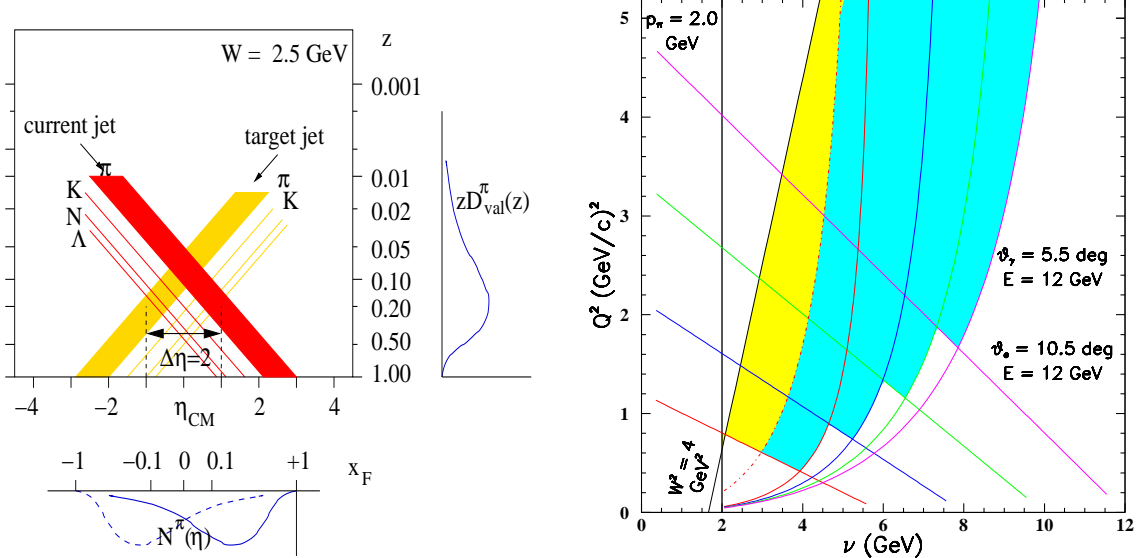


Figure 3.10: Left: Relation Between Elasticity z and Center-of-Mass Rapidity in semi-inclusive fragmentation for an invariant mass W of 2.5 GeV. Right: Kinematics plot for meson electroproduction experiments showing energy loss ν versus momentum transfer squared Q^2 , assuming the HMS-SHMS magnetic spectrometer combination. Kinematics of interest are in the deep inelastic region, i.e. $W^2 > 4 \text{ GeV}^2$ and accessible with HMS measuring the scattered electron (angle $> 10.5^\circ$) and SHMS measuring the produced meson (angle $> 5.5^\circ$). Beam energies of 6, 8, 10, and 12 GeV are assumed. The yellow area is what can be accessed at a 6-GeV beam energy with the present HMS-SOS magnetic spectrometer combination. The blue area is what can be accessed with the HMS-SHMS combination at a 12-GeV beam energy, and essentially corresponds to $W > 2.5 \text{ GeV}$. For a fixed Q^2 , the large kinematic acceptance in ν allows for a large variation in terms of elasticity z .

illustrated in Fig. 3.10, where the shaded area shows the kinematics region for deep exclusive reactions, arbitrarily cut off at a maximum $Q^2 \sim 5 \text{ (GeV/c)}^2$. Here, it is assumed that HMS, with a minimum angle of 10.5° , will detect the scattered electrons, and SHMS, with a minimum angle of 5.5° will detect the electroproduced mesons. For a fixed Q^2 , the large kinematic acceptance in ν allows for a large variation in terms of elasticity z . E.g., at $Q^2 = 2.5 \text{ (GeV/c)}^2$ the HMS-SHMS combination allows for precise measurements to verify the validity of factorization (or duality) for $0.2 < x < 0.7$ and $0.3 < z < 0.8$, within one month of beam time.

It is worth stressing here that confirmation of factorization and truncated duality would open the way to an enormously rich semi-inclusive program, allowing unprecedented spin and flavor decompositions of quark distributions. It possibly would also allow a similar spin and flavor decomposition of the fragmentation process, enabling us to understand the mechanism by which the quarks struck in the electron scattering process neutralize their color, to end up as the detected hadrons. Including strangeness electroproduction, even the sea could be mapped in this fashion.

3.4 Exclusive Reactions and Generalized Parton Distributions.

The recently developed formalism of “Generalized Parton Distributions” (GPDs) [21, 22, 23] for the first time provides us a rigorous map of the entire set of fundamental quantities of hadronic structure, such as: form factors, polarized and unpolarized parton distributions and components of the spin content of the nucleon due to orbital excitations. Thus, GPDs hold the promise of a complete determination of the nucleon wave function. Structure functions are probabilities, and intrinsically limited in what they can tell us about quark and gluon wavefunctions of hadrons. Until recently, attempts to determine such wavefunctions have been hopelessly handicapped by the lack of a rigorous framework for making a connection between them and any experiments. The discovery of GPDs and their connection to certain exclusive cross sections has made it possible, in principle, to map out complete nucleon wavefunctions. The GPDs are sensitive to the wavefunction at the amplitude level, rather than the probability level, and explore quark-quark correlations. Processes that lead to GPDs, and thence to quark and gluon wavefunctions, can be extracted under appropriate kinematic conditions from the generic production mechanisms shown in the top (“handbag”) diagram of Fig. 3.11.

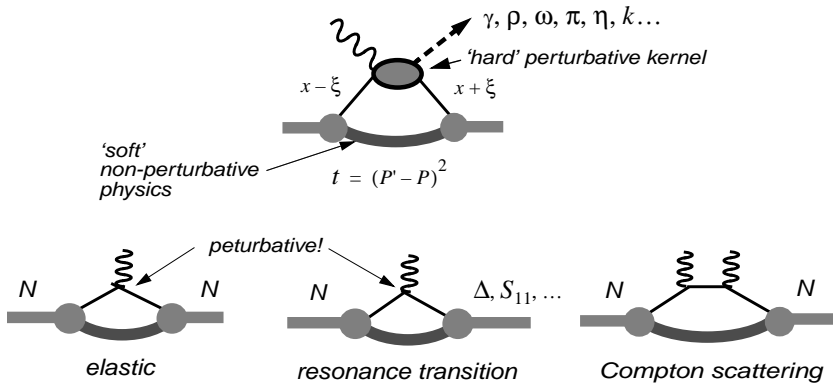


Figure 3.11: Deep Exclusive Scattering Processes that have been identified as providing a new window on the quark-gluon wavefunctions.

While pQCD is an interesting mechanism which probes the simplest Fock state component of the hadron, it does not address the large “soft” contribution which involves the more complex components of the hadronic wave functions. To achieve an understanding of the fully developed hadronic configuration, a theoretical mechanism is needed to describe the soft contributions to the reactions, which are measurable at accessible momentum transfers. The approach of addressing soft processes in terms of GPD’s achieves its full power at momentum transfers where the upper part of the handbag becomes fully perturbative. Here, the reaction factorizes into the perturbative part, and a GPD which represents the off-diagonal probability of the interacting quark being placed back into the remaining hadron intact but at a different transferred momentum. The power of this approach is that the same soft GPD, which contains the information about the hadronic structure is accessed in a variety of different reactions, while the hard perturbative part is reaction specific and calculable. The GPDs give us unique information about the transverse (k_\perp) and longitudinal (x) parton momentum distributions, and importantly, about the interference between the initial parton wave function and the phase shifted final parton wave function.

The GPD approach may be discussed in two kinematic regimes: the t dependent *form factor* type reaction; and the $t \rightarrow t_{min}$ *off-forward* production of mesons or photons.

3.4.1 High t Structure Functions and GPD's

The proposed Hall C configuration will provide a unique facility in the world in its capability of studying *form factor* type reactions at high momentum transfer. Here the incident real or virtual photon interacts perturbatively with one of the quarks within the hadron, and is followed by either of two processes: the quark is reabsorbed into the hadron leaving it either intact or in a higher resonant state. This reaction maps the full complexity of the non-perturbative nucleon structure and, in this picture, form factors are the lowest x moments of the GPDs. They constrain the longitudinal dependence of the hadronic structure and, as a function of t , uniquely provide a mapping of the k_\perp dependence of the hadron wave functions.

The measurement of F_π will serve as a prototypical reaction because the pion has the simplest hadronic structure for which we can measure the form factor at reasonably high $-t$. In a two-body framework the pion form factor is related to the pion GPD as [24, 25]

$$F_\pi(t) = \int_{-1}^1 \sum_q H_\pi^q(x, t) dx$$

with $H_\pi^q(x, t)$ related to the pion “wave function” by

$$H_\pi^q(x, t) \propto \int \Psi_\pi^*(x, k_\perp + \bar{x}q_\perp) \Psi_\pi(x, k_\perp) d^2k_\perp$$

where $\bar{x} \equiv 1 - x$, and q_\perp and k_\perp momentum transfer and struck quark transverse momentum in the pion. Taking the Fourier transforms yields the quark transverse spatial impact parameter distribution. $H_\pi^b(x, b_\perp) = \int dq_\perp e^{i\vec{b}_\perp \cdot \vec{q}_\perp} H_\pi^b(x, t)$.

One of our abiding interests is to obtain a three dimensional mapping of the nucleon structure by modeling the GPD's as a function of x and t , constrained by various form factor measurements as a function of t , and structure functions measurements as a function of x . Examples of form factor type reactions which will be measured in Hall C are the proton electric form G_{Ep}/G_{Mp} , the $N \rightarrow \Delta$ resonance transition form factors, the $N \rightarrow S_{11}$ transition amplitude $A_{1/2}$, and wide angle Compton scattering from the nucleon. In each case, there is a direct relationship between the form factor and a GPD.

For elastic scattering

$$F_1(t) = \int_{-1}^1 \sum_q H^q(x, t) dx \quad F_2(t) = \int_{-1}^1 \sum_q E^q(x, t) dx \quad (3.1)$$

where q signifies both quark and anti-quark flavors. We work in a reference frame in which the total momentum transfer is transverse so that $\xi=0$, and denote $H^q(x, t) \equiv H^q(0, x, t)$, $E^q(x, t) \equiv E^q(0, x, t)$, etc.

For Compton scattering the appropriate *form factor-like* quantities are the -1'th moments of the GPD's

$$R_1(t) = \int_{-1}^1 \sum_q \frac{1}{x} H^q(x, t) dx \quad R_2(t) = \int_{-1}^1 \sum_q \frac{1}{x} E^q(x, t) dx \quad (3.2)$$

Resonance transition form factors access components of the GPD's which are not accessed in elastic scattering or wide angle Compton scattering. The $N \rightarrow \Delta$ form factors are related to isovector components of the GPD's.

$$G_M^* = \int_0^1 \sum_q H_M^q(x, t) dx \quad G_E^* = \int_{-1}^1 \sum_q H_E^q(x, t) dx \quad G_C^* = \int_{-1}^1 \sum_q H_C^q(x, t) dx \quad (3.3)$$

where G_M^* , G_E^* and G_C^* are magnetic, electric and Coulomb transition form factors, and H_M^q , H_E^q , and H_C^q are isovector GPD's, which can be related to elastic GPD's in the large N_C limit through isospin rotations. The $N \rightarrow S_{11}$ transition form factor is also important, as it probes fundamental aspects of dynamical chiral symmetry breaking in QCD. If chiral symmetry were not broken, the S_{11} would be the nucleon's parity partner and the N and S_{11} masses would be degenerate.

A major component of the Hall C program will be to measure all of these form factor exclusive reactions to the highest t attainable. The measurement of G_{Ep}/G_{Mp} will extend existing results, currently at $Q_{max}^2 = 5.6$ (GeV/c)² to about 14 (GeV/c)² as previously shown in Fig. 3.3. The wide-angle Compton scattering experiment will measure both s and t dependences with high precision out to about 15 (GeV/c)², as shown in Fig. 3.12. Here, the process may be described by Compton scattering from a single free quark convoluted with the GPD of the quark in a proton. The cross section may be written as a function of vector and axial vector terms (as plotted) which directly probe the GPDs.

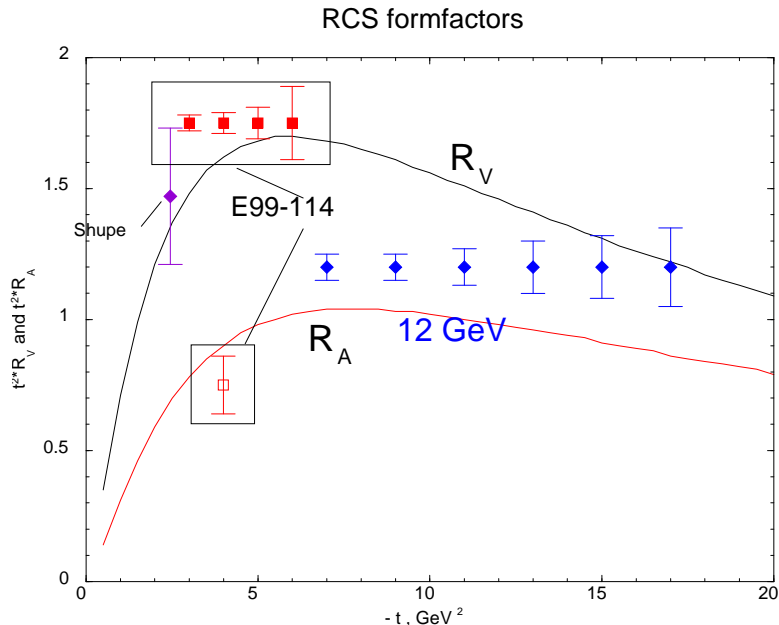


Figure 3.12: Projected measurements for wide angle Compton scattering as a function of $-t$, as compared to recent JLab data.

Transverse recoil proton asymmetries, for which GPD and pQCD based theoretical calculations make very different predictions will also be measured.

The $p \rightarrow \Delta$ form factor G_M^* and the $p \rightarrow S_{11}$ form factors will be measured by missing mass technique out to $Q^2 \sim 18$ (GeV/c) 2 (see Fig. 3.13). All these form factor measurements will be used as part of a consistent data set which constrains the longitudinal and transverse momentum distributions in the nucleon.

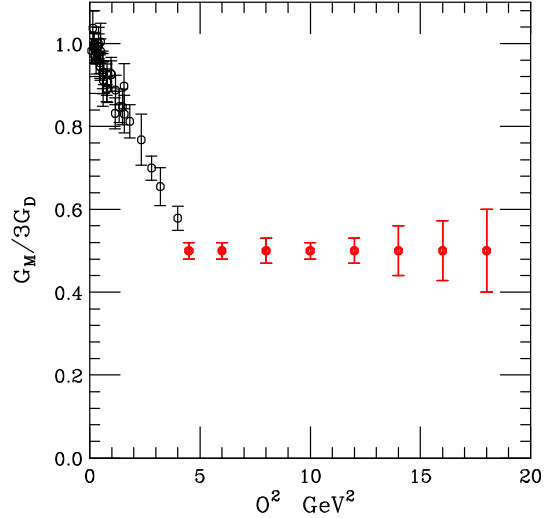


Figure 3.13: The Delta Resonance Transition Form Factor, as compared to the dipole. Existing Hall C and other data are in black, with projected 11-GeV Hall C results in red.

3.4.2 Low t GPDs

One promising class of reactions sensitive to GPDs are the hard exclusive lepto-production of mesons. This is based on a factorization theorem which states that for longitudinally polarized photons the meson production amplitudes can be factorized into two parts. One part which is exactly calculable in pQCD and describes the interaction of the virtual photon with the quark and gluons of the target, and another part with information about the long-distance and non-perturbative components in the meson and the nucleon target, which can be parametrized in terms of the GPDs. The factorization theorem has recently been proven [23] for lepto-production of mesons at large photon virtuality ($Q^2 \gg \Lambda_{QCD}^2$) and $|t| < \Lambda_{QCD}^2$. The polarized GPDs can be separated from the unpolarized ones by measuring pseudo-scalar meson production and vector-meson production respectively. However, GPDs are related to cross-sections through integrals and hence they require de-convolution procedures. This implies that cross-sections alone are not sufficient, but it is also important to measure spin observables. Moreover, the extraction of GPDs cannot be achieved just by a single experiment but it entails measurements of a variety of channels and observables. The single target spin asymmetries in single pion electroproduction is one such observable. These asymmetries depend on the imaginary part of the product of the polarized GPDs, and calculations for nucleon targets have recently become available [27].

A measurement of the single target spin asymmetry in the reaction $e n \rightarrow e' \pi^- p$ with a transversely polarized ${}^3\text{He}$ target is a feasible option to access the polarized GPDs. The polarized ${}^3\text{He}$ target acts as an effective polarized neutron target in these experiments. These asymmetry measurements can be done with an 11-GeV electron beam on a transversely polarized ${}^3\text{He}$ target and the SHMS and the HMS used to detect the scattered electron and π^- in coincidence. The high momentum and small angle capability of SHMS give a large

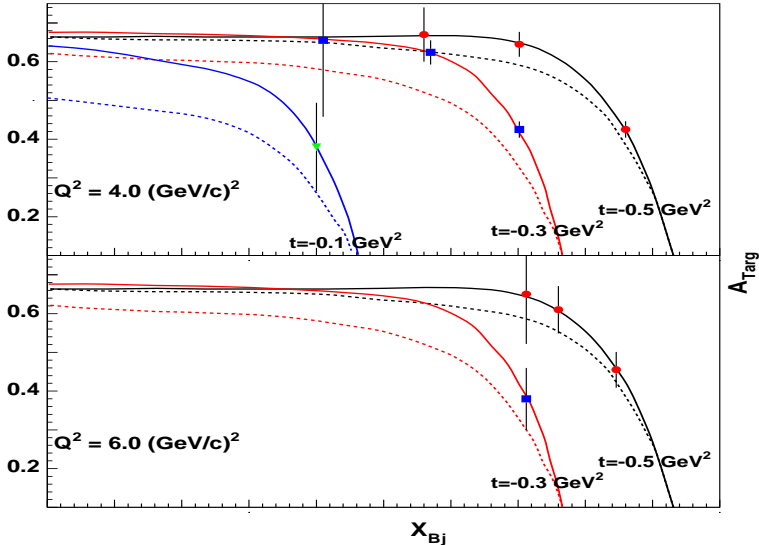


Figure 3.14: The Projected Results for Target Asymmetry in the Process $e n \rightarrow e' \pi^- p$ with a transversely polarized ${}^3\text{He}$ target. The solid and dashed lines are the calculations from Ref. [27] and represent different model assumptions regarding the GPDs.

coverage of the relevant kinematic variables Q^2 , x_{Bj} and t . It is important to stress that the region of interest for extracting GPDs is $-t < 1.0$ $(\text{GeV}/c)^2$, because the factorization theorem holds only for low t . Thus the forward angle capabilities of the SHMS are a key advantage for Hall C. Figure 3.14 shows the feasibility of measuring the target asymmetry in electroproduction of pions from a transversely polarized ${}^3\text{He}$ target.

3.5 The Nucleus as a Laboratory

3.5.1 Color Transparency

Color Transparency is an unusual QCD effect having its most counterintuitive manifestation in $A(e, e' p)$ experiments at very high energy. The basic idea is that, under the right conditions, three quarks, each of which would normally interact very strongly with nuclear matter, could form an object that passes undisturbed through the nuclear medium. A similar phenomenon occurs in QED, where an e^+e^- pair of small size has a small cross section determined by its electric dipole moment. In QCD, a $q\bar{q}$ or qqq system can act as an analogous small color dipole moment.

Current theoretical calculations suggest that most of the CT effect should be seen around $Q^2 = 10$ $(\text{GeV}/c)^2$. Experiments at SLAC and JLab have found no evidence for the onset of CT effects at momentum transfers up to 8.1 $(\text{GeV}/c)^2$. However, there is some potential evidence for CT in $A(p, 2p)$ data from Brookhaven (left side of Fig. 3.15). If one attributes the rise in Transparency in this data to CT, then it must be observable in $A(e, e' p)$ measurements at $Q^2 > 12$ $(\text{GeV}/c)^2$, corresponding to comparable momenta of the ejected nucleon. Hall C at 11 GeV will answer this question, allowing for searches for Color Transparency in the $A(e, e' p)$ reaction up to $Q^2 = 18$ $(\text{GeV}/c)^2$ (see right side of Fig. 3.15), and in the $A(e, e' \pi)$ case up to $Q^2 = 14$ $(\text{GeV}/c)^2$. Intuitively, one expects an earlier onset of CT for meson production than for hard proton scattering, as it is much more probable to produce a small

transverse size in a $q\bar{q}$ system than in a three quark system.

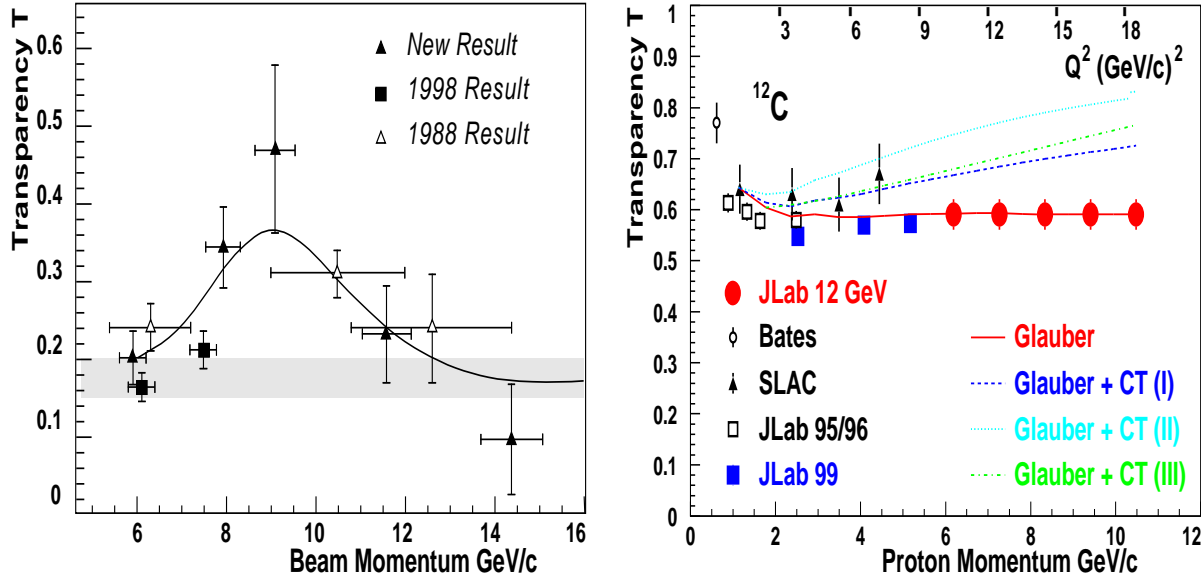


Figure 3.15: A(p,2p) Transparency Data from BNL (left), Compared to Recent and 11-GeV Projected Color Transparency Data from ($e,e'p$) measurements on Carbon in Hall C (right).

Not observing the Color Transparency phenomenon casts doubt on the strict applicability of the QCD factorization theorems, intrinsically related to the Generalized Parton Distributions. Color Transparency is a necessary, but not sufficient, indication of the applicability of the QCD factorization theorems.

3.5.2 $x > 1$ and Superfast Quarks

At extremely high temperature or density, matter is expected to undergo a phase transition wherein quarks and gluons are no longer confined within hadrons and instead form a quark-gluon plasma. While ordinary nuclear densities are well below the expected phase transition, local fluctuations in density can occur within nuclei when nucleons are close together. The EMC effect and measurements of in-medium proton form factors provide hints of some modification to hadron structure at ordinary nuclear densities [28]. At close range, these nucleons interact via the strong repulsive core of the N-N interaction, and thus typically have extremely large momenta. Inclusive scattering at $x > 1$ is sensitive to these high momentum nucleons and can therefore be used to probe these high-density configurations. At extremely high Q^2 values measurements at $x > 1$, no longer probe the nucleon distributions, but instead measure the distribution of “superfast” quarks in nuclei. As these superfast quarks carry a momentum fraction larger than an entire nucleon would be expected to carry, they only occur when multiple nucleons share momentum. By extracting the distribution of superfast quarks within nucleon clusters, we can look for the onset of deconfinement which may manifest itself as nucleon ‘swelling’ or the collapse of two nucleons into a 6-quark bag as one approaches the phase transition. Figure 3.16 shows an example of such an experiment that could be carried out in an energy-upgraded Hall C, where it would be possible to obtain a maximum

momentum transfer $\approx Q^2 = 23$ $(\text{GeV}/c)^2$.

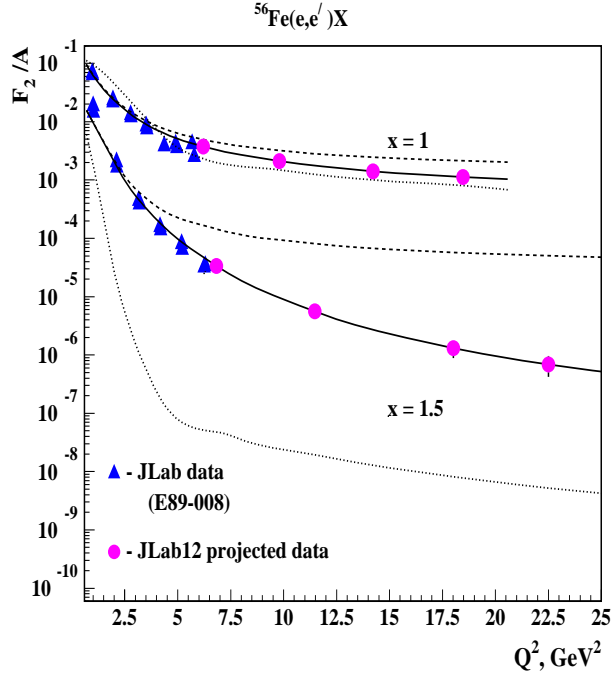


Figure 3.16: An Example Measurement of Inclusive Electron Scattering from an Fe Target, allowing for data up to four-momentum values near 23 $(\text{GeV}/c)^2$.

Studies at JLab will complement studies of high temperature, high density regions of the phase diagram of nuclear matter (see Fig. 3.17) planned for relativistic heavy ion experiments at RHIC and the LHC. One can access the low temperature, high density phase at, for example $x = 2$ and $Q^2 = 10$ $(\text{GeV}/c)^2$. Here, on the very extreme tails of the quark distribution functions, the small cross sections are accessible only with the high luminosity, good acceptance, and good resolution properties of the Hall C equipment.

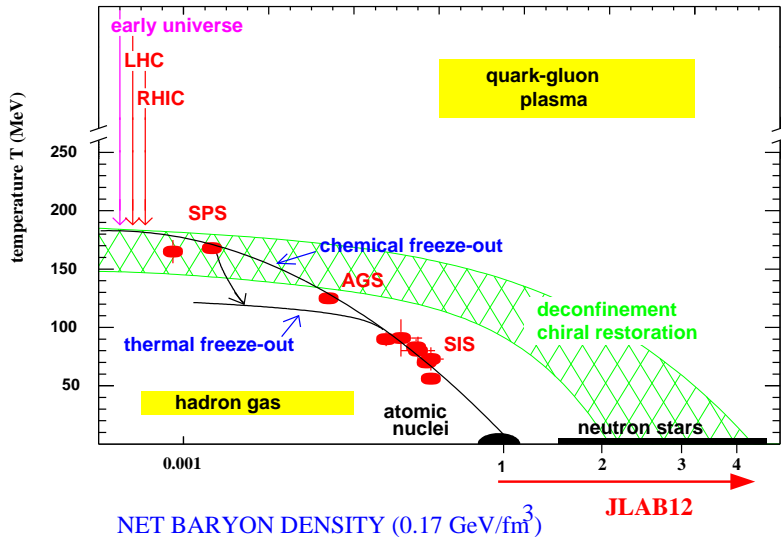


Figure 3.17: The Phase Diagram for Nuclear Matter.

In addition to mapping out the transition to deconfinement as one approaches chiral restoration, we also probe the behavior of cold, dense hadronic matter (up to 3-4 times nuclear matter densities in the region where nucleons overlap). This is also the region of

temperature and density relevant to understanding the equation of state of neutron stars and to study the possible transition from neutron star to "quark stars". Large x distributions involve the very extreme tails of the quark distribution functions. This, combined with high Q^2 , means very small cross sections, which can be accessed only with a high energy (11 GeV is appropriate), high luminosity, beam combined with good detector acceptance and resolution properties such as that proposed for Hall C.

3.5.3 Nuclear Broadening

The production of mesons (M) in semi-inclusive electron scattering, $eN \rightarrow e'MX$, yields insights into the quark structure of the nucleon that are unavailable in inclusive measurements. Another potential for this type of measurement is the ability to directly probe multiple parton correlation functions inside a nucleus. As the struck quark travels through a nucleus, it loses energy via radiation, and picks up additional transverse momentum due to multiple scattering. Understanding this increased transverse momentum broadening is fundamental to the development of an understanding of quark effects in nuclei.

Inside a large nucleus, multiparton scattering can take place within one nucleon or between different nucleons. At high energies, a single hard scattering is always localized within one nucleon, and it cannot have any large dependence on the nuclear size. Similarly, multiple scattering within one nucleon cannot have much dependence on nuclear size. Therefore, large dependence on nuclear size is a *unique* signal of partons multiple scattering between nucleons. Measurements of anomalous dependence on nuclear size for any physical observable will provide direct information on multiparton correlation functions within a nucleus. Direct measurement of the multiparton correlation functions is of great importance for testing the generalized QCD factorization theorem, which allows for the application of QCD perturbation theory in studying collisions involving nuclei (for instance, in relativistic heavy ion collisions).

However, there are many QCD multiparton correlation functions, and it is important to identify those physical observables which depend on only a small number to separate contributions. It has been pointed out that the $A^{1/3}$ -type enhancement of the transverse momentum broadening of Drell-Yan pairs and the jet broadening in lepton-nucleus deep inelastic scattering are good observables because, at leading order α_s , these observables depend only on one type of multiparton correlation function: the correlation between hard quarks and soft gluons. Experimentally, the $A^{1/3}$ -type nuclear enhancement has been observed in the transverse momentum broadening of Drell-Yan pairs in hadron-nucleus collisions, and the measured dijet momentum imbalance in photon-nucleus collisions. While the latter depends on final state multiple scattering, and the former on initial state, the leading order calculation for the quark-gluon correlation function strengths should agree. However, the Drell-Yan is much smaller. Therefore, a measurement of the transverse momentum broadening in deep inelastic semi-inclusive pion production would provide an independent measurement and a test of the QCD treatment of nuclear multiple scattering.

It has been suggested that measuring the transverse momentum broadening of the leading pions in deep inelastic scattering at Jefferson Lab energies can provide good information on this quark-gluon correlation function[29]. As shown in Fig. 3.18, it is predicted that the size of the $A^{1/3}$ -type broadening is large enough to be measured experimentally. These

predictions assume factorization and, while calculated for 6 GeV, will be more applicable and accessible kinematically at 12 GeV.

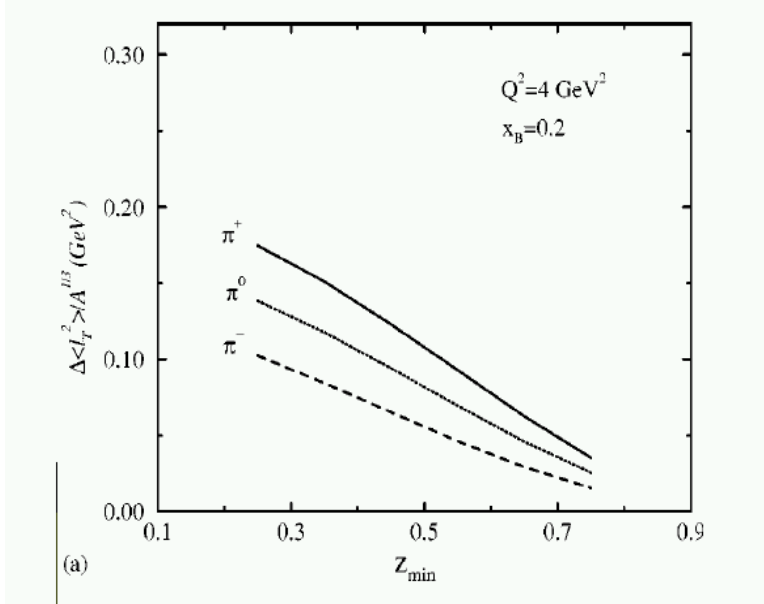


Figure 3.18: The Predicted Nuclear Transverse Momentum Broadening in Semi-Inclusive Pion Production.

By measuring the transverse momentum broadening for π^+ , π^- , and π^0 , and keeping a reasonably large value of z_{\min} , it would be possible to extract the quark flavor dependence of the correlation functions. Predictions are more reliable for the leading pions, or pions having relatively large momenta and, hence, the SHMS will be an excellent tool for this type of measurement.

3.6 Search for New Physics

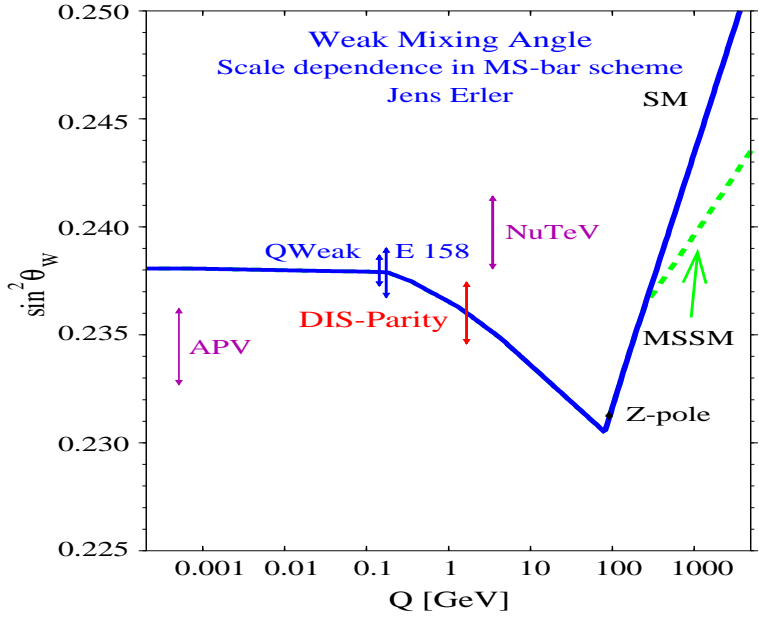
The weak mixing angle, θ_W is one of the fundamental parameters of the Standard Model. The tangent of the weak mixing angle represents the relative coupling strength of the SU(2) and U(1) groups (g and g'). At the Z resonance, the value of $\sin^2(\theta_W)$ has been well established through a number of measurements. One important consequence of the Standard Model is that the value of $\sin^2(\theta_W)$ will vary (run) as a function of Q^2 , as shown in Fig. 3.19 along with existing and projected measurements. Deviations from the predicted running are sensitive to possible extensions of the Standard Model. Unfortunately, there are few measurements of $\sin^2(\theta_W)$ away from $Q^2 = M_Z^2$.

Two measurements which were made away from the Z -pole come from atomic parity violation (APV) and νA scattering. The most recent calculations of cesium APV appear to disagree with the measured values by approximately two standard deviations, however, the interpretation of APV results have been somewhat controversial and the extracted value for the weak charge [$Q_W = 1 - 4\sin^2(\theta_W)$] depends on a detailed understanding of atomic structure. The most recent calculations of cesium APV appear to disagree with the measured values by approximately two standard deviations [30]; however, this conclusion is by no means universal and there is still considerable ongoing discussion in the literature about these values. At higher energies using neutrino scattering on iron, the NuTeV collaboration at Fermilab

recently reported a value for $\sin^2 \theta_W^{\text{on-shell}}$ three standard deviations above the Standard Model predictions [31]. Naturally, this deviation has been interpreted both somewhat conventionally and in terms of physics beyond the Standard Model.

A competitive search for physics beyond the Standard Model can be made using deep inelastic parity violation at Jefferson Lab using the upgraded 11-GeV beam. A measurement of $\sin^2(\theta_W)$ would be possible to an 0.6% relative error. It is important to note that such an experiment is complimentary to both the planned SLAC Møller and JLab Q_{weak} parity-violating experiments, with a different sensitivity to “new physics” scenarios.

Figure 3.19: The Running of $\sin^2 \theta_W$ Shown as a Function of Q^2 . The proposed combined statistical and systematic precision of the DIS parity violation experiment (DIS-Parity) is shown in red. Also shown are the existing APV cesium and neutrino DIS (NuTeV) measurements along with expected uncertainties for the approved Jefferson Laboratory QWeak and running SLAC E-158 Møller experiments.



The proposed experiment is sensitive to “new physics” in both the axial Z-electron coupling times the vector Z-u quark (d quark) coupling ($C_{1u(d)}$) and the vector Z-electron coupling times the axial Z-u quark (d quark) coupling ($C_{2u(d)}$), specifically $2C_{1u} - C_{1d}$ and $2C_{2u} - C_{2d}$. Each of the C_{ia} terms is sensitive to physics beyond the Standard Model in different ways. The sensitivity to $2C_{2u} - C_{2d}$ makes this experiment quite unique. Figure 3.20 shows the much tighter bounds on both C_{2u} and C_{2d} provided by this proposed 11-GeV Hall C experiment in conjunction with the SAMPLE experiment at BATES.

To fully explore the range of possible extensions to the Standard Model, the experiments at SLAC, BATES, and Jefferson Lab form a nicely complimentary program, and will give unprecedented information on the running of the electroweak coupling constant.

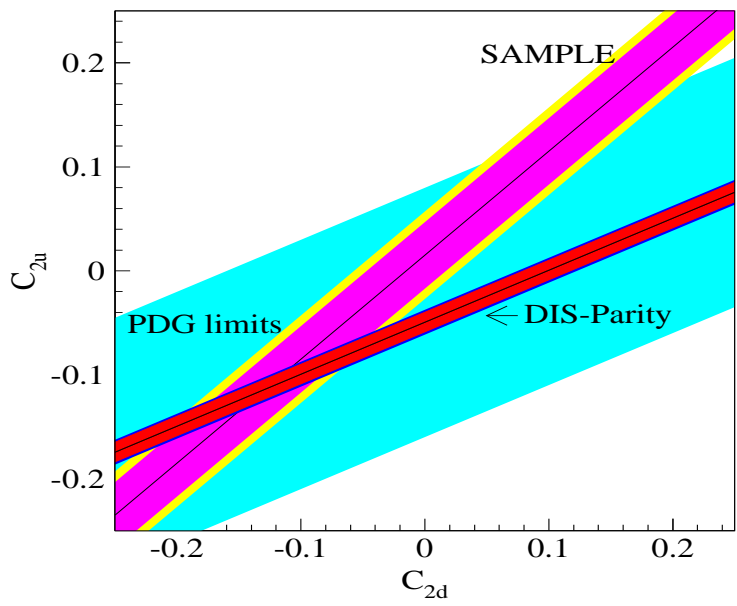


Figure 3.20: The Limits on C_{2u} and C_{2d} Listed by the Particle Data Group, SAMPLE, and the Proposed Experiment.

Chapter 4

Spectrometer Systems

4.1 Overview

The physics outlined in the previous chapter can be accessed only if the Hall C spectrometer system is capable of providing the necessary measurements with precision, rate, and trigger capabilities consistent with those physics goals. Our plan for meeting this need consists of improving the existing High Momentum Spectrometer (HMS) and providing a new Super High Momentum Spectrometer (SHMS). The SHMS will be capable of analyzing the higher energy particles produced by the 12-GeV upgraded CEBAF beam, which are above the momentum range of the HMS. The SHMS will be thoughtfully designed as a companion to the HMS so that, taken together, the system will provide full momentum range single-arm capabilities as well as double-arm coverage over the entire kinematic region of interest to the proposed experiments. Thus, the SHMS will not be a replacement for the HMS, but rather a complementary partner to it just as the SOS (Short Orbit Spectrometer) functions as a partner to the HMS.

To this end we will proceed by first reviewing the characteristics of the existing HMS in section 4.2. The physics demands on the Hall C spectrometer system were developed in section 2.2. With that background we can derive what improvements to the HMS are necessary and what are the needed specifications for the companion SHMS. A summary of those specifications and a design for the SHMS which provides what the physics demands is given in section 4.3.

Especially for particle identification, there is no single choice of detector elements which is optimum over the full momentum range and for all experiments in which the SHMS will be used. The system design will provide for convenient rearrangement and substitution of detector modules as needed for particular experiments. The baseline design will consist of a subset of these modules. The choice of which of these elements will be included in the baseline SHMS spectrometer will be made on the basis of physics experiment scheduling priorities. In this report we present the core design of each detector type and how it contributes to the system.

4.2 The High Momentum Spectrometer

The HMS is a focusing spectrometer which can be tuned for central momenta from 0.4 to 7.3 GeV/c and production angles from 10.5 to 90 degrees relative to the beam direction. Its momentum acceptance is 20% and the angular coverage is ± 32 mr in-plane by ± 85 mr out-of-plane, achieved by the optical system consisting of three quadrupoles in a FDF arrangement followed by a dipole. The angular acceptance is defined by a collimator near the upstream end of the spectrometer.

The optical system is followed by a detector stack made up of two pairs of crossed scintillator hodoscopes, twelve planes of precision drift chambers, a gas Čerenkov counter which can operate from 0.3 to 2.5 atm., an aerogel Čerenkov counter, a segmented lead-glass shower counter, and a muon counter. A schematic diagram of the magnets and detector stack is shown in Fig. 4.1. The system is tied together by a triggering and data acquisition system providing full event readout of more than 1000 events/second with time-of-flight (TOF) and coincidence time resolution better than 200 ps.

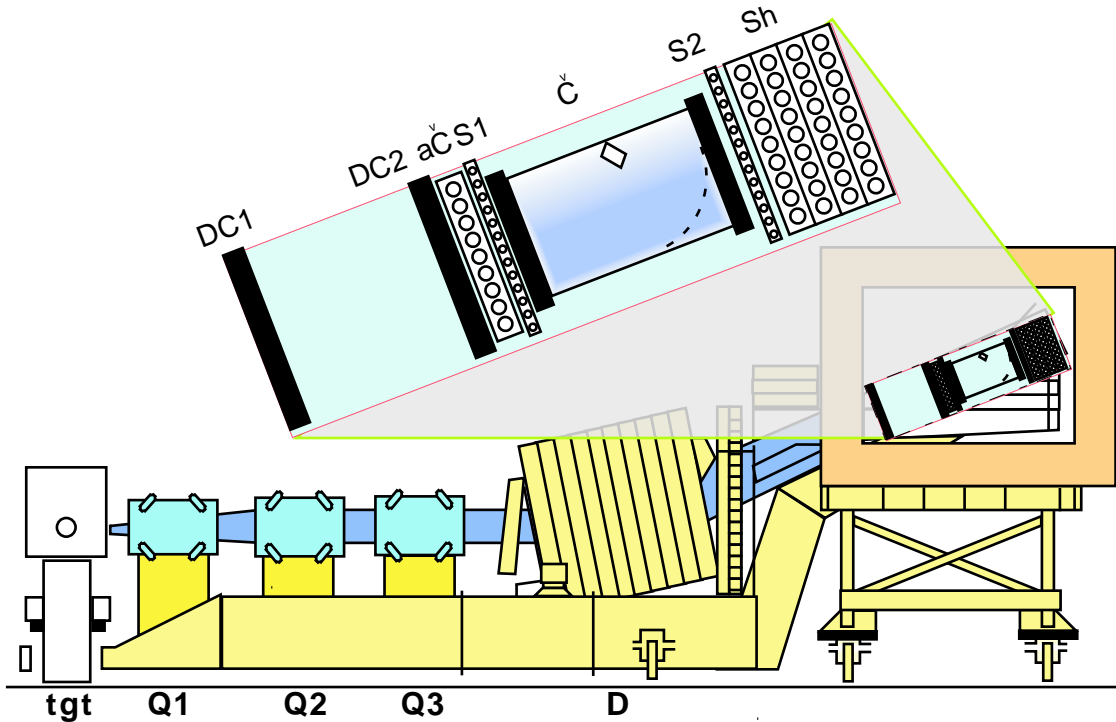


Figure 4.1: Sketch of the High Momentum Spectrometer showing the Magnets, the Carriage, and an expanded block diagram of the Detector Stack.

Since the beginning of physics operation in Hall C, the HMS has provided precision tracking and particle identification for many experiments. Figure 4.2 shows some of the detector calibration results from these experiments which demonstrate its resolution and particle discrimination capabilities, which are summarized in Table 4.1.

Rotation of the whole spectrometer to a new central scattering angle is accomplished remotely, without the need for access to the radiation enclosure, in about ten minutes.

Angular setting accuracy is better than half a milliradian. Similarly, the central momentum may be adjusted remotely in about the same amount of time. This capability is crucial to experiments that must take data at a multitude of kinematic settings.

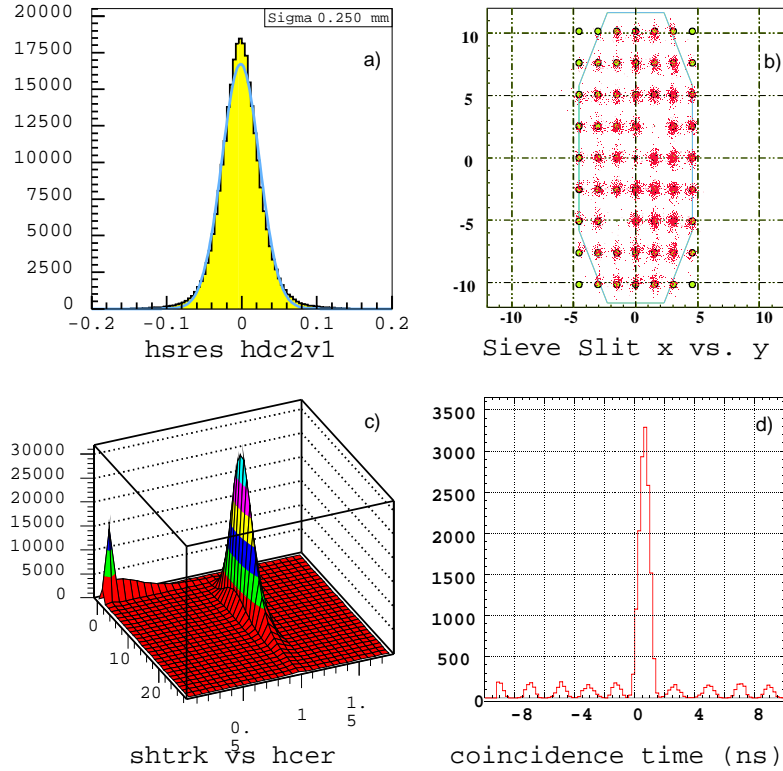


Figure 4.2: HMS Spectrometer Representative Data: Tracking capability is shown by a) Single-plane wire chamber resolution, and b) sieve slit reconstruction. Panel c) shows Shower Counter Energy vs. number of photons in the Čerenkov, demonstrating clear electron-hadron separation. Coincidence time resolution in the HMS-SOS hodoscope system is demonstrated in panel d) by the clear separation of particles from neighboring RF buckets.

<i>Parameter</i>	<i>HMS Performance</i>
Range of Central Momentum	0.4 to 7.4 GeV/c
Momentum Acceptance	$\pm 10\%$
Momentum Resolution	0.1% – 0.15%
Scattering Angle Range	10.5 to 90 degrees
Maximum Target Length at 90 degrees	10 cm
Horizontal Angle Acceptance	± 32 mrad
Vertical Angle Acceptance	± 85 mrad
Solid Angle Acceptance	8.1 msr
Horizontal Angle Resolution (yptar)	0.8 mrad
Vertical Angle Resolution (xptar)	1.0 mrad
Vertex Reconstruction Resolution (ytar)	0.3 cm
Maximum Event Rate	2000 events/second
Maximum Flux within Acceptance	~ 5 MHz
e/h Discrimination	>1000:1 at 98% efficiency
pi/K Discrimination	100:1 at 95% efficiency

Table 4.1: Summary of the HMS Performance

4.3 The Super High Momentum Spectrometer

4.3.1 Overview

The Super-High-Momentum Spectrometer (SHMS) will play a vital role in the overall JLab physics program at 12 GeV. Short latency detector elements will minimize pileup and out-of-time events and, coupled with advanced data acquisition components, will allow readout of 10,000 or more events per second. An inevitable consequence of relativistic kinematics is that much of the interesting physics at 12 GeV will only be accessible provided at least one of the spectrometers can achieve angles significantly below 10 degrees. The SHMS will achieve a minimum scattering angle of 5.5 degrees with acceptable solid angle and it will do so at high luminosity. The maximum momentum will be 11 GeV/c, well matched to the maximum beam energy available in Hall C. These three characteristics (high luminosity, small scattering angle, and high momentum) are essential for carrying out a program of electron-hadron coincidence experiments at large $z = E_h/\nu$, where ν is the electron energy loss. (For orientation, in the limit of $z \rightarrow 1$, one approaches the exclusive limit.) At large z (i.e. $z \approx 1$), sensitivity to the valence quark structure of the hadron is maximized and the reaction mechanism is simplified.

The HMS-SHMS spectrometer pair will be rigidly connected to a central pivot which permits both rapid, remote angle changes and reproducible rotation characteristics which simplify accurate measurements. From its inception, the SHMS momentum and target acceptances have been designed to be very flat, with performance similar to that of the HMS. This also simplifies making accurate measurements. These capabilities will facilitate experiments which rely on a large number of angle and momentum settings, such as L-T separations, for which accurate pointing as well as flat momentum and target acceptances are essential. Finally, for experiments which are willing to trade off small-angle performance for increased solid angle, this can be achieved by pulling the magnets and detectors forward and re-tuning the spectrometer. A schematic diagram of the proposed SHMS design is shown in Fig. 4.3. In the remainder of this section we will address the design and performance details of the SHMS.

4.3.2 The SHMS Magnets and Structural Design

4.3.2.1 General

The SHMS is an 11-GeV/c superconducting spectrometer. The magnet system consists of two cold iron quadrupoles similar in design to the HMS Q1, and a combined function warm bore magnet that is 5 m long. The cryogenics are proven systems using standard JLab components. The shield house is a composite of concrete, steel and lead. The magnets and the shield house are supported by a welded steel structure with steel drive wheels. Fig. 4.3 shows a perspective view of the spectrometer and Fig. 4.4 provides a line drawing of the layout.

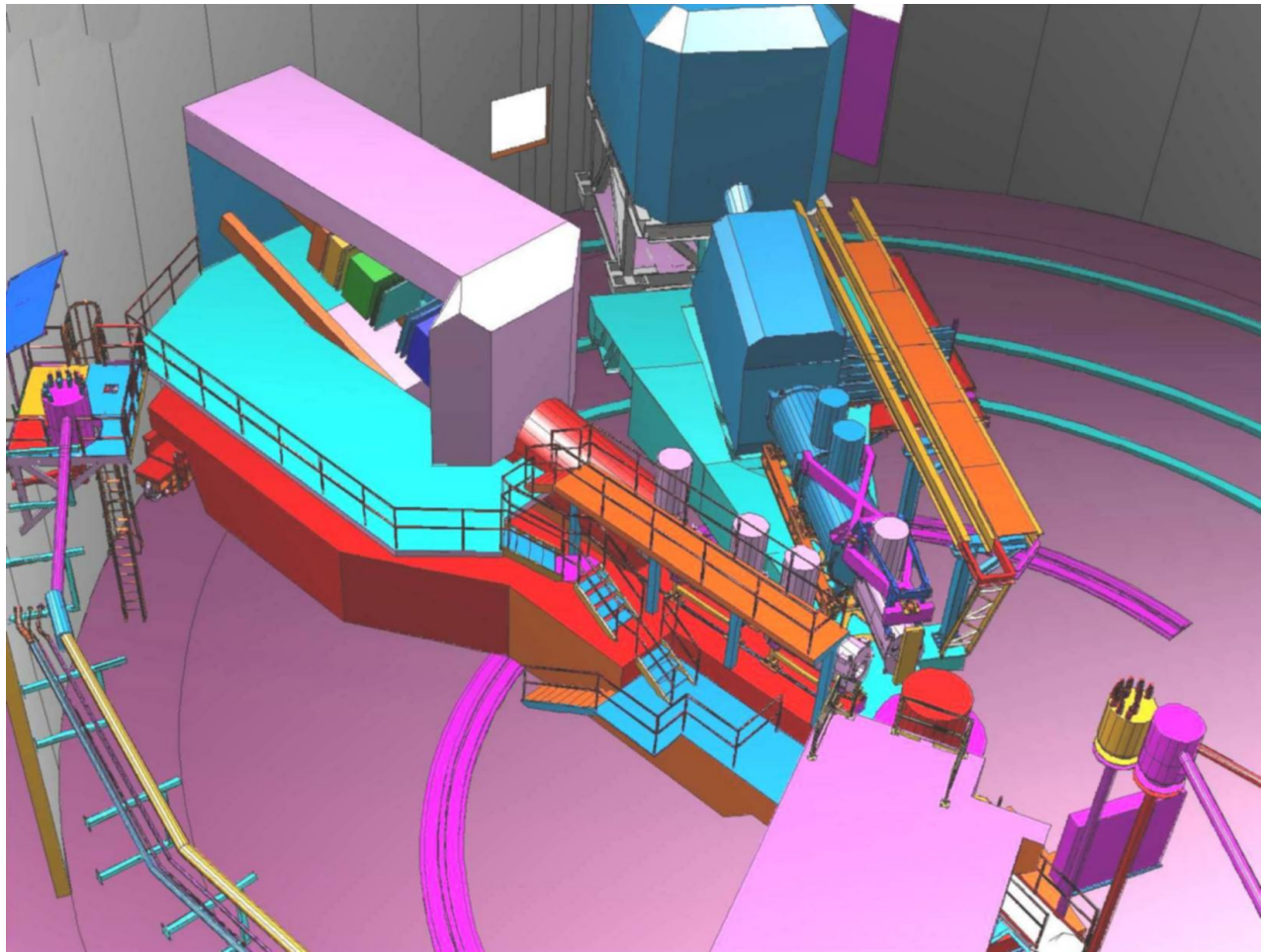


Figure 4.3: Artist's Rendering of SHMS and HMS Spectrometers in Hall C. The top of the SOS Spectrometer is in the foreground.

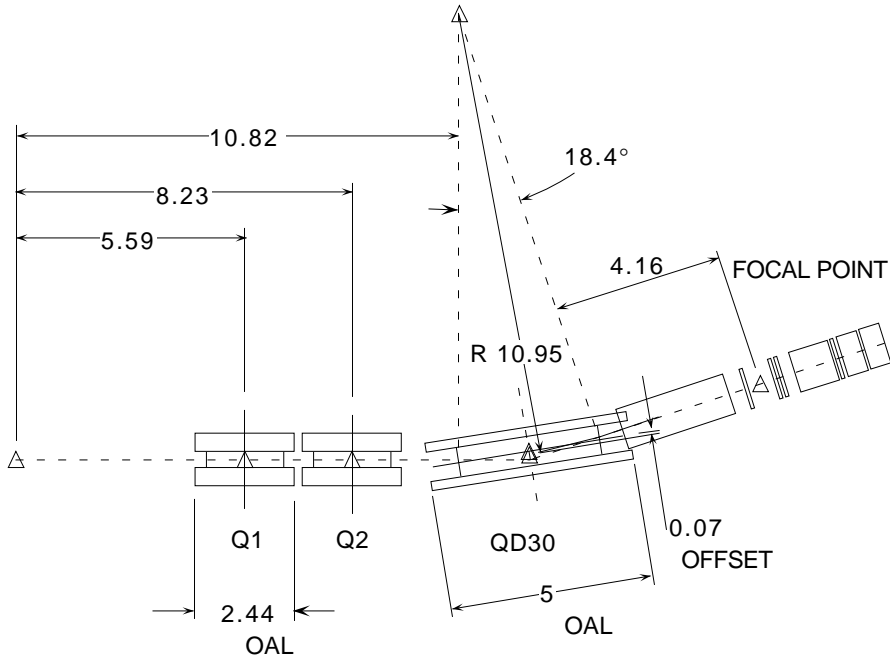


Figure 4.4: SHMS Spectrometer Key Dimensions (meters) showing the location of the two quadrupoles and the combined function magnet relative to the target and the detector stack.

4.3.2.2 Q1 at 8.6 T/m

The SHMS spectrometer requires two quadrupoles with a gradient of 8.6 T/m and 40-cm aperture. The requirement to reach the scattering angle of 5.5 degrees means that the quads must be narrow. The HMS spectrometer Q1 magnet can just reach the required gradient due to the built in margin in operating current. The Q1 and Q2 magnets were designed by Oxford Instruments with a considerable operating margin so that the required gradients for HMS could be reached given some uncertainty in the yoke packing factor and the performance of the then new design of the large cold iron quads. The power supplies, for example, were sized at 1250 amps even though the gradient was predicted to be reached at \sim 1050 amps. The cold iron quads worked as designed and the margin was never called into service. The margin in power supply current was matched by similar margins in the current leads, superconductor critical current, and force containment. The forces at the 8.6-T/m gradient are under evaluation at this time to determine if any internal structural modifications are required. Table 4.2 has the relevant Q1 parameters at the present maximum excitation and, for comparison, those required for SHMS. The force stands out as an area for engineering analysis. The design margins in the present Q1 are very comfortable but much of this is lost at the higher excitation. Figures 4.5 and 4.6 show the gradient field quality and saturation at 8.6 T/m. Both are reasonable and meet the requirements.

The project plan for SHMS is to procure, through competitive contracting, two Q1 magnet systems with a slightly thicker yoke shell to compensate for the \sim 50% force increase. This modification will add a few centimeters to the overall size of the yoke/shell combination.

Parameter	HMS	SHMS	Change
Gradient (T/m)	7.11	8.59	20.8%
Current (A)	1010	1291	27.8%
Pole Tip Field (T)	1.78	2.15	20.8%
Field in Iron (T)	3.72	3.82	2.7%
Coil Forces (N)	Fx 28,571	44,062	54.2%
(Coil Stack 1)	Fy 7,465	-12,604	68.8%

Table 4.2: Q1 comparison between HMS at 1010 amps and SHMS at 1291 amps.

The SHMS power supply will be rated for 1350 amps, an increase of $\sim 10\%$ over the present HMS Q1 supply. Similarly, the energy dump resistor will have to absorb a higher stored energy.

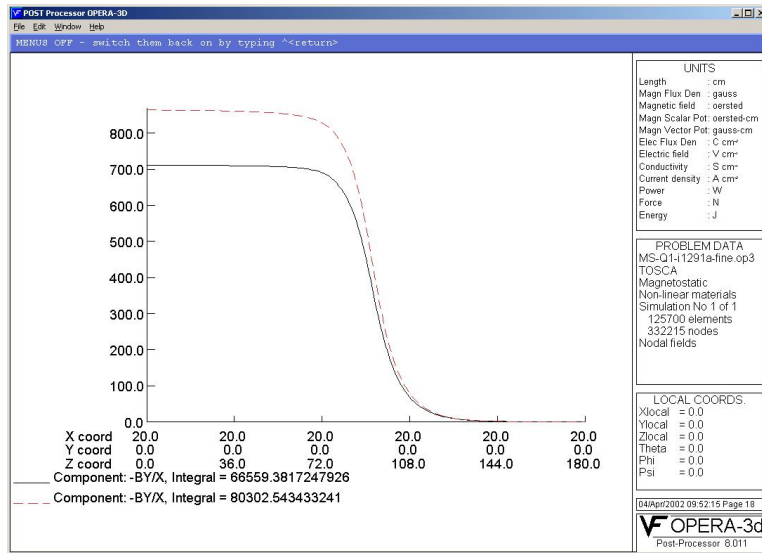


Figure 4.5: Q1 Gradient Comparison along Z.

4.3.2.3 QD30 Superconducting Magnet for the SHMS

The spectrometer requires a combined function superconducting magnet that can simultaneously produce a 4.0-T dipole field and a 3.0 T/m quadrupole field inside a warm bore of 30 cm. A magnetic design using TOSCA 3-D[32] has been performed to establish the basic magnetic requirements, provide 3-D field maps for optics analysis, and produce basic engineering information about the magnets. A four sector cosine theta current distribution and a two sector cosine two-theta quad design with warm bore and warm iron has been selected and analyzed. A cut-away drawing is shown in Fig. 4.7.

The magnetic design uses TOSCA-generated cosine theta type coils with “constant perimeter ends”. These coils closely approximate the ideal cosine geometry that would

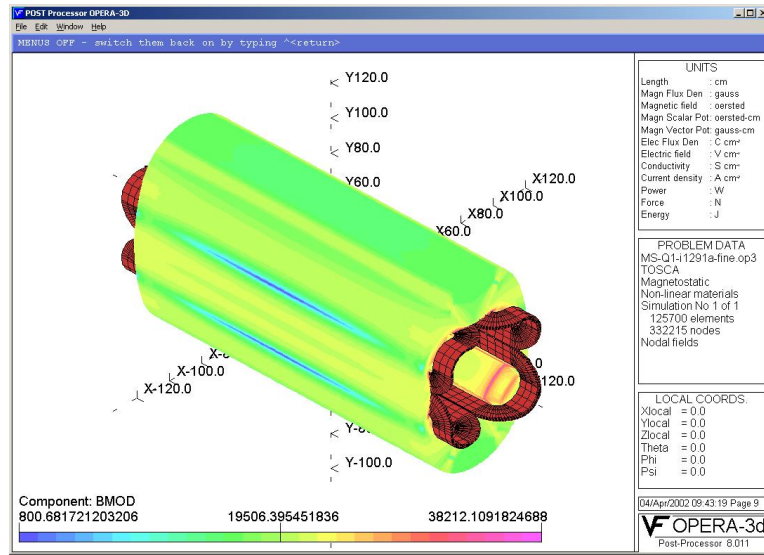


Figure 4.6: Magnetic Fields in Q1 at High Current.

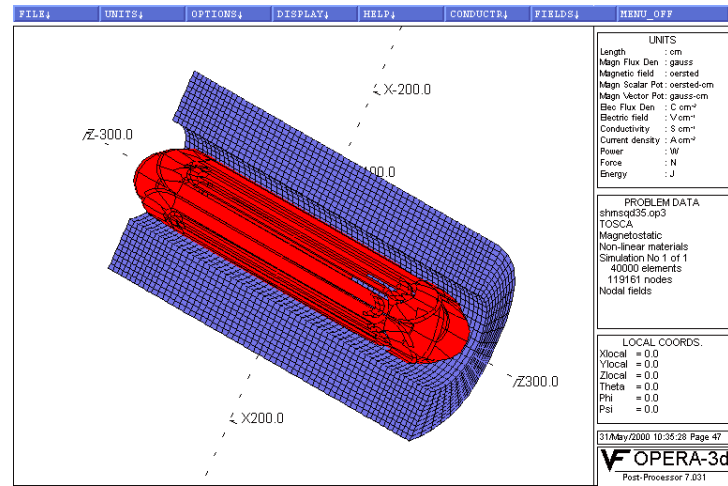


Figure 4.7: Cut-Away View of QD30 Magnet with beam-left side of yoke removed. Orientation is with bend field horizontal. Perspective angle is such as to make the image appear approximately as installed.

be a perfect generator of high purity fields. Practical considerations such as finite current distributions, a limited number of sectors, and TOSCA's internal approximations, all contribute to deviations from the ideal geometry and are the sources of higher order field errors in the design. The yoke is modeled as non-linear iron with the nominal properties of 1010 steel. It is 4.2 m long with an outer elliptical shape having radii 120 cm 100 cm and a 60-cm inner circular radius. The detailed shape of the yoke is not very important in a cosine type magnet as the design requires an unsaturated yoke for good internal fields. The high field region is either on top or on the bottom depending on the relative sign of the dipole and quadrupole coils, therefore an elliptical yoke represents an ideal solution.

The QD30 combined function magnet produces a 4.3-T peak field in the bore and a peak field in the windings of 5.4 T (see Figs. 4.8 – 4.11). These fields are comparable to those achieved in large bore magnets produced 20 years ago for MHD research, particle spectroscopy and coal sulphur separation. There are significant differences between the present magnet design and these prototypes. For example, the stored energy of the QD30 is somewhat less even though the field volumes are comparable. This is due to the fact that the superposed quadrupole field produces significantly less stored energy for a given maximum field. The combined fields also produce a very asymmetric resultant field and force distribution. The fields add on the bottom of the magnet and subtract on the top, so the fields across the bore range from ~ 0 to ~ 5 T. Similarly the fields in the windings are highest where the fields add (5.4 T) and nearly -2 T where they subtract. Thus there is a net force between the yoke and coil that must be dealt with due to the asymmetry. The peak linear force densities are 40,000 pounds per inch for the dipole winding and 11,000 pounds per inch for the dipole winding. These forces add on one side and subtract on the other yielding peak pressures that range from 4680 psi to 2100 psi. Simple pressure vessel computations for 20-ksi material stress yields a 6.0-inch thickness for the cold mass force collar. Due to the large radial thickness of the windings (3.5 inches) and cryostat (11.8 inches), the required 6-inch pressure shell is easily accommodated without stressing the coil cold mass. Obviously in a real cold mass the stress will be distributed and the resulting stresses lowered. The large size of the cryostat will allow separate fluid pressure vessels in accordance with the ASME code. This will greatly simplify the final design and result in a much more conservative magnet. A fully clamped winding is planned for the final construction.

Cryogenic stability of the QD30 quadrupole and dipole has been evaluated against the Steckly criterion, α . The condition of stability is that α must be less than one, which means that the velocity of spread of a normal zone is negative. That is, a normal zone will always shrink. Analysis shows that α is 0.79 and 0.48 for the dipole and quadrupole coil designs, respectively.

4.3.2.4 Magnet DC Power and Energy Dump System

The DC power system for the SHMS magnets will consist of four independent power supplies. These supplies will be 12-pulse SCR supplies with a final stage transistor regulator providing stability of 10 ppm. They will be low voltage high current commercial units readily available from Danfysik and others. A DC current of 5000 amps at 10 volts would be a reasonable choice for SHMS due to the relatively low inductance (0.72 H), and would provide a charge time under 30 minutes. The Quad power supplies will be identical to those in use on HMSQ1

Function	Combined Quadrupole – Dipole	
Bore	30 cm Warm	
Overall Length	5.0 m	
Outer Diameter	3.2 m	
Yoke	240 kilopound (kip) warm 1010 steel. Length: 4.2 m. Outer envelope: ellipse with half-axes 1.2 m \times 1.0 m. Inner envelope: 0.6 m radius circle.	
Coil and cryostat	40 kip St.Steel 5 m Long, 0.6 m (0.3 m) outer (inner) radius	
Stored Energy	13.0 MJ	
	Dipole	Quadrupole
Amp-Turns	3.3×10^6	1.8×10^6
Current Density	$5600 A/cm^2$	$5040 A/cm^2$
Coil Sectors	4	2
Winding	$\cosine(\theta)$	$\cosine(2\theta)$
Magnetic Strength	12.50 Tm	11.48 (T/m)m
Central	Field 3.58 T	Gradient: 3.63 T/m
Effective Length	3.45 m	3.4 m
Uniformity	$dB/B \sim 1 \times 10^{-3}$	$dG/G \sim 1 \times 10^{-3}$
Peak force density	40 kip/in	11 kip/in
Peak pressure	3390 psi	1290 psi

Table 4.3: SHMS QD30 Magnet Parameters

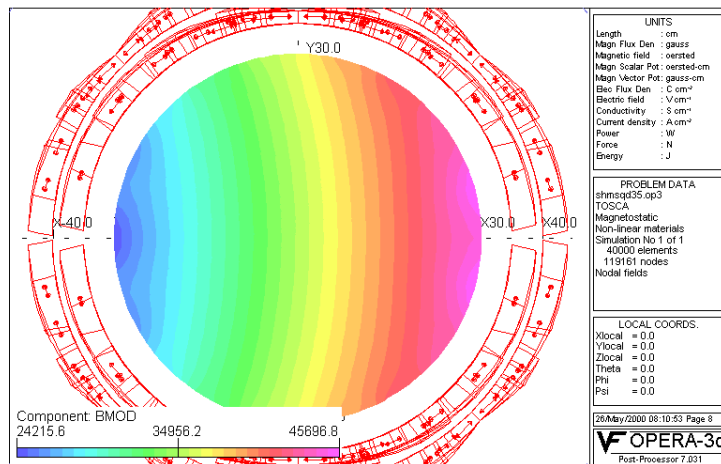


Figure 4.8: BMOD in QD30 Midplane (Gauss).

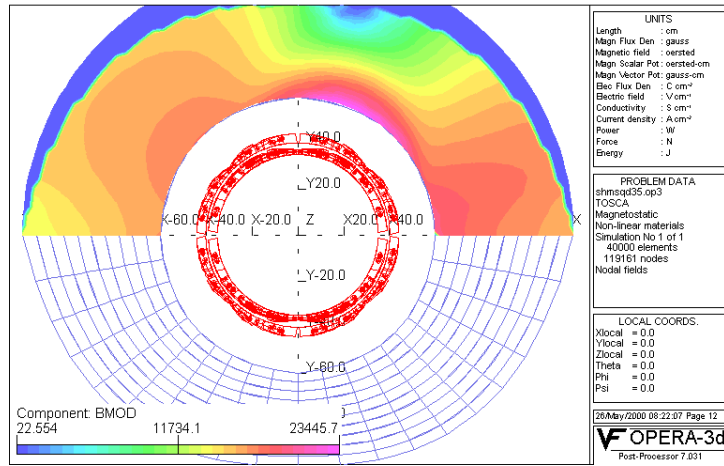


Figure 4.9: QD30 Yoke Saturation-Bmod (Gauss).

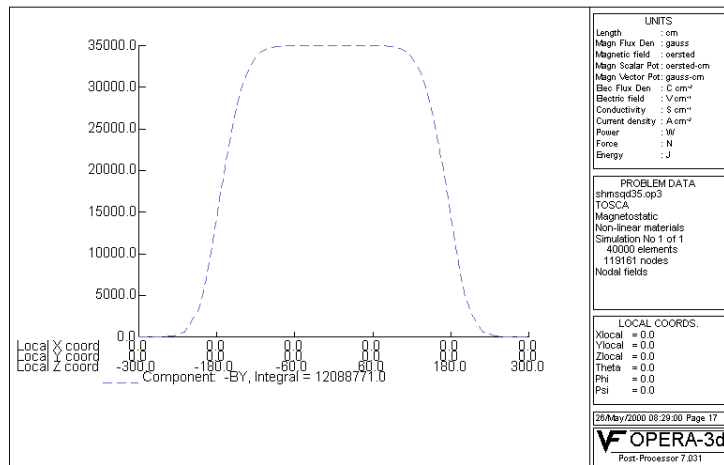


Figure 4.10: QD30 B_y and Integral from $z = -300$ to $+300$

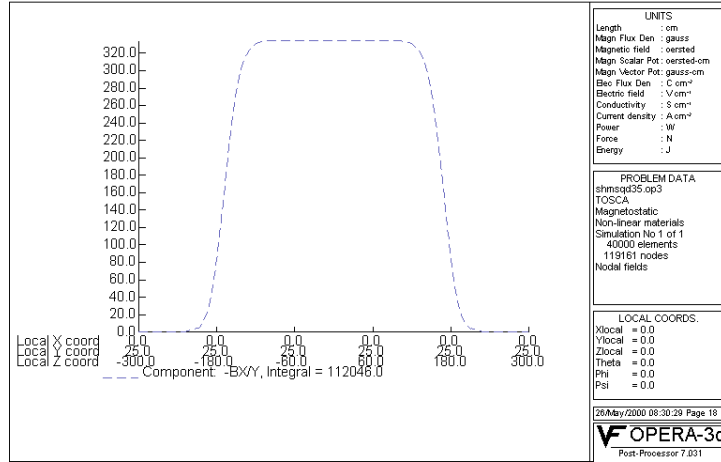


Figure 4.11: QD30 Integral B_x/y from -300 to 300 and gradient at (0,25,0)

and the QD30 magnet supply will be similar to the new HMS dipole power supply. All of the supplies will provide ~ 10 volts for ramp-up or ramp-down, have polarity reversal switches, and the possibility of NMR control for the dipole coils.

The energy dump systems will consist of a 10 volt ramp-down, a slow dump and a fast dump resistor. The fast dump for the Quads will provide 450 volts while the fast dumps for the QD30 magnet will apply a voltage of 150 volts to the dipole coils and 250 volts to the quad coils. These voltages may increase as the design progresses to maintain a reasonable final coil temperature near 80 K. The large cold mass and moderate current densities insure that sufficient material is available to absorb a large fraction of the stored energy at a low final temperature during a quench discharge. The QD30 magnet circuits will have dump resistances such that the time constants are equal so that both coils will discharge at the same rate. The design is such that in the event of a discharge of one coil set, the second set will see a voltage which mimics a quench and a discharge of the second coil will be initiated. The possibility of a real second coil quench is also likely due to eddy current heating in the stabilizer material.

4.3.2.5 Magnet Control System

The SHMS magnets will have a control system that is self contained and able to be operated remotely by EPICS. The magnets' internal controls will take care of interlocks, operating valves by PID, and converting information from the magnet into engineering units. The EPICS system will allow operation from remote screens, archival data logging and graphic display. A dual processor PLC designed for critical fail safe process control will be used. Such PLCs can switch the process control from primary to secondary in ~ 50 ms in the event that the primary processor fails. They can also be switched manually or by software for routine maintenance. The use of dual processor PLCs can reduce if not eliminate the nuisance of radiation induced local processor lockup. The PLC will use a combination of commercial electronics and PLC I/O modules for signal acquisition. Liquid level control and cryogenic

thermometry is straightforward to provide using commercially available units. Readouts of magnet voltages, pressures, strain gauges and valve position LVDTs will be performed by standard PLC plug-ins.

4.3.2.6 Support Structure

The SHMS support structure will be a welded steel frame riding on steel wheels and a center bearing. The structure will be built from prefabricated sections that must be welded together in the Hall. The steel structure will have a main beam section that will carry the entire spectrometer. The entire beam and spectrometer will ride on large hinged steel wheel bogies and floor mounted rails to allow precise scattering angle changes. This system is similar to that used in the HMS and SOS spectrometers. The steel fabrications will be hollow welded structures similar to ship hull sections. As such they will have internal access to permit complete welding of all seams and joints. The wheel sections will be driven by motors and reducers with variable frequency drives. The wheels are planned to be conical sections that are machined at the proper angle to control the radius of rotation. The use of the successful “Bertozzi” hinges on the wheel assemblies to eliminate the large radial forces that arise from even small misalignments is incorporated in the design.

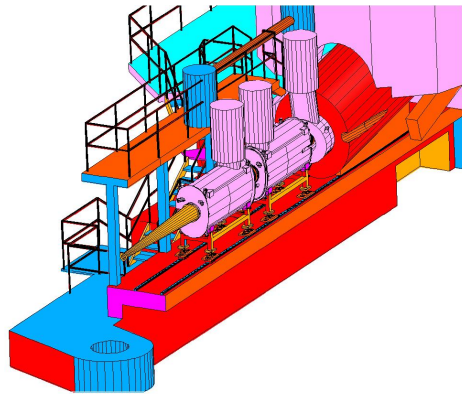


Figure 4.12: SHMS Pivot with Slider.

4.3.2.7 Spectrometer Motion System

The SHMS spectrometer has a required range of motion from 5.5 degrees to 25 degrees. These two orientations are shown in figures 4.13 and 4.14. Proximity detectors will insure that the system always moves in a safe angular range and that obstacles are avoided. Positioning accuracy consists of three components: angular measurement, pointing control, and distance from pivot. The scattering angle positioning tolerance will be 0.01 degrees, the pointing tolerance will be ± 0.5 mm, and the distance off the pivot will be constant to within ± 1 mm. While it may be possible to measure these quantities more accurately, these are the spectrometer setting tolerances. Note that this is similar to what has been obtained with the HMS. The scattering angle will be measured by a shaft encoder that can detect an angle

change of 0.003 degrees. A scale etched into the floor at the radius of the rear drive wheels and viewed by a video camera with a graticule lens will confirm the scattering angle setting. Pointing and distance from pivot will be controlled by a large central crossed roller bearing. The accuracy of such bearings is a few thousandths of an inch. A view of the pivot showing simultaneous connection of the SHMS, and SOS, and the HMS, is provided in Fig. 4.15.

The motion of the SHMS spectrometer will be coordinated by a stand-alone PLC that integrates the drive wheel motion, angle read-back, proximity sensors, and obstacle detection. The rotation motion will be limited to a preprogrammed range set in EPROM in the PLC and by the proximity detection. This design is similar to the HMS rotation control system.

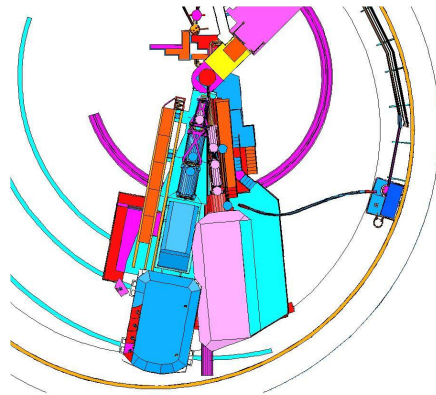


Figure 4.13: SHMS at 5 degrees. HMS at 10.5 degrees.

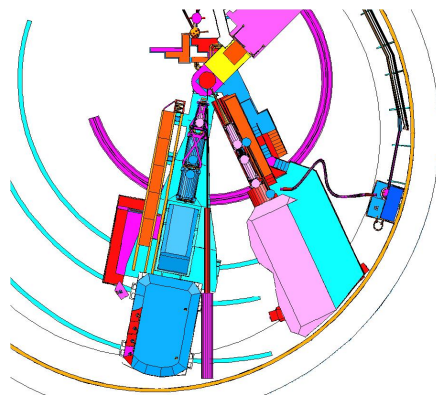


Figure 4.14: SHMS at 25 degrees. HMS at 10.5 degrees.

4.3.2.8 Shield House

The SHMS spectrometer shield house will be a reinforced cast concrete structure that is built on the steel carriage. The concrete thickness will be 100 cm on all sides except toward the pivot where it will be 200 cm. The concrete is formed and poured in place. A conventional

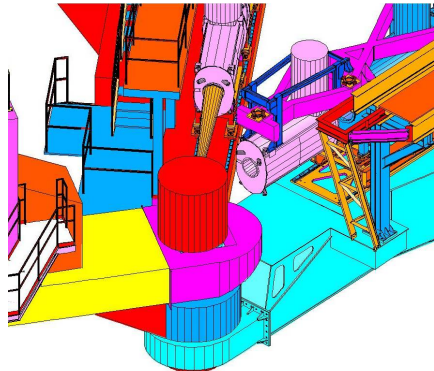


Figure 4.15: Hall C Pivot with (from left) SOS, SHMS, and HMS Attached.

concrete mix will be used with added borate to absorb thermal neutrons. The interior walls, floor and ceiling will have a minimum 2-inch thick lead lining except for the front wall which will have 3 inches of lead. The lead will be covered and constrained by a system of aluminum plates and C channels. The SHMS detectors will be mounted on a transverse rail system so that the detectors may be easily removed for servicing and relocated accurately. The shield house will be accessed by a door that is hinged to open outward on the side away from the beam, and a removable block wall. There will be a limited amount of space inside the shield to allow a corridor access on both sides of the detector stack.

4.3.2.9 SHMS Cryogenic System

Description

The SHMS magnets will be designed with a cryogenic interface similar to the existing HMS magnets. Internally the magnets will have thermal siphon circulation from helium and nitrogen reservoirs. The reservoirs will contain dual relief devices: an ASME coded mechanical relief and a rupture disc set at a 25% higher pressure. Exhaust lines for relief which are separate from the cool-down lines will be used so that there will be no chance of a contamination blockage in these pressure relief paths. Temperature sensors, liquid level sensors, and voltage taps will be within the reservoirs. The magnets will have liquid level control and valves to permit independent warm up or cool down using a local heat exchanger. The cryogenic valving will allow for top-fill and bottom-fill of helium and nitrogen for steady operation and for cool-down, respectively. Cold return and warm return shutoff valves will be included to allow smooth transition from cool-down to regular closed cycle operation. The cryogenic supply will use the existing Hall C G0 transfer line including the G0 flex line, vacuum jacketed return lines, flex gas lines and cool-down heat exchanger. The SHMS cryogenic system will use a new cryogenic distribution box mounted on the back of SHMS and a flexible transfer line similar to that constructed for the G0 experiment. The magnets will be connected by JLAB standard U-tubes similar to those used on HMS/HRS quads. A set of gas manifolds installed on the back of the SHMS will collect and return cryogenic gases to the existing Hall C cryogenics system. A stand and a platform are required for support of equipment and for personnel access. The system is completed by automated cool-down

valves and actuators identical to those used on HMS.

Operating modes

During normal operation the SHMS magnets will be fed helium gas at 4.5 K and 3 atm. This gas gets JT expanded at each magnet by a valve that is controlled by the SHMS magnet control system to maintain liquid level. Boil off gas and JT flash will be returned to the local refrigerator at 1.2 atm. and 4.2 K. Nitrogen will be fed to the SHMS at ~85 K and 4 atm. where it is expanded into the N₂ reservoir by a valve under local control. Boil off N₂ will be vented outside. Vapor cooled current leads will be controlled by valves that servo on the SHMS magnet current and adjust the helium gas flow accordingly. Separate flow control and measurement for each current lead is a normal part of this design. Non burn-out current leads are specified. The helium gas from the leads will be returned warm to the End Station Refrigerator compressor suction. The cool-down gas return and N₂ gas return lines will be vacuum jacketed to prevent ice and water from accumulating near the magnets.

Internally the SHMS magnets use thermal siphon circulation. An insulated supply line will feed helium to the bottom of the magnet cryostat and a return line will collect the slightly less dense fluid at the top of the cryostat and return it to the helium reservoir through a stand-pipe. The magnet heat leak will provide the energy to drive the circulation. The pipes are sized for 10 times the design heat load to insure stable thermal siphon flow under all conceivable conditions. The LN₂ system design is similar.

During cool down and warm up, 4-atm. helium gas at 300 K will be blended with a pre-cooled 80-K helium stream on the SHMS in a “cool-down heat exchanger” (CDHXR). This variable temperature source will be controlled by the SHMS magnet control system to provide a 70-K differential temperature for either warming or cooling, and will maintain an internal temperature difference in the SHMS magnet of no more than 50 K. This CDHXR will provide a precise method of warming and cooling the SHMS magnets independently in a manner which minimizes thermal stress due to relative contraction. This technique will also provide increased cryogenic efficiency.

4.3.2.10 SHMS Vacuum Systems

The SHMS spectrometer will have three vacuum systems dedicated to the operation of a) the QD30 superconducting magnet, b) the SHMS spectrometer vacuum, and c) the Čerenkov detector. The SHMS cryogenic system is presumed to be made leak tight and cryo-pumping so a dedicated vacuum system is not included in the design. The QD30 magnet will also be leak tight, but a vacuum system tailored to leak testing, commissioning and biannual vacuum servicing will be included as a dedicated system. It can be used to commission and service the cryogenic system as needed. It will be portable, self contained, and fully instrumented. The spectrometer and Čerenkov vacuum systems will be dedicated to those devices and will be permanently installed on the SHMS.

The pumping system for the QD30 magnet will consist of a turbo pump backed by a direct drive roughing pump. A 1000 liter per second turbo pump with a full port gate valve, roughing bypass manifold and leak testing manifold will be required. The wheeled pump station will have a mechanical 30 – 0 – 30 vacuum gauge, high range and low range thermocouple gauges, and a cold cathode ion gauge. A dedicated RGA for system commissioning

will be needed. A large full port cold trap that can be piped in for system startup and mounted on a separate wheeled cart is included in the specification. Appropriate auxiliary vacuum hoses, valves and flanges to facilitate connecting to all the SHMS vacuum systems will be provided as well.

The SHMS will have thin aluminum entrance and exit windows. The windows will be hydro-formed spherical shapes similar to those in use on the HMS. The spectrometer vacuum between these windows will be maintained by a large mechanical pump and roots blower as a roughing system, and a 1000 l/s turbo pump.

The Čerenkov vacuum and gas system design is similar to the above but includes the capability of introducing other gases besides helium. This system will be dedicated to providing the correct Čerenkov atmosphere and will have differential pressure relief valves to limit the operating pressure range. Appropriate monitoring equipment to verify that the correct index has been achieved will be necessary. An arc cell system and a hygrometer will be used for quality control of the process. The Čerenkov system operates first with a nitrogen purge to dry the system, then the nitrogen is displaced with the detection gas. A small volume purge of the detection gas may be maintained to permit monitoring of gas quality.

4.3.3 SHMS Optics and Monte Carlo

SHMS Optics Design

The goal of the SHMS design was a compact, general purpose spectrometer similar in properties to the HMS, but with a higher maximum momentum setting for experiments that will use the 11-GeV beam available in Hall C from the CEBAF upgrade. The SHMS needs to be compact in order to fit into the forward-angle space now used by the SOS spectrometer, with angular range from 5.5 to 25 degrees, and a minimum angle with respect to the HMS of 16 degrees. The design process also sought to minimize the cost. A summary of the design parameters is given in Table 4.4.

To achieve these goals, the SHMS was designed as a vertical bend, QQ(QD) spectrometer. Two quadrupole magnets are followed by a combined function magnet that includes both quadrupole and dipole elements. This is similar to the HMS optical layout, except that the last quad and the dipole have been superimposed to make the spectrometer compact.

The first two quads are copies of the HMS Q1 magnet. Re-use of this design helps keep costs low, and the performance of these magnets is well known. The QD is a new design, the engineering details of which may be found in section 4.3.2. Because of the large fields required to bend 11-GeV electrons in a compact spectrometer, the QD must be superconducting, without iron pole-faces. The coils are enclosed in a cylindrical shell of iron, which serves as a flux return yoke. This configuration is very compact, and relatively inexpensive to build. However, it is not a true QD magnet. That would require a toroidal iron shell, and similarly curved coils. A true QD magnet would be very expensive to build, and the performance of the SHMS with a cylindrical QD is adequate.

The SHMS design is very flexible. The coils in the QD are separately excited, and the magnets and detectors will have adjustable positions, making many tunes possible. We consider two here: the original Small Solid Angle (SSA) tune used to design the spectrometer, and a Large Solid Angle (LSA) tune, with all magnets and detectors moved forward

Parameter	Requirement
Range of Central Momentum	2.5 to 11 GeV/c
Momentum Acceptance	-15% to +25%
Momentum Resolution	< 0.2%
Scattering Angle Range	5.5 to 25 degrees
Target Length Accepted at 90°	50 cm
Horizontal Angle Acceptance	±18 mrad
Vertical Angle Acceptance	±50 mrad
Solid Angle Acceptance	4 msr (LSA tune) 2 msr (SSA tune)
Horizontal Angle Resolution (yptar)	2-4 mrad
Vertical Angle Resolution (xptar)	1-2 mrad
Target resolution (ytar)	0.2 - 0.6 cm
Maximum Event Rate	10,000 events/second
Maximum Flux within Acceptance	~ 5 MHz
Minimum Acceptable e/h Discrimination	1000:1 at 98% efficiency
Minimum Acceptable π /K Disc.	100:1 at 95% efficiency

Table 4.4: Design Specifications for the SHMS

2.32 meters as a rigid body.

Several tools were used in designing the SSA tune. The first of these is TOSCA[32], a finite-element, 3-D magneto-statics program. The results discussed here come from the ‘QD30’ TOSCA model of June 5, 2000. TOSCA calculated the field values on a 3-D grid inside the magnet, and a model was fit to the horizontal, or y field component on the $y = 0$ plane (the vertical mid-plane, or symmetry plane of the magnet.) A ray-tracing program was then used to numerically integrate the equations of motion for an electron in the model’s field. This determines the trajectory of the central ray in the spectrometer.

Early in the design process, the total bend angle was fixed at 18.4 degrees. This is essentially the maximum that can be allowed without limiting the acceptance through the QD magnet. An important point to realize is that the quadrupole fields in the QD bend the central ray. Optimizing the spectrometer performance involved tuning the Q/D ratio, and this required compensatory changes in the dipole strength in order to preserve the correct bend angle.

It should also be noted that the central ray has to be offset from the exact center of the QD to avoid cutting off the acceptance by the magnet entrance and exit. Monte Carlo simulations showed that an offset of 7 cm in the center of the magnet combined with a beam-pipe transition at 200 cm from the QD center would optimize the acceptance. This layout is shown in Fig. 4.16. A complex transition pipe is needed to join the QD to the neighboring quad magnet. As long as this pipe does not intrude into the hatched area, it will not impact the acceptance.

With a central trajectory specified through the QD, the optics of the spectrometer as

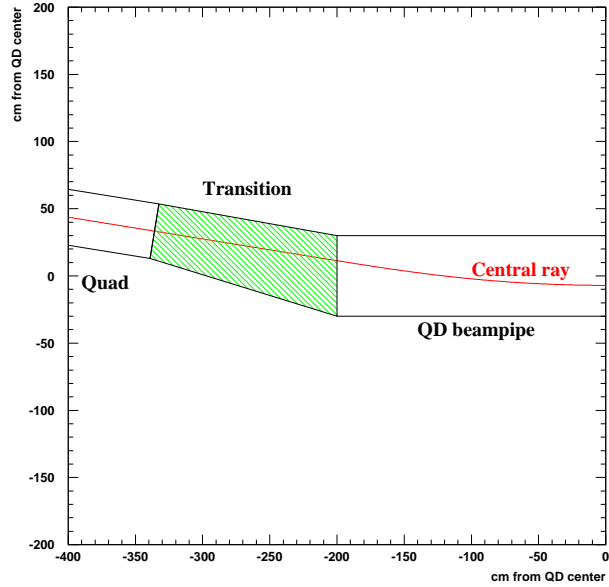


Figure 4.16: Track of the central ray from the exit of the last quad through the first half of the QD. The picture has been rotated so that the QD beam-pipe appears horizontal.

a whole could be studied. The optics are defined by map functions that transform the trajectory of a particle at one location to its trajectory at a different location. We used the COSY[33] program to calculate 5th order Taylor series polynomial expansions of both the global map from target to detectors, and the individual sequential maps that transform from one significant aperture in the spectrometer to the next. The COSY calculations are based on a model of the spectrometer magnets that we describe below. Concurrent with the map calculations, COSY would track an ensemble of test rays through the spectrometer, and adjust the strength of the first two quads to produce the sharpest focus at the detectors. This process was iterated with manual adjustment of other parameters, such as focal plane position, to optimize the performance. The end result was the standard tune. Parameters of the standard tune are given in table 4.5, and the tracks of 27 test rays are shown in Fig. 4.17.

COSY magnet model

Standard COSY quadrupole elements were used for the two quad magnets, as was done in the HMS optics model. There are no COSY standard elements corresponding to the QD magnet, and it had to be modeled using the general field-map element. Past experience has shown that this requires extremely smooth field-map data, such that the TOSCA field-maps could not be directly used. Instead, field values were calculated from a model fit to the data. The use of a model also allows changes to be made in the fields to simulate small changes in the dipole and quadrupole coil excitations for tuning purposes. This model was also used in the central-ray integrations mentioned above. The form of the model is:

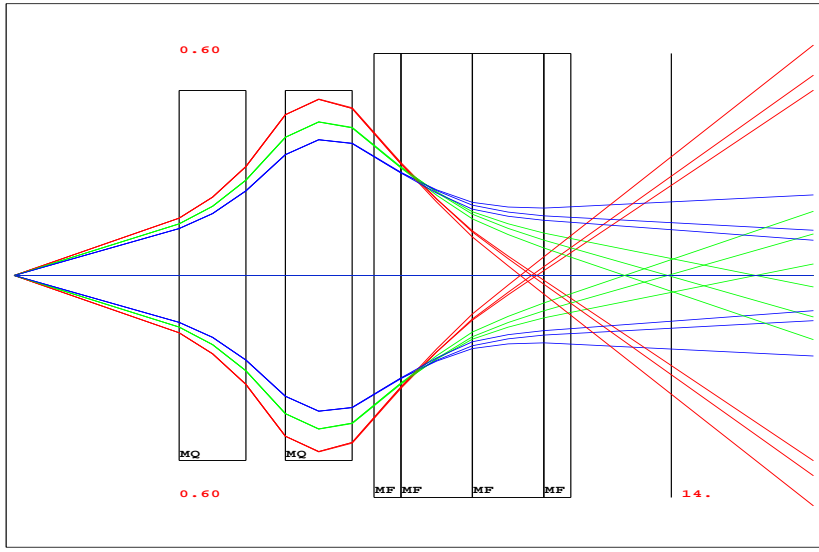
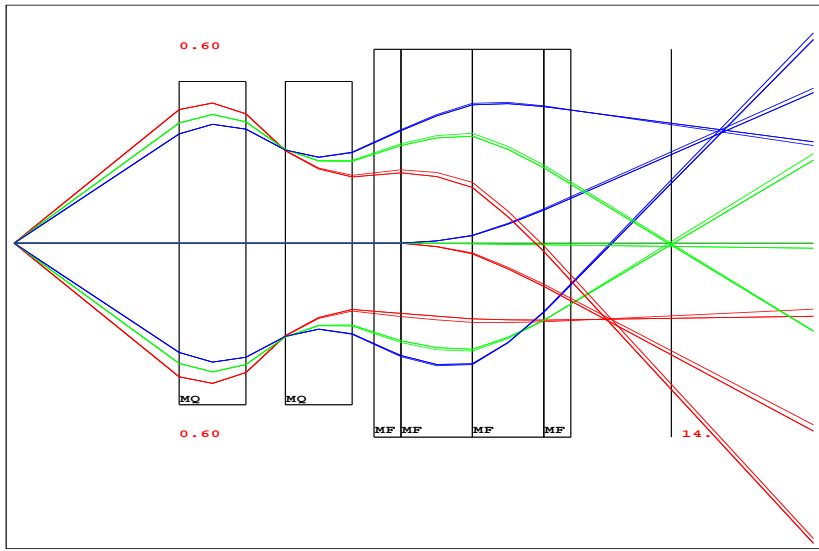


Figure 4.17: Rays Tracked through the SHMS by COSY for the SSA Tune. The upper panel is the bend-plane projection (COSY (x, z) coordinates), and the lower is the transverse projection (COSY (y, z) coordinates). 27 rays are plotted for all combinations of 3 values of total momenta ($\Delta p/p_0 = 0.1$ [blue], 0 [green], -0.1 [red]), 3 values of p_x/p_0 (0.4, 0, -0.4), and 3 values of p_y/p_0 (0.15, 0, -0.15).

$$B_y(x, z) = \sum_{i=0}^6 C_i(z) (x/r_0)^i \quad (4.1)$$

in which (x, y, z) are right-handed Cartesian coordinates with z the axis of the magnet pointing downstream, y is horizontal, and x is in the vertical plane, pointing upwards, with origin the center of the magnet; B_y is the y -component of the magnetic field in the plane $y = 0$; and $r_0 = 30$ cm is the radius of the beam-pipe. For each discrete z_j in the TOSCA data, polynomial coefficients C_{ij}^T were fit to the data using the method of singular value decomposition. Gaussian interpolation was then used to calculate coefficients at arbitrary z :

$$C_i(z) = \sum_j C_{ij}^T \exp(-[(z - z_j)/(s \Delta z)]^2)/(s \sqrt{\pi}) \quad (4.2)$$

where Δz is the 2-cm grid spacing. $S = 2.5$ gives smooth results that accurately reproduce the TOSCA data.

As mentioned above, both the dipole and quadrupole coil excitations needed to be adjusted by small amounts to fine tune the bend angle and optimize the focus. In principle, this could be done by re-running the TOSCA model, but this was not practical. Instead, we use symmetry arguments to treat all the terms in the model that are even-order in x as harmonics of the dipole coils, and the others as harmonics of the quad coils. Thus, we adjusted the dipole excitation in the model by simply scaling the even-order coefficients, and similarly adjust the quadrupole excitation by scaling the odd-order ones. This approximation neglects non-linear saturation effects in the iron and thus is only good for small corrections. The adjusted coefficients are plotted as a function of z in Fig. 4.18. One can see that there are significant higher order terms beyond about $z = 120$ cm, with the C_2 component dominant. Once the final tune is determined by this approximation, a full TOSCA calculation based on the tune values may be performed to verify the results.

LSA tune

The LSA tune is closely related to the SSA tune. It is produced by sliding all the magnets and detectors forward by 2.32 m. The QD is operated with the same fields, so that the central ray follows the same path through the QD and the detectors. The fields in the two quadrupoles were re-optimized by COSY in order to produce a good focus at the focal plane, which was shifted 1 meter farther back from the QD, as measured along the central ray, to avoid tipping the focal plane to too shallow an angle. By having the quads closer to the target, the solid angle acceptance is increased, as is evident from Fig. 4.19, in which we track the 27 standard test rays. However, this tune requires substantially higher quadrupole fields, as listed in Table 4.5. The values listed, corresponding to a central momentum of 11 GeV/c, exceed the capability of these magnets. The maximum central momentum that can be reached in this mode of operation is 8.8 GeV/c, for which Q1 operates at its maximum gradient of 8.6 T/m. Note that with a central momentum of 8.8 GeV/c the SHMS still accepts full energy (11-GeV/c) particles, albeit with somewhat poorer resolution. With the quads moved forward the minimum scattering angle becomes 10°.

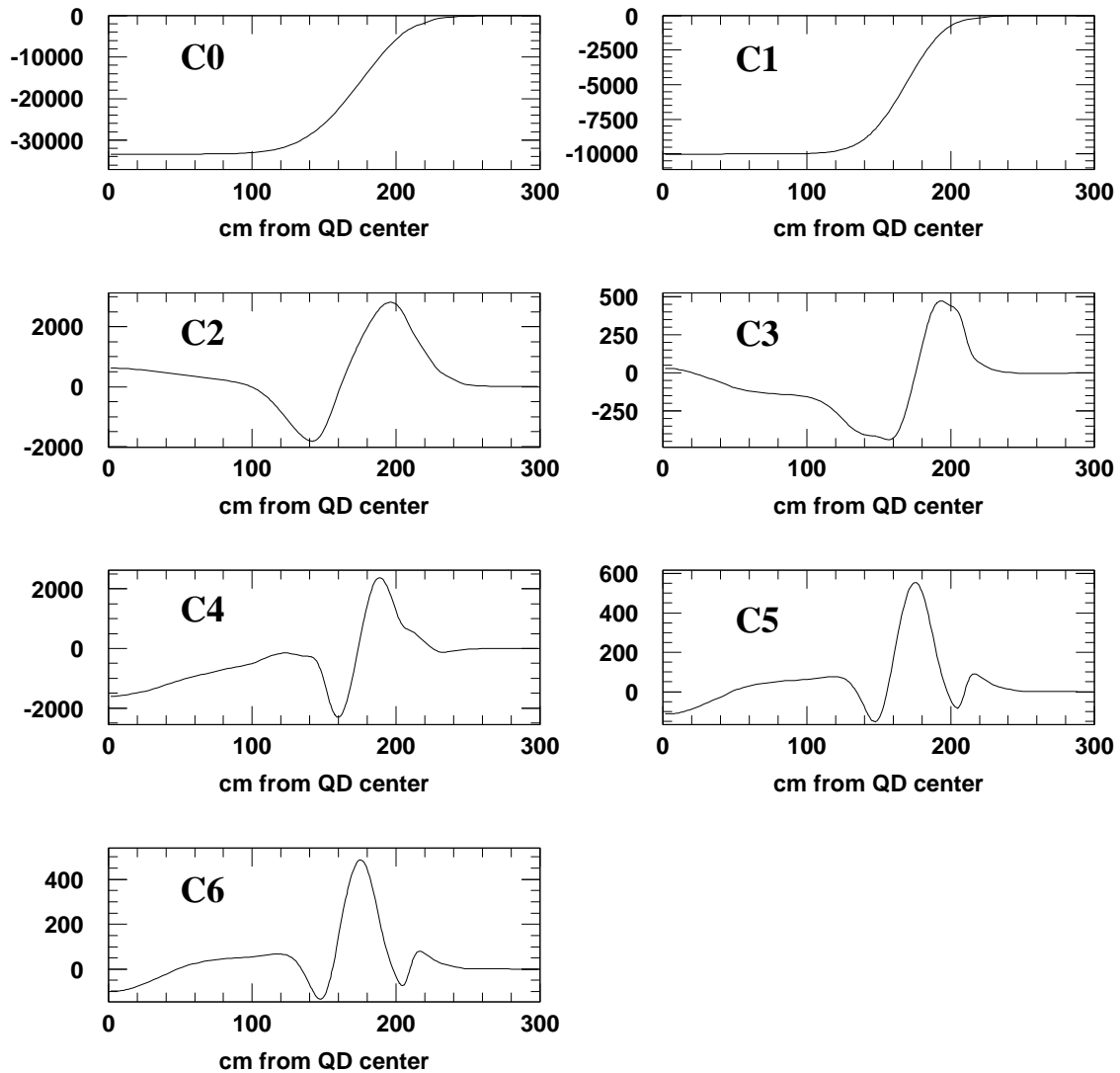


Figure 4.18: Polynomial Coefficients in the QD Magnetic Field Model as a function of z , the axial distance from the magnet center. (The functions are symmetric about $z = 0$.) C_0 is the dipole component, C_1 the quadrupole component, and the others are higher order contributions. The vertical axes are the contribution to B_y at $x = 30$ cm, in gauss.

Parameter	SSA tune	LSA tune
Q1, Q2 mechanical length	189.0 cm	189.0 cm
Q1, Q2 magnetic length	187.9 cm	187.9 cm
Q1, Q2 pole-tip radius	25.0 cm	25.0 cm
Q1, Q2 beam-pipe inner radius	20.5 cm	20.5 cm
Length from target center to Q1 center	558.5 cm	326.5 cm
Length from target center to Q2 center	857.5 cm	625.5 cm
Q1 field gradient for 11 GeV	-7.7069 T/m	-10.7436 T/m*
Q2 field gradient for 11 GeV	8.6041 T/m	9.3790 T/m*
QD beam-pipe inner radius	30.0 cm	30.0 cm
Central ray path-length to middle of QD	1290.0 cm	1058.0 cm
Coordinates of QD center	(1288.2 cm, 20.8 cm)	(1056.2 cm, 20.8 cm)
QD rotation	9.200°	9.200°
Total bend angle	18.400°	18.400°
Layout bend radius	1079.8 cm	1079.8 cm
Coordinates of layout bend center	(1116.6 cm, 1079.8 cm)	(884.6 cm, 1079.8 cm)
Total length of central ray	1850.0 cm	1718.0 cm
Central ray coordinates at focal plane	(1824.3 cm, 177.3 cm)	(1687.2 cm, 208.8 cm)
Field at QD center for 11 GeV	3.3416 T	3.3416 T
Quad component at QD center, 11 GeV	3.3416 T/m	3.3416 T/m
Minimum spectrometer angle	5.5°	10°
Maximum spectrometer angle	25°	25°
Minimum separation from HMS	16°	25°

* Maximum achievable quad gradient of 8.6 T/m limits central momentum to 8.8 GeV

Table 4.5: SHMS Optics Parameters for SSA and LSA Tunes. Coordinates are given as (horiz,vert) distance from nominal target center.

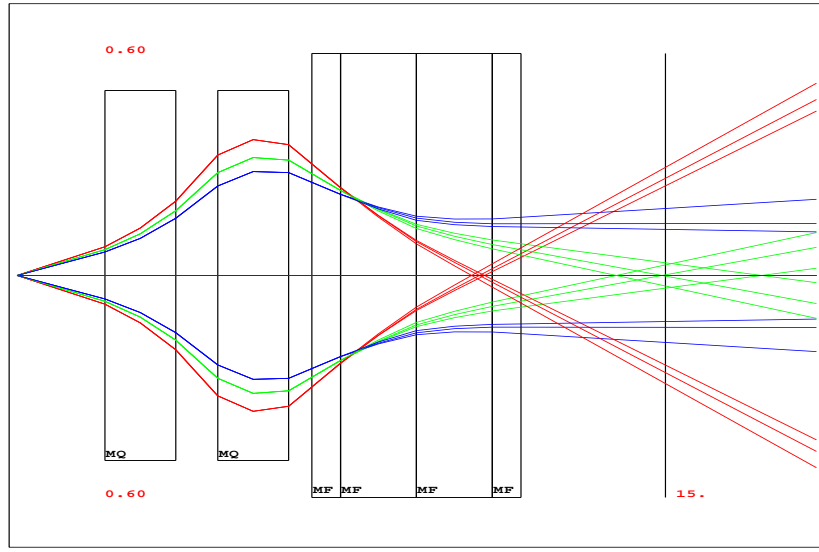
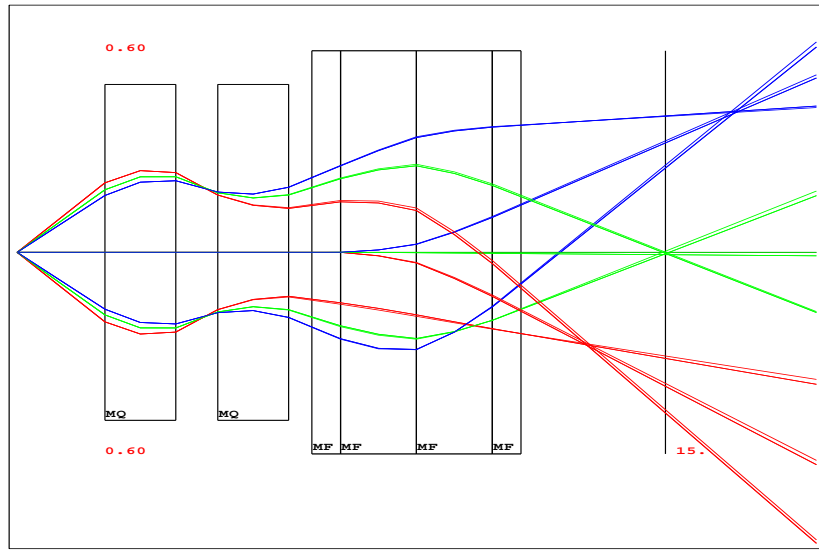


Figure 4.19: Rays Tracked through the SHMS by COSY for the LSA Tune. The upper panel is the bend-plane projection (COSY (x, z) coordinates), and the lower is the transverse projection (COSY (y, z) coordinates). 27 rays are plotted for all combinations of 3 values of total momenta ($\Delta p/p_0 = 0.1$ [blue], 0 [green], -0.1 [red]), 3 values of p_x/p_0 (0.4, 0, -0.4), and 3 values of p_y/p_0 (0.15, 0, -0.15).

SHMS model in the 'physics' Monte Carlo

The field maps generated by COSY have been incorporated into a model of the spectrometer so that detailed simulations can be made of the SHMS acceptance, resolution, and distributions of events at the detectors. COSY-generated transformations are used to propagate particles from the target to each of the important apertures in the spectrometer. In addition, the particle trajectories can be evaluated at each detector package in order to determine the active region needed for each detector.

The SHMS model is of the same format as the existing HMS and SOS models, and so has been added to 'SIMC', the physics Monte Carlo used extensively in Hall C. This allows generation of various physics processes, taking into account the cross sections and event distributions, as well as multiple scattering and energy loss in target, spectrometer, and detector materials, and any relevant particle decays. The SHMS model includes the same level of detail as the models for the existing spectrometer, and so the simulation can be used for detailed and extremely realistic studies under a variety of conditions. In particular, it can be used to determine the acceptance and resolution as functions of target length, collimation scheme, and detector configuration.

4.3.4 SHMS Performance (Resolution/Acceptance)

A stand-alone Monte Carlo has been used to investigate the properties of the SHMS design as developed in the previous section. The Monte Carlo was run with the spectrometer at 90° and a target length of 70 cm. Electrons were generated uniformly over the phase space and sent through the SHMS spectrometer with the central momentum (p_{cent}) set at 7.5 GeV/c. Events were generated over the $\delta = (p - p_{\text{cent}})/p_{\text{cent}}$ range of -40% to 40%, horizontal angle ($y' = dy/dz$) range of ± 100 mr and vertical angle ($x' = dx/dz$) range of ± 100 mr relative to the spectrometer axis. Studies were done with the large solid angle (LSA) tune (spectrometer moved forward by 2.32 m) and the small solid angle (SSA) tune.

Plots of the δ , Y_{tar} , y' and x' acceptance are shown in Fig. 4.20 for the large solid angle (LSA) tune (solid black line) and the small solid angle (SSA) tune (solid red line). Both tunes have a large acceptance in δ and Y_{tar} , the horizontal position. Both tunes have a flat acceptance in Y_{tar} . For the LSA tune, the δ acceptance is flat for negative δ and gradually decreases with increasing positive δ . The SSA tune has a fairly flat acceptance with a drop-off above $\delta = 10\%$. Both tunes have a sharp drop off below $\delta = -20\%$. In designing the size of the detectors, cuts of $-15 < \delta < 25\%$ and $-25 < Y_{\text{tar}} < 25$ cm were used. The plots of y' and x' acceptance in Fig. 4.20 include these cuts. The LSA tune has about twice the x' acceptance of the SSA tune. The acceptance in y' is a little deceptive, since for a *point* target the acceptance in y' for the LSA tune is only slightly larger than for the SSA tune. In Fig. 4.21, plots of Y_{tar} versus y' and x' are shown. One can see a correlation between Y_{tar} and y' , so that the width of the y' acceptance is almost Y_{tar} independent. Plots of Y_{tar} versus x' shown in Fig. 4.21 indicate no correlation between Y_{tar} and x' .

The beam envelope at $z=0$ in the detector hut is plotted in Fig. 4.22 for the LSA tune with cuts of $-15 < \delta < 25\%$ for target lengths of 0.5, 4, 30 and 50 cm. (Note that a 30 (50) cm target viewed at 90° roughly corresponds to a ≥ 70 (120) cm target at $\leq 25^\circ$.) We use the TRANSPORT[34] coordinate system in which +X is down and +Y is beam left. For the 0.5-cm target, one can see the expected hourglass shape of the X versus Y distribution and

with increasing target length the waist of the hourglass expands. In addition in Fig. 4.22, the bottom plots for target lengths of 30 and 50 cm show that to accommodate an increase of the target length by 1.7 times the detectors have to be increased by 1.4 times in the horizontal dimension. The detectors will be built for $-25 < Y_{tar} < 25$ cm, but, where appropriate, will initially only be instrumented for the 30-cm target. The beam envelope is plotted at the exit of various detectors for both the SSA tune (Fig. 4.23) and the LSA tune (Fig. 4.24). In both figures, the upper right plot is the beam envelope at the first drift chamber. The red box is the size of the active area for the drift chambers. The size is ± 55 cm in Y and ± 42.5 cm in X with center at $x = +5$ cm.

The effective solid angle was calculated by generating 100K events over a range of horizontal angle of $\Delta x' = \pm 0.1$, vertical angle of $\Delta y' = \pm 0.1$, $-15 < \delta < 25$ % and $-25 < Y_{tar} < 25$ cm. The effective solid angle, Ω , was calculated as $\Delta x' \cdot \Delta y' \cdot \frac{\# \text{ accepted}}{\# \text{ thrown}}$. The LSA tune has $\Omega \approx 4.0$ msr, while the SSA tune has $\Omega \approx 2.0$ msr.

The resolutions for the target quantities δ , Y_{tar} , y' and x' are plotted in Fig. 4.25 (LSA tune) and in Fig. 4.26 (SSA tune) as a function of δ for 7.5-GeV/c electrons. For these calculations, the assumption was that the pipe which could contain the gas and mirror for the first gas Čerenkov detector will be at vacuum. This Čerenkov detector is primarily intended for experiments in which high resolutions are not needed. The solid blue curve has no multiple scattering nor wire chamber resolution in the Monte Carlo and indicates the limitations of the optics matrix used in the model of the SHMS. For both tunes, the blue line is barely noticeable except near the edges of the δ range, confirming that the optics matrix is adequate. The red dashed curve adds the effects of wire chamber resolutions in the Monte Carlo. The solid black curve adds the effect of multiple scattering. For the Monte Carlo, the hydrogen target cell was a cylinder with radius 3.37 cm and a wall thickness of 0.005 inches. The combination of the scattering chamber window, air and spectrometer entrance window was 0.6% radiation lengths. In the detector hut, the material was the spectrometer's exit window (taken as Mylar/Kevlar material of 0.020 inches thickness in the simulation), air and the material of the drift chambers. The resolutions in y' and x' are relatively independent of δ . The contribution to the resolution in y' and x' from wire chamber resolution and multiple scattering are about equal, while the Y_{tar} and δ resolutions are dominated by wire chamber resolution with multiple scattering having almost no effect at this momentum. The Y_{tar} resolution has a fairly dramatic parabolic dependence on δ . For the LSA tune, the δ resolution has an asymmetric parabolic dependence on δ with a minimum at $\delta \approx -6\%$. For the SSA tune, the δ resolution has a slightly asymmetric parabolic dependence on δ with a minimum at $\delta \approx -1\%$. The average resolutions for δ , Y_{tar} , y' and x' are about 0.05 %, 0.20 cm, 0.8 mr, 0.8 mr for both the SSA and LSA tunes, meeting or exceeding the requirements given in Table 4.4.

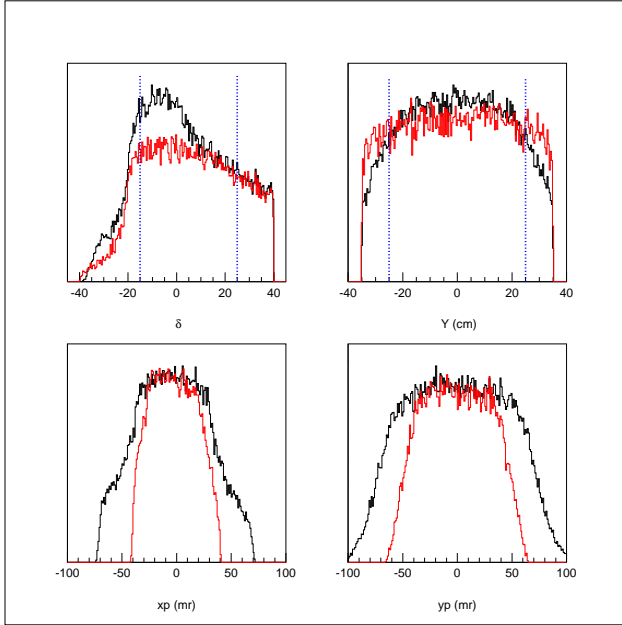


Figure 4.20: The Phase Space Acceptance plotted as function of δ , Y_{tar} , y' and x' for the large solid angle (LSA) tune (black solid line) and the small solid angle (SSA) tune (red solid line). The y-axis is yield in arbitrary units and the LSA and SSA yields have been scaled to match each other at the maximum. The blue dotted lines indicate the limits of $-15 < \delta < 25\%$ and $-25 < Y_{tar} < 25\text{ cm}$ which were used in determining the detector size. The plots of y' and x' include the cuts of $-15 < \delta < 25\%$ and $-25 < Y_{tar} < 25\text{ cm}$.

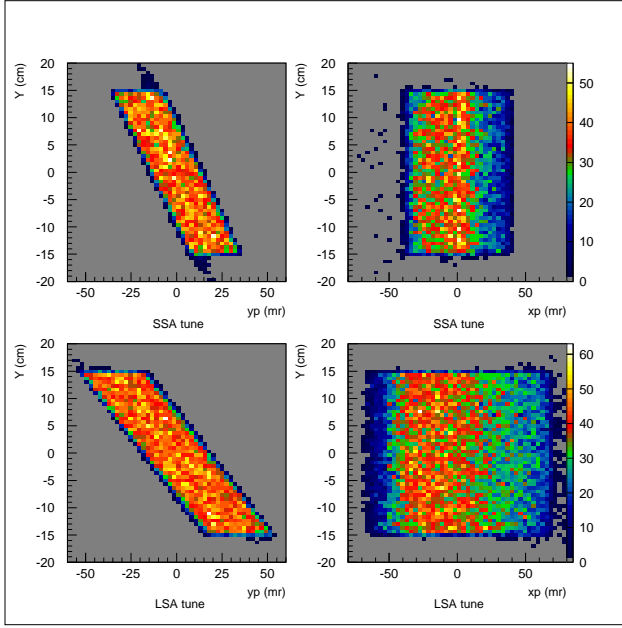


Figure 4.21: Y_{tar} Acceptance. Plots on the left are Y_{tar} versus y' and the plots on the right are Y_{tar} versus x' with cuts of $-15 < \delta < 25\%$ and $-25 < Y_{tar} < 25$ cm. The top plots are with the small solid angle (SSA) tune and the bottom plots with the large solid angle (LSA) tune.

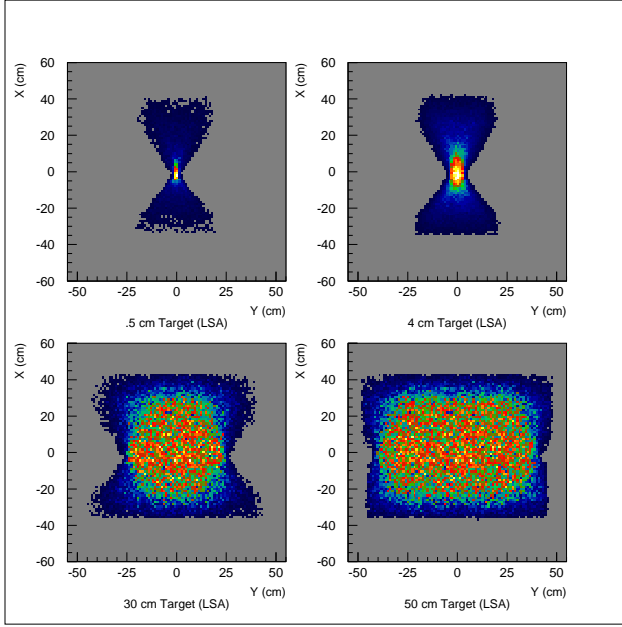


Figure 4.22: Plots of the Vertical X versus the Horizontal Y position at $z=0$ cm in the detector hut for target lengths of 0.5 cm, 4 cm, 30 cm and 50 cm. Spectrometer set for large solid angle tune with a cut of $-15 < \delta < 25\%$.

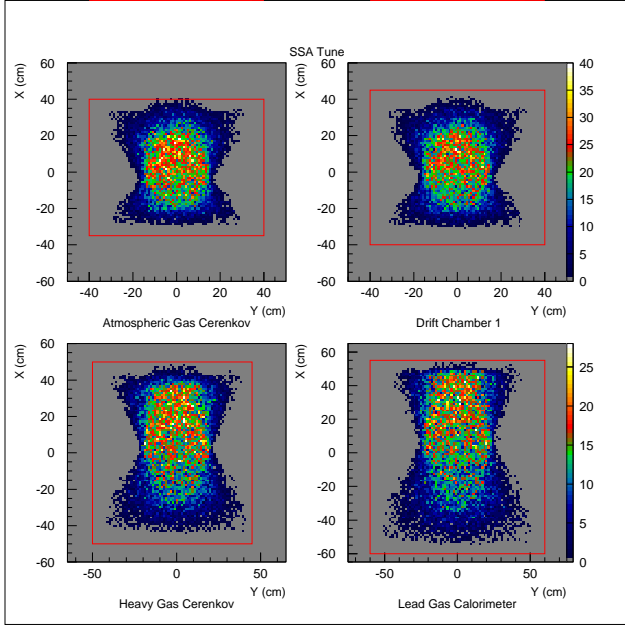


Figure 4.23: Plots of the vertical X versus the horizontal Y position at $z=-60$ cm (*Atmospheric Čerenkov*), $z=-40$ cm (*Drift Chamber 1*), $z=160$ cm (*Heavy Gas Čerenkov*) and $z=320$ cm (*Lead Glass Calorimeter*). Spectrometer set for small solid angle tune with cuts of $-15 < \delta < 25$ % and $-25 < Y_{tar} < 25$ cm.

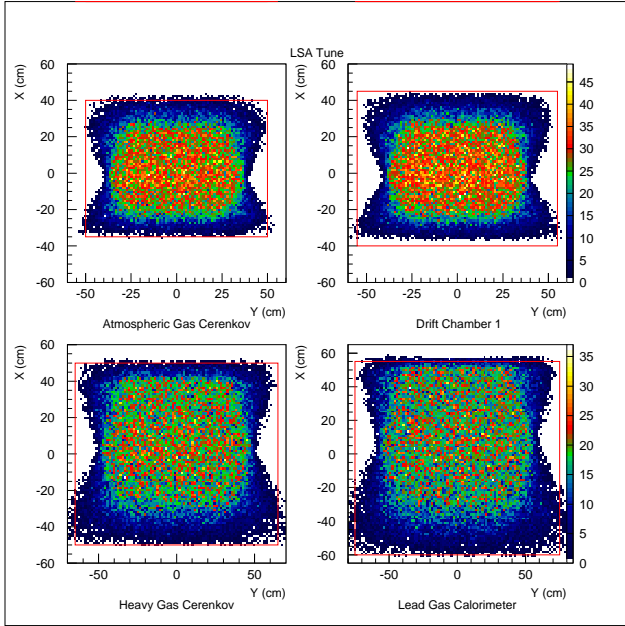


Figure 4.24: Plots of the vertical X versus the horizontal Y position at $z=-60$ cm (*Atmospheric Čerenkov*), $z=-40$ cm (*Drift Chamber 1*), $z=160$ cm (*Heavy Gas Čerenkov*) and $z=320$ cm (*Lead Glass Calorimeter*). Spectrometer set for large solid angle tune with cuts of $-15 < \delta < 25$ % and $-25 < Y_{tar} < 25$ cm.

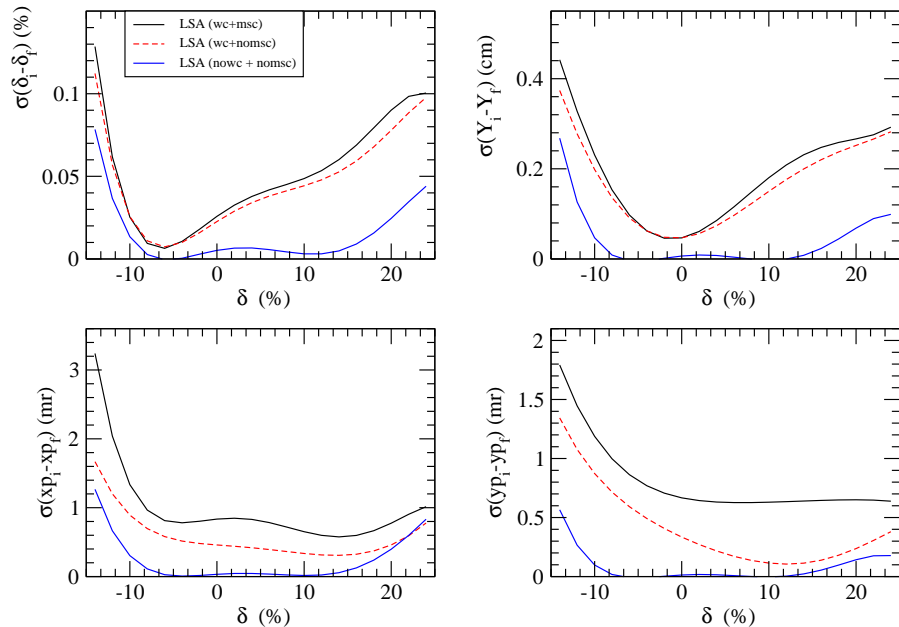


Figure 4.25: For the large solid angle (LSA) tune, plots of the resolutions in the target quantities δ , Y_{tar} , y' and x' as a function of δ for 7.5-GeV/c electrons. The solid black curve is the best estimate of real-world resolutions. The red dashed curve has only the effects of wire chambers resolutions and optics. The blue curve shows the limitation of the optical model. The subscripts f and i refer to the reconstructed and originally generated variables.

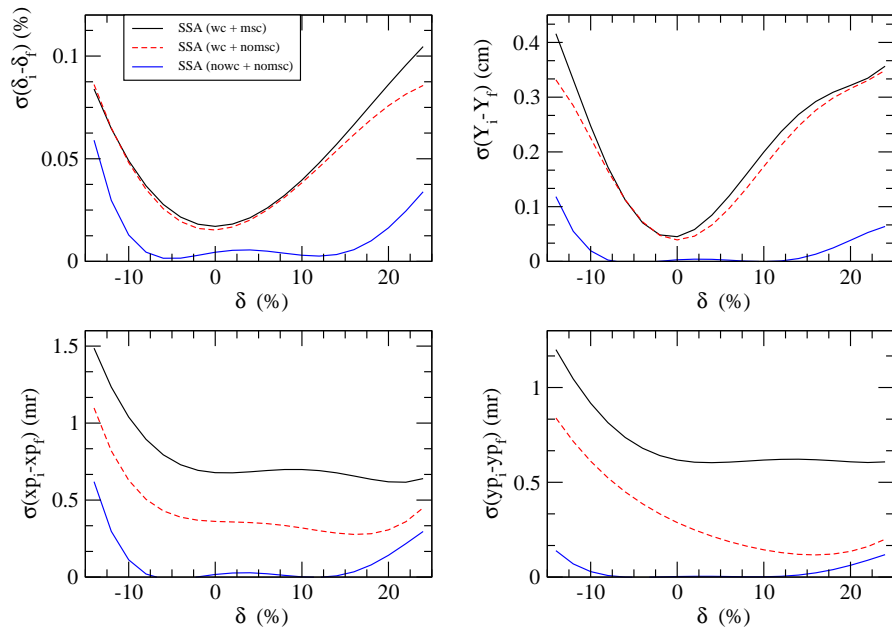


Figure 4.26: For the small solid angle (SSA) tune, plots of the resolutions in the target quantities δ , Y_{tar} , y' and x' as a function of δ for 7.5-GeV/c electrons. The solid black curve is the best estimate of real-world resolutions. Other curves explained in the text. The subscripts f and i refer to the reconstructed and originally generated variables.

4.3.5 SHMS Detector Systems

As the momentum range of a spectrometer changes, so also do the demands on the particle detector elements. At higher momenta, the degradation of angle and momentum resolution caused by multiple scattering become less severe, so that one can consider incorporating a low-mass detector in the upstream regions of the detector stack. The times-of-flight (TOF) of different particle species differ less, making trigger timing somewhat easier, but the same effect makes particle identification by this technique a less viable option. Particle identification using the Čerenkov effect also depends upon the relative speeds of particles, which means that Čerenkov counters must be more thoughtfully designed than at lower momenta, and that other identification techniques should be considered. Higher energy leads to larger fluctuations of the energy deposited in a total-absorption calorimeter, as there is a higher probability that some of the energy leaks out the back. Therefore it is necessary to consider making a thicker shower counter for the SHMS than is used in the HMS.

The above considerations lead us to a SHMS detector system design which would essentially be a HMS stack modified for higher energies. However, new physics initiatives demand the inclusion of new capabilities. Measurement of the polarization of final state particles would require the inclusion of a polarimeter in the SHMS detector stack, for example. Experiments at higher rates or with low signal-to-background would benefit from improved electron/hadron discrimination, such as that provided by the addition of a transition radiation detector (TRD). Pion/kaon separation, primarily achieved by gas and aerogel Čerenkov counters, can be enhanced by recording dE/dx information in the tracking chambers and the TRD. Below, we describe an integrated system of detector components which are optimally matched to one-another and to the physics to be done in Hall C. A block diagram of the proposed detector system is shown in Fig. 4.27. The overall specifications for the spectrometer, developed in section 2.2, were summarized in Table 4.4.

The magnetic optics described and studied in the previous sections of this report provide good resolution over a large acceptance. Further, it allows the possibility of performing experiments with a projected target length as large as 50 cm without giving up good resolution. To detect and measure this full acceptance will require that the detectors cover a large area. The required detector sensitive areas are given in Table 4.6. Our plan is to build the mechanical components of the detectors large enough to achieve full coverage of the 50-cm (projected) target over a 40% momentum bite ($-15\% < \delta < +25\%$). However, until such time as the full acceptance is actually needed by an experiment, only the central regions of the detectors (covering a 30-cm projected target) will be instrumented.

4.3.5.1 Wire Chambers

The SHMS tracking system will provide the only measurement of particle momentum and production angle in the spectrometer. Given an adequate description of the magnetic optics, the momentum and production angles are determined by measuring enough of the track to generate a track vector at the reference plane, then projecting it back to the target.

Although Multiple Coulomb Scattering is reduced at higher momentum, it is still a significant effect limiting momentum and angular resolution, even at 11 GeV/c. We have considered several alternatives to wire chambers for tracking in the SHMS, but conclude that

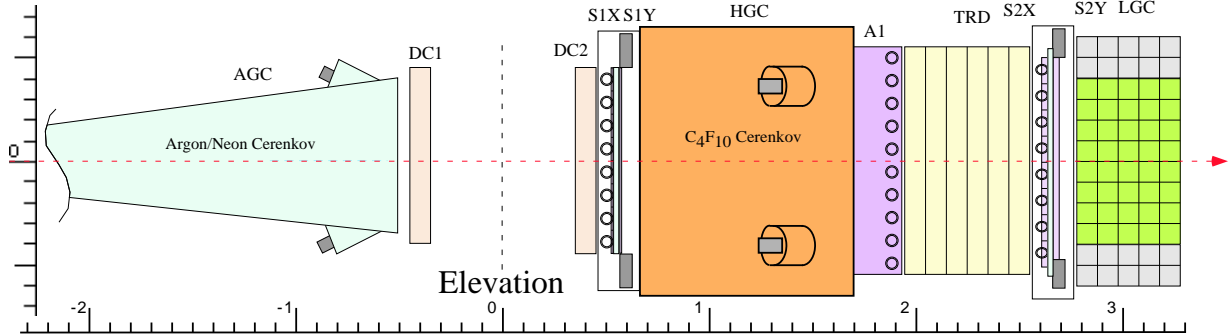


Figure 4.27: Block Diagram of SHMS Detector Arrangement.

Detector	30-cm Target		50-cm Target	
	X size	Y size	X size	Y size
Atm. Gas Č	75	80	75	100
Drift Chambers	85	80	85	110
Scint. Hodo 1	90	90	90	110
Heavy Gas Č	100	95	100	130
Aerogel Č	110	100	110	140
TRD	110	100	110	140
Scint. Hodo 2	110	100	110	140
Shower Counter	115	120	115	150

Table 4.6: Sensitive Areas of the Detectors for Momentum Range $-15\% < \delta < +25\%$, for both 30-cm long and 50-cm long targets.

gas drift chambers remain the best choice to simultaneously provide the necessary position resolution while keeping the detector mass low.

The particular design we have chosen is based upon the successful SOS drift chambers, with only minor modifications suggested by the different SHMS optical parameters and lessons learned from the original design. These chambers provide better than 180- μm single-plane resolution and operate at rates of at least 1 MHz per wire, while placing only about 0.002 radiation lengths of material in the path of particles for a stack of six sense planes. The excellent performance of the SOS drift chambers is demonstrated by the distributions of track residuals shown in Fig. 4.28.

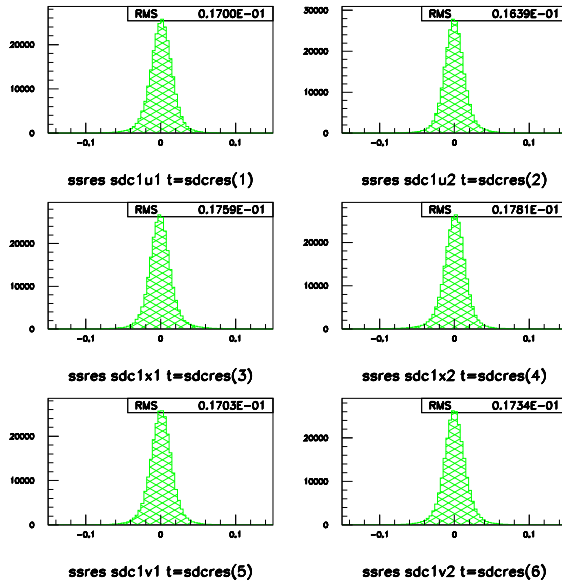


Figure 4.28: Measured Residual Distributions in the SOS Wire Chambers (cm).

A simplified diagram of the chamber design is shown in Fig. 4.29. These chambers are constructed using the “open plane” technique, in which individual wire and cathode (foil) planes are fabricated on a work bench, then stacked up on a rigid frame to make the chamber assembly. This method of construction is relatively simple and robust, lending itself nicely to fabrication in a modest workspace.

As a baseline, we plan to use commercially available readout electronics of the same design as presently in use in the SOS, the HMS, and other wire chambers at JLab. However, we note that there is the possibility of enhancing the particle identification power of the SHMS spectrometer if we measure the energy loss distribution of particles traversing the wire chambers. To do so would require modified electronics at the chamber and the addition of analog readout for groups of wires. A study of the feasibility and usefulness of performing a maximum likelihood analysis of these Landau distributed dE/dx samples is ongoing. Fig. 4.30 shows the results of a simulation of such a dE/dx system for identifying kaons and pions.

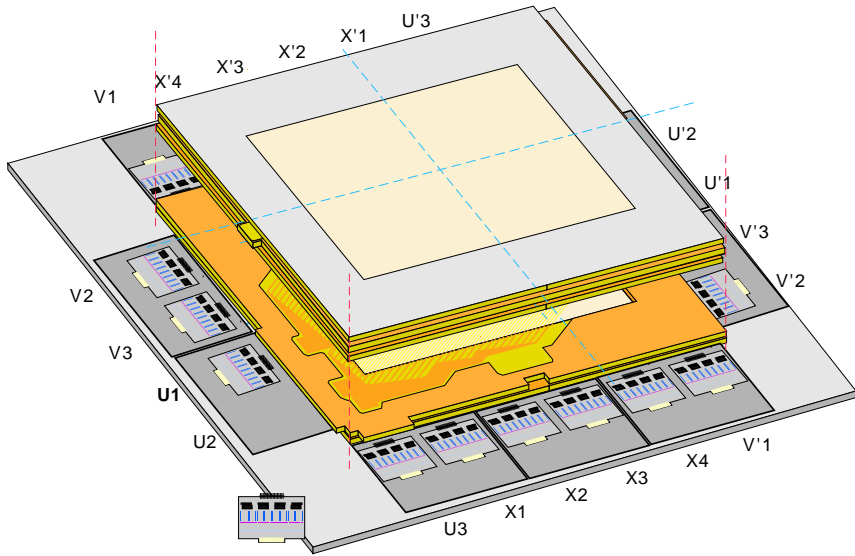


Figure 4.29: Block diagram of the SHMS Wire Chamber Assembly. The chamber is built by stacking individual wire and foil planes, each of which is fabricated separately using precision tooling.

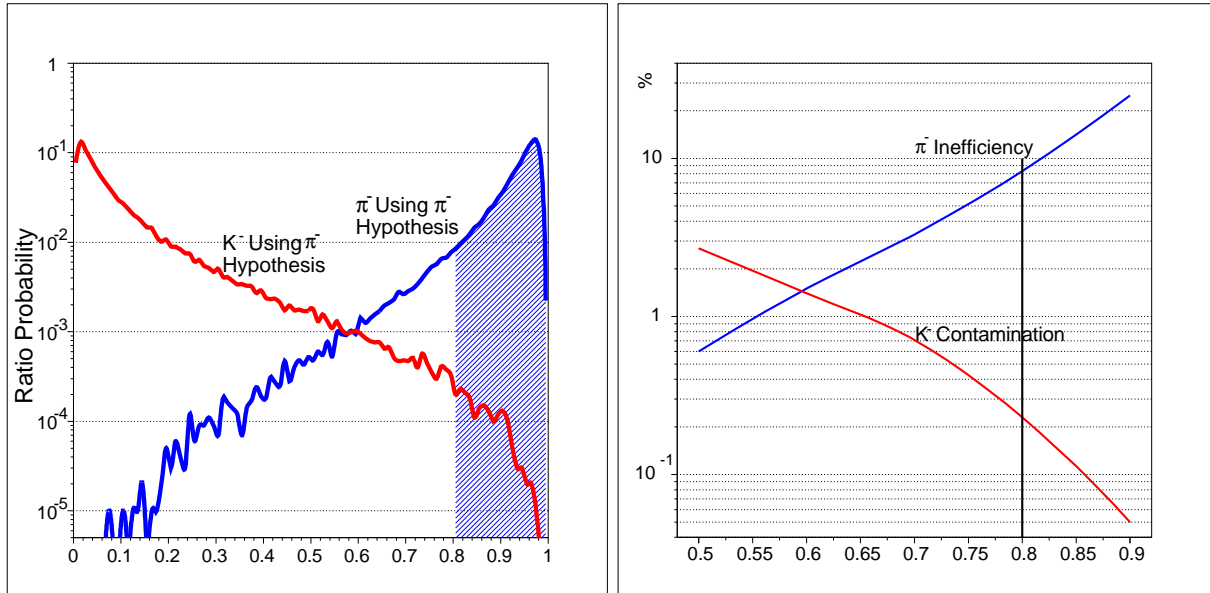


Figure 4.30: Pion/Kaon Discrimination using a Likelihood function applied to simulated energy loss distributions for 7-GeV/c particles in 12 wire chamber planes. For the (pion/kaon) hypothesis, only the eight (highest/lowest) measured energies are used. The left figure shows the distribution of pion likelihood ratios $R = \frac{L_\pi}{L_\pi + L_K}$ when the incident particle is a kaon or a pion. On the right is shown the pion inefficiency and the kaon contamination as a function of the choice of cut, when equal numbers of pions and kaons are passed through the system.

4.3.5.2 Quartz Čerenkov Hodoscope

The existing scintillating hodoscopes in Hall C are used for a surprising number of essential functions: to provide a trigger which is approximately 100% efficient for minimum ionizing particles¹, to reject accidental coincidences in multi-arm experiments, to help measure the efficiency of the tracking system, and to provide Particle Identification (PID) by time of flight (TOF).

While the first three functions listed above will still be critical for the SHMS, the PID function by TOF over the short $\simeq 2.2\text{-m}$ baseline inside the SHMS hut will be of little use at the higher average energies of the upgrade. Fig. 4.31 shows that, even over a 22.5-m distance from the target to the detector stack, particle identification by TOF is of limited use. Generally speaking, efficient, high-confidence PID will require extensive use of other technologies such as Čerenkov detectors, and that the time resolution requirement for the hodoscope system may therefore be relaxed. This means that the front hodoscope array can be made thinner (5mm versus the present 10mm in the HMS and SOS) which will help reduce the production of knock-on electrons which would otherwise deteriorate the performance of downstream Čerenkov detectors. Meanwhile, the rear hodoscope array can be made quite thick (10mm-25.4mm) since it will be the last element before the electromagnetic calorimeter.

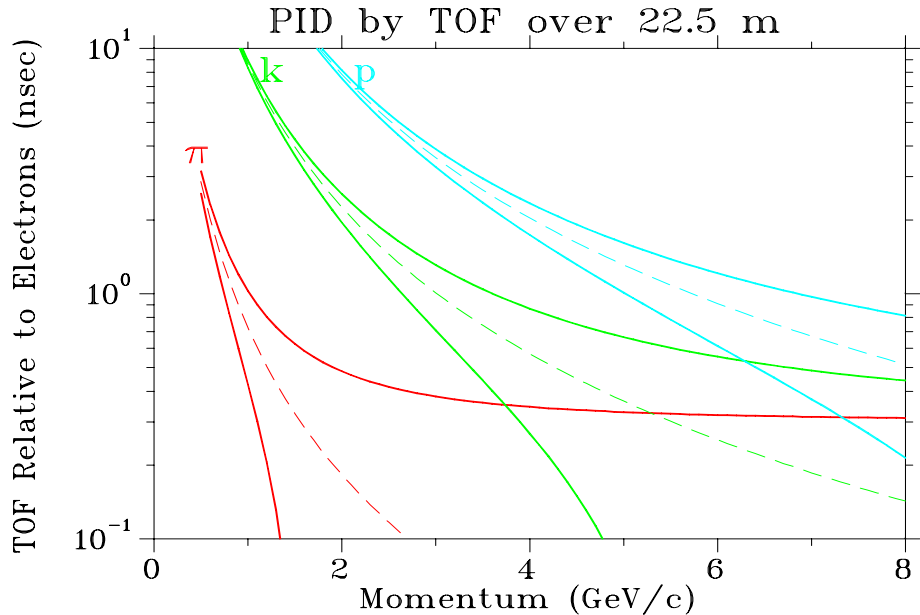


Figure 4.31: The dashed lines represent the time of flight (relative to electrons) versus momentum. The vase-shaped envelopes in solid lines demonstrate the limitations due to finite timing resolution ($\pm 1.5\sigma$ with $\sigma = 200 \text{ ps}$ assumed). At the points where the solid lines first intersect, the separation is only 3σ .

Taking into account the essential functions, and folding in our experience with the Hall C scintillating hodoscopes, we arrive at the following specifications for the SHMS hodoscopes:

¹For common detector materials, this corresponds to $\beta\gamma \simeq 3\text{-}4$, so a “realistic worst case scenario” is the detection of protons of momenta 3-4 GeV/c.

- Trigger: Because it is the heart of the SHMS trigger, the hodoscope must have $\geq 99.9\%$ trigger efficiency for minimum ionizing particles. To help ensure high efficiency, the pulse height variation across an element should be less than 10%. There must also be sufficient redundancy such that an $S_1 \cdot S_2$ coincidence is robust with respect to the inefficiency (or even loss) of a few channels. The detector should also be insensitive to background.
- Rejection of Accidentals: The mean-time resolution of the SHMS focal plane must be at least 100 ps (rms). This will easily permit a coincidence time resolution of 200 ps (rms) so that a $\pm 1\text{-ns}$ cut (single beam bucket) on coincidence time would remove only the tails of the good event distribution beyond 5σ .
- Wire Chamber Tracking Efficiency: The segmentation of the hodoscope X and Y elements has to be sufficiently fine to define a beam of particles which pass through the active region of the wire chambers.
- The hodoscope should have minimal adverse impact on downstream detectors.
- The hodoscope should have a 10-year lifetime before major overhaul.

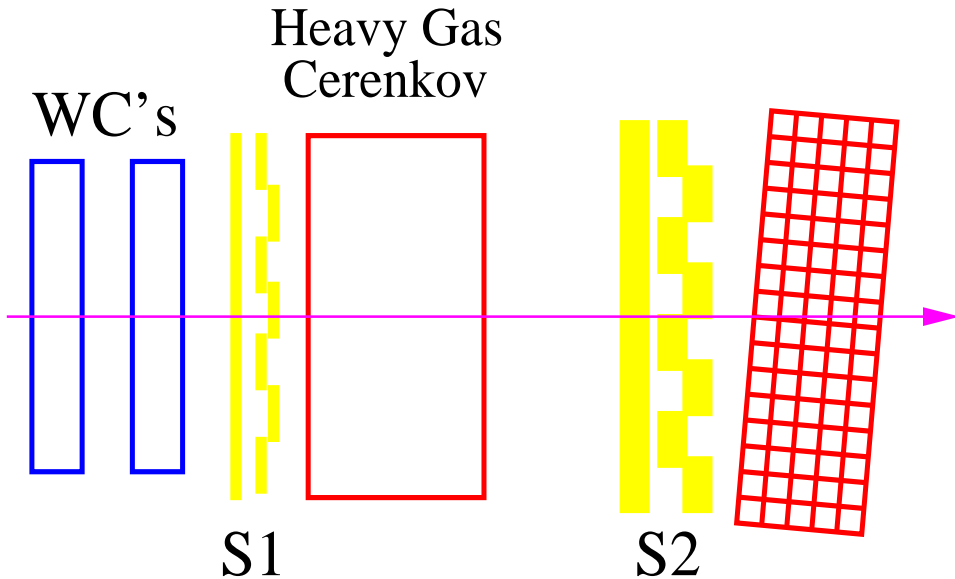


Figure 4.32: The thin S1 X and Y arrays will be located immediately after the wire chambers. The thicker S2 arrays will be located just before the electromagnetic calorimeter. (Drawing not to scale.)

The solution which meets nearly all of the above specifications is two pairs of X-Y hodoscopes (Figure 4.32), named S_1 and S_2 , similar to those currently installed in the HMS and SOS. The two arrays would be separated by roughly 2 m, with S_1 following the Wire Chambers and S_2 just before the Calorimeter. The new features which we would like to emphasize are that

Element	Material	Width	Length
S1X	5 mm BC408	11.3 cm	110 cm
S1Y	5 mm BC408	14 cm	90 cm
S2X	2.5 cm Quartz ³	14 cm	140 cm
S2Y	2.5 cm Quartz	18 cm	110 cm

Table 4.7: Nominal dimensions for the hodoscope elements of each of the four arrays. There are eight elements per plane.

- i. S1 will be made of “thin” (e.g. 5mm), scintillator elements with long attenuation length BC408,
- ii. S2 will consist of a relatively “thick” (e.g. 2cm-3cm) quartz Čerenkov radiator elements, and
- iii. standard 12-stage PMTs like the XP2262B will be employed, operated at low anode currents for extended lifetime.

Since the existing Hall C hodoscopes are made of scintillator, the most dramatic change listed above would be the use of a quartz Čerenkov for the S2 arrays. Simulations by Simicevic[35] for the $Q_{weak}(proton)$ experiment indicate that it is reasonable to expect several hundred photoelectrons (p.e.) for a 1-meter length quartz radiator with a moderately good surface reflectivity. *A quartz Čerenkov detector operated at a threshold of 100 p.e. could be essentially 100% efficient and blind to low energy backgrounds, resulting in a much cleaner $S_1 \cdot S_2$ trigger.* This capability is critical for the clean detection (and accurate tracking efficiency determination) of protons in extremely low cross-section measurements² at a CW facility.

Each of the four arrays will have eight rectangular bars of scintillator or Čerenkov radiator. The active area of the arrays is designed to have $\simeq 100\%$ acceptance of the beam envelope for the full momentum bite and target acceptance of the large solid angle tune. The SHMS beam envelope simulations can be found in Section 4.3.4. A summary of the nominal hodoscope dimensions is given in Table 4.7. Finally, with one PMT on each end of a scintillator or Čerenkov radiator paddle, the total number of SHMS hodoscope channels will be 64.

4.3.5.3 Particle Identification

Overview

Hadron identification for momenta up to 11 GeV/c will be fundamentally different from that of the HMS-SOS detector systems. With increasing momentum it becomes more and more difficult to distinguish hadrons by time of flight measurements. With the 2.2-m flight path in the detector hut, kaon-pion separation by time of flight becomes infeasible at roughly 2 GeV/c. At 3.5 GeV/c also proton-kaon separation will no longer work. Coincidence timing with a hadron flight path in the SHMS of 22.5 m and a reconstructed coincidence time resolution of roughly 200 ps extends this to 4 GeV and 7 GeV, respectively. Note however,

²e.g., $d(\gamma, p)n$ at high s and $A(e, e'p)A - 1$ at high Q^2 .

that particle identification by means of coincidence timing will in general not distinguish particles from accidental coincidences and therefore will lead to an irreducible background that must be subtracted. Therefore, at high momenta one must rely on other means of particle identification, e.g. Čerenkov detectors, dE/dx measurements, and Transition Radiation Detectors (TRD).

As described in detail below, the Super High Momentum Spectrometer will draw upon a variety of techniques to achieve particle identification over its entire momentum range. A global outline of the scheme is shown graphically in Fig. 4.33, where the discrimination power is shown as the significance of the measurements (number of standard deviations) in the various PID detectors versus the particle momentum.

Electron identification can always be accomplished by use of energy measurements in the electromagnetic calorimeter, and optionally improved upon with a TRD. Over the SHMS momentum range, electrons will always radiate in Čerenkov counters, so these devices will also contribute to electron tagging. For extreme cases at high momentum and low signal to background, such as measurements at $x > 1$, we envision adding another Čerenkov counter in place of the last section of vacuum pipe just upstream of the first wire chamber. This device, using a Ne-Ar mixture at atmospheric pressure, can have its index of refraction tuned to enhance either electron-pion or pion-kaon discrimination at high momentum.

For hadron identification the following PID strategy can be employed:

~1 to ~3 GeV/c: Kaon-pion separation can be achieved with the appropriate choice of one aerogel Čerenkov. A time of flight path of 2.2 m with a TOF resolution of 200 ps still allows one to distinguish protons from kaons at the 3σ level up to 2 GeV/c. At the high end of this range, proton PID can be improved with the use of an additional aerogel counter with $n=1.02$.

~3 to ~5.5 GeV/c: Pions will trigger a C_4F_{10} gas Čerenkov. The C_4F_{10} pressure will be adjusted such that kaons do not radiate. Kaons will trigger an $n = 1.015$ aerogel Čerenkov.

~5.5 to 11 GeV/c: Pions will still trigger the C_4F_{10} gas Čerenkov. An atmospheric pressure gas Čerenkov counter will be inserted upstream of the first wire chamber and filled with an Ar-Ne mixture to provide a pion tag or an additional electron tag. At these higher momenta the multiple scattering in this added detector will be tolerable.

Thus, an appropriate choice of combinations of detectors and techniques will allow the SHMS to provide useful particle identification over its entire momentum range. The remainder of this section will describe each of these detectors.

Shower Counter

The SHMS magnetic spectrometer is aimed to cover small forward angles and higher momentum settings not available so far in Hall C[36]. When identifying electrons at these settings, good particle identification is needed to suppress high hadron background. Lead glass electromagnetic calorimeters are well suited to this purpose.

The design of the SHMS electromagnetic calorimeter is similar to the existing HMS and SOS calorimeters in many respects. The HMS calorimeter consists of $10 \times 10 \times 70 \text{ cm}^3$

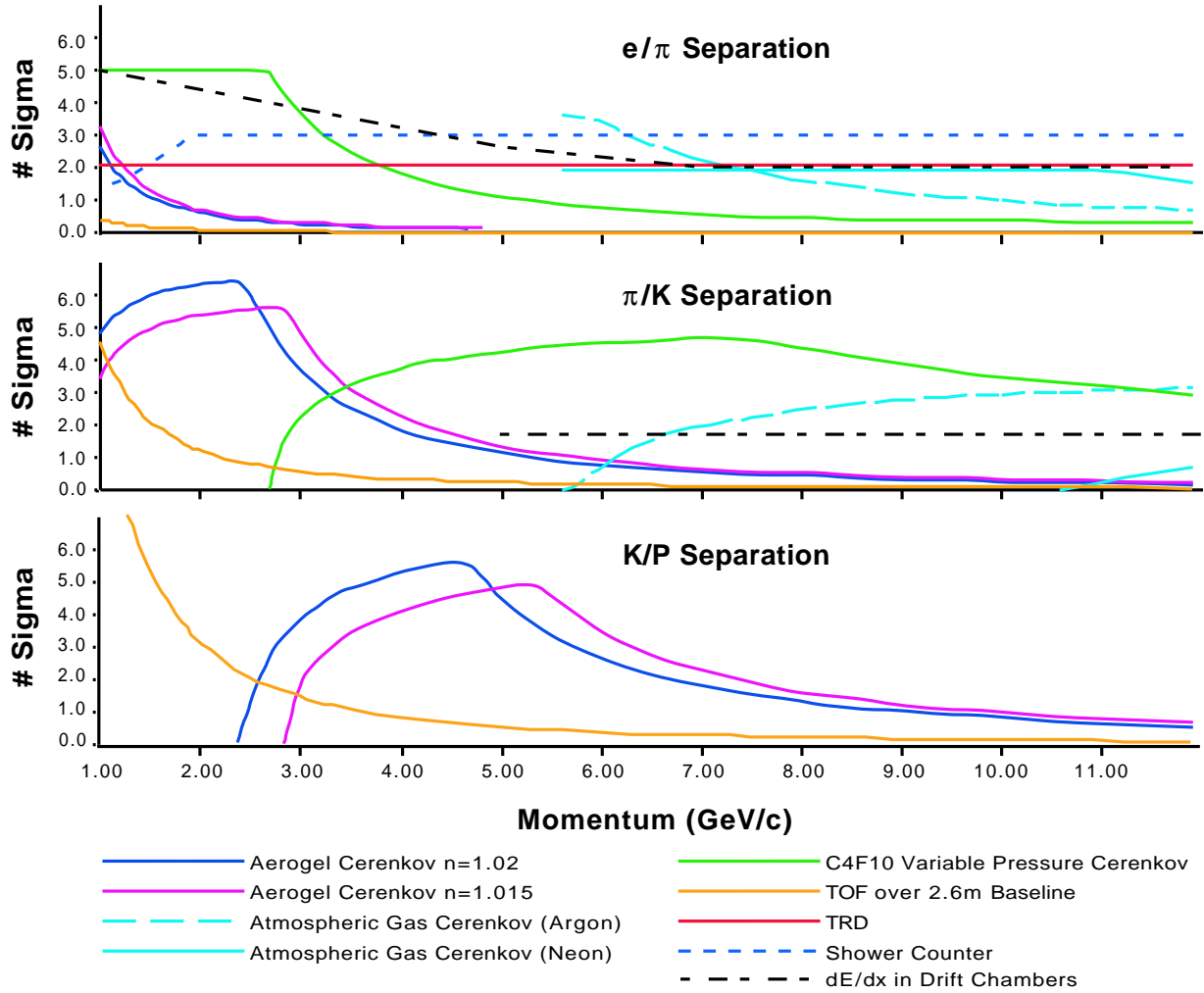


Figure 4.33: Particle Identification Resolving Power over the SHMS Momentum Range. The vertical scale in each graph is number of standard deviations which separate the two particle types shown, calculated for all of the relevant detectors in the system.

TF-1 Lead Glass rectangular blocks wrapped in thin aluminized mylar and in teflon film for optical tightness. The characteristics of the TF-1 lead glass are: density $\rho = 3.86 \text{ g/cm}^3$, refractive index $n=1.65$, radiation length $R_L = 2.74 \text{ cm}$. The blocks are arranged in four layers for a total thickness of 40 cm (14.6 radiation lengths). Photomultiplier tubes (Philips XP34462B) are mounted at both ends of each block in the first two layers and at one end for the remaining layers. The modules are equipped with ST-type fiber adapters for the gain monitoring system.

Figure 4.34 shows the results of a Monte Carlo simulation for the lead glass calorimeter. As can be seen from the left panel, the calorimeter is linear within 3.5% up to electron energies of 12 GeV. The energy resolution of the HMS calorimeter (PMTs mounted on one

end of each block) measured in the energy range 0.5–4.0 GeV is given by

$$\frac{\Delta E}{E}(\%) = \frac{6.1}{\sqrt{E(GeV)}} + 0.3 \quad (4.3)$$

and is comparable to the resolution of similar devices[37]. The SOS calorimeter is somewhat better in this respect[38]. More details on the HMS and SOS calorimeter construction and performance can be found in Ref. [38]. The performance of the calorimeters has not deteriorated significantly in the 7 years since they were first installed.

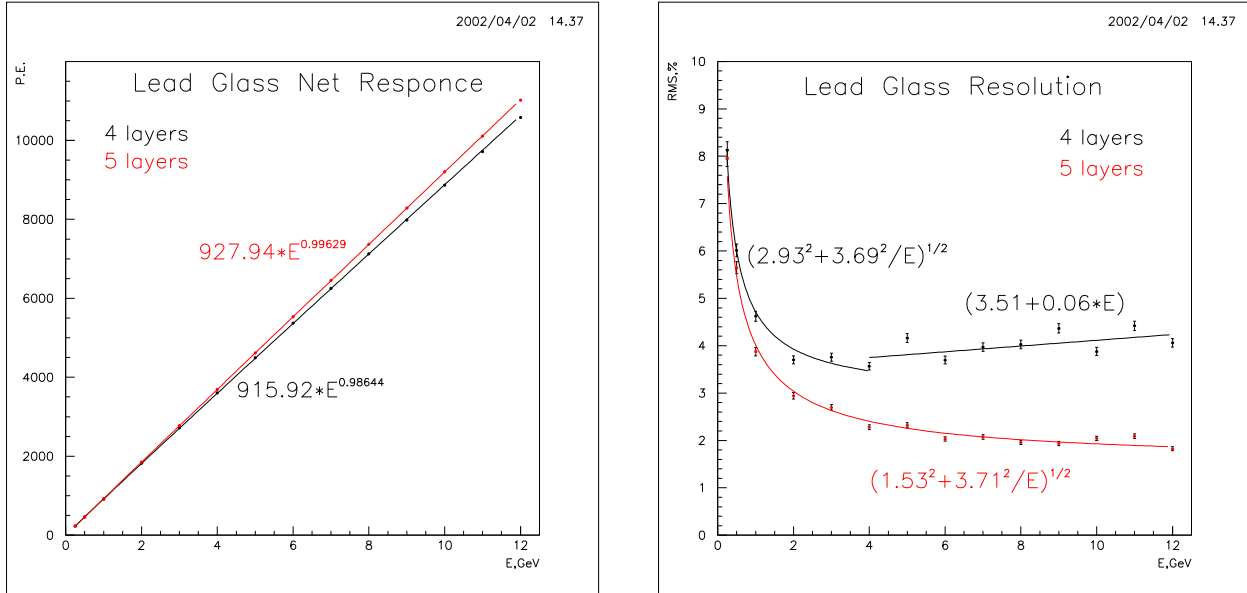


Figure 4.34: EGS4 Monte Carlo simulation of the linearity (left panel) and resolution (right panel) of a TF-1 Lead Glass modular calorimeter. The calibration, coordinate correction and electronic effects are not included.

The observed π^-/e^- rejection factor of the HMS calorimeter is better than $(1 - 5) \times 10^{-2}$ in the momentum range 0.5 to 2.0 GeV/c, with electron detection efficiency $\geq 99\%$. At these low momenta, pion rejection can be improved at the cost of electron efficiency by using a tighter cut on the calorimeter energy. At higher momenta, the pion rejection is not significantly improved by a tighter cut.

The energy dependence of the resolution of the calorimeters indicates almost complete absorption of electromagnetic showers up to energies of ~ 4 GeV. However, at higher energies the Monte Carlo simulation predicts a slow rise of the resolution, which is a clear indication of leakage (see Fig. 4.34, right panel). Adding an additional layer restores full absorption, hence improving both the resolution and linearity. Adding a fifth layer also improves the electron detection efficiency (see Fig. 4.35, top panel), but it does not change the pion rejection (Fig. 4.35, bottom panel). Exploiting the transverse and longitudinal spread of the deposited energy will improve pion rejection, and the contribution of a fifth layer may be valuable in this case.

Two side by side stacks of 12 blocks are needed to cover the whole acceptance of the spectrometer (see Figs. 4.23, 4.24) and thus 120 modules would be required. As adjacent

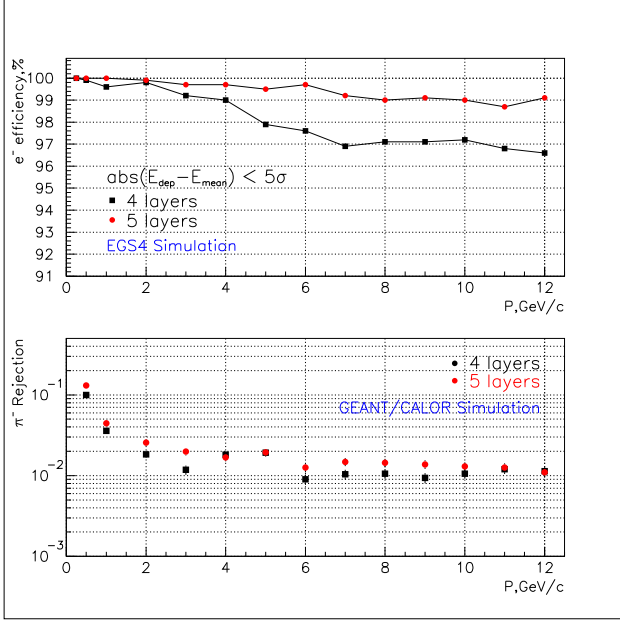


Figure 4.35: Electron detection efficiency (top panel) and pion rejection (bottom panel) obtained from the Monte Carlo simulation of the TF-1 Lead Glass Calorimeter. The calibration, coordinate correction and electronic effects are not included.

blocks will be optically decoupled, the light will be collected with PMTs on both sides of the calorimeter. The calorimeter will be deflected by small amounts in both vertical and horizontal directions to avoid cracks in between the modules.

Alternatively one can construct a lower cost, 4-layer calorimeter using only 96 modules. It will still contain most of the electromagnetic shower and hence have hadron/electron rejection capability. The leakage of energy will not significantly affect the hadron rejection, but will hurt the electron efficiency (or the electron rejection when measuring pions).

Another low cost alternative is an assembly of 132 short modules oriented along the beam direction. A preshower wall of 24 long modules before this assembly may be helpful for the separation of minimum ionizing hadrons from just developed electromagnetic showers. The deepness of the calorimeter should be optimized to get good rejection across the SHMS momentum range.

Atmospheric Pressure Čerenkov

One of the typical uses of the SHMS will be to detect highly inelastic scattered electrons. At such kinematics the pion background can be significant, so a reliable method of electron identification is required. Threshold Čerenkov detectors are excellent tools to use when the particle velocity β is greater than phase velocity of light in the medium c/n . The minimum momentum at which a particle will exceed the phase velocity of light in the medium is given by:

$$P_{\min} \cdot c = \frac{M \cdot c^2}{\sqrt{n^2 - 1}} \quad (4.4)$$

Thus, if we require 10-GeV/c pion to be under threshold, then $n - 1$ must be 0.0001 or

smaller, which can be achieved either by choosing low pressure gases, or certain noble gases at STP. For example $n - 1 = 0.000067$ for Ne, $n - 1 = 0.000033$ for He.

The main characteristic of threshold Čerenkov detectors is the number of detected photons. For very low refractive index gases the number of emitted photons is extremely small. At $p > 9.0$ GeV/c a gas Čerenkov for electron-pion discrimination should be over 2.5-3 m long in order to have an adequate number of photoelectrons. A $\beta=1$ particle traversing a 3 m long Ne radiator will produce about 30 photons in the visible light range (300-700nm). Most PMTs are not very sensitive below 300 nm. Since the production has a λ^{-2} dependence, and $n(\lambda)$ goes to unity at short wavelengths, the Čerenkov light produced will be peaked in the ultraviolet (100-300nm). Using these photons will double the number of photoelectrons from the photocathode [38, 40]. PMT windows coated with p-terphenyl, which absorbs UV light and retransmits it in the range of 390 nm, increase the PMT response by about 90% compared to the uncoated tubes[40]. The expected number of photoelectrons will be $\simeq 10 - 12$.

If the pion momentum is slightly higher than threshold, the number of photons produced by pions may still be much smaller than the number of photons produced by electrons. Fig. 4.36 shows that the Čerenkov light production reaches 20% of the maximum with particle momenta about 1.1 times the threshold momentum. We propose to use a Ne+Ar gas mixture to tune the Čerenkov radiator refractive index and increase the number of photons by about 20%.

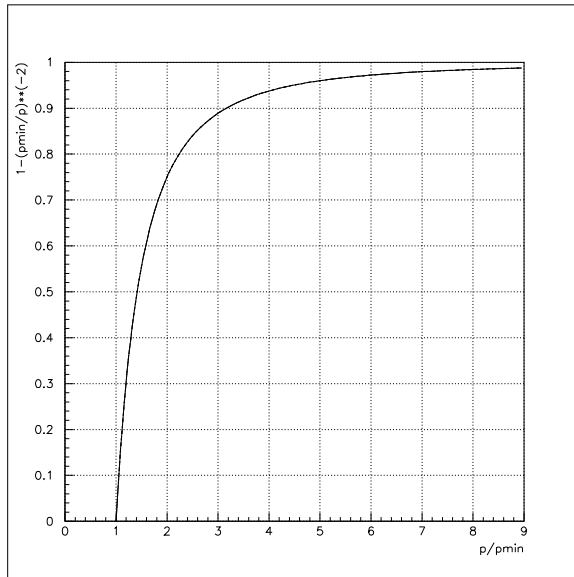


Figure 4.36: The Momentum Dependence of the Čerenkov Light Production Rate (eq.6)

The solution to adjust the refractive index by using the noble gases at STP appears more attractive than the use of a low pressure tank. The low pressure approach requires a 3 m long vacuum sealed volume. Having this volume under-pressure tends to gradually take in O₂ and H₂O which can change not only the threshold condition, but also absorb the ultraviolet part of the Čerenkov radiation.

Using Ne gas at STP has another essential advantage. In this case, entrance and outgoing windows of the Čerenkov tank can be made very thin (maybe from teflon). This will aid in minimizing multiple scattering in front of focal plane (drift chambers).

The atmospheric Čerenkov tank we propose would replace the final 3 m of the vacuum pipe as it enters the SHMS detector hut. The diameter needs to be only about 60 cm at the upstream end, and cover $75 \times 100 \text{ cm}^2$ at the downstream end. A vacuum window with the same scattering properties as the standard one would be installed upstream of the Čerenkov counter. The Čerenkov windows and mirrors and their supports will be made lightweight so as to keep multiple scattering at a minimum. Even then, the detector would only be compatible at the high end of the SHMS momentum range.

Heavy Gas Čerenkov

Above $\sim 3 \text{ GeV}/c$, hadron species cannot be reliably distinguished by time of flight over the 2.2-m baseline planned for the SHMS detector stack, and so information from Čerenkov detectors becomes increasingly relevant. An aerogel Čerenkov detector with $n = 1.02$ will provide π^\pm/K^\pm discrimination only up to $2.4 \text{ GeV}/c$. Beyond this momentum, a gaseous Čerenkov detector is required. Based on the excellent operational experience at JLab and elsewhere, we propose to construct a threshold Čerenkov using the heavy perfluorocarbon (PFC) gas C_4F_{10} as a radiator. This gas has an index of refraction of 1.00143 at standard temperature and pressure, and so can be used here over a wide range of incident particle momenta.

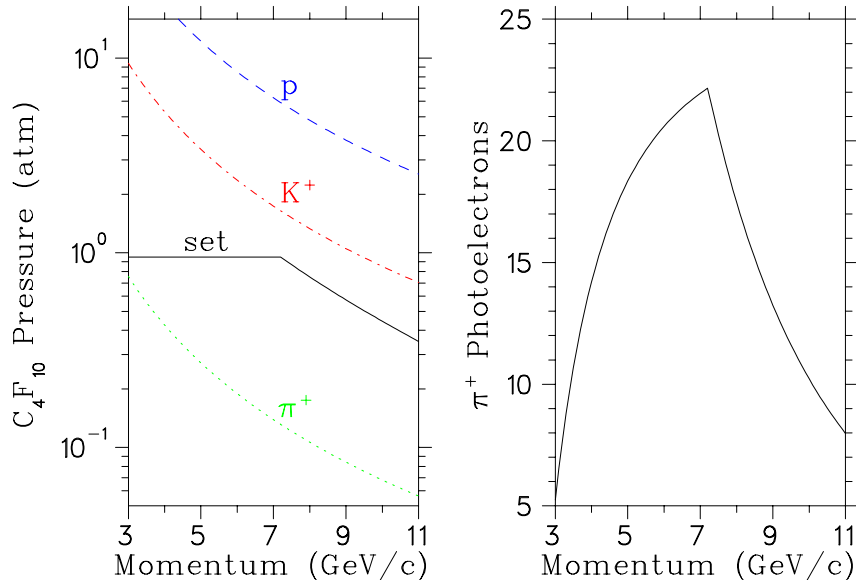


Figure 4.37: Left: Threshold C_4F_{10} pressure required for Čerenkov light generation from the particles indicated. The solid curve indicates the operating pressure planned for the detector. Right: Number of photoelectrons anticipated for the detector, taking into account the transmittance, reflectivity, and quantum efficiency functions of the detector components.

The solid curve in the left panel of Fig. 4.37 indicates the gas pressure we propose to use

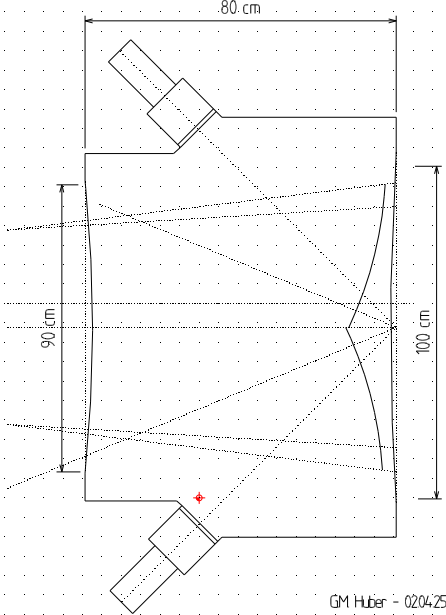


Figure 4.38: Schematic Design for the SHMS Heavy Gas Čerenkov Detector.

at each SHMS central momentum setting. It is expected that the detector gas pressure will be remotely controlled from the counting room as the spectrometer momentum is changed. We assume 0.95 atm. pressure from 3.4 GeV/c to 7.0 GeV/c, and sub-atmospheric pressure at higher momenta. The gap between the ‘set’ and ‘ K^+ ’ curves above 7 GeV/c takes into account the +25%/-15% momentum bite of the SHMS, and a possible 0.1-atm error in the setting of the gas pressure regulator. We do not anticipate the detector being used for π^+/K^+ separation at momenta below 3.4 GeV/c.

Figure 4.38 shows a schematic design for the heavy gas Čerenkov. The enclosure is a cylinder of nonmagnetic stainless steel, with the PMTs located outside, viewing through a 1-cm thick UV-grade fused silica window. This allows for better isolation of the pressurized cavity, and allows one to maintain proper PMT-mirror optical alignment should the PMT require servicing. Four mirrors and photomultipliers are required to cover the SHMS beam envelope; they should be of the highest possible quality. As a reference design, we have selected the Photonis[41] XP4508B 5” photomultiplier tube. This is similar to the PMT currently used in Hall B, except that it has a flat face of fused silica, which allows for flush mating with the quartz window. A custom-design voltage divider with boosted voltage between the photocathode and the first dynode will be used to provide optimum focusing of the photoelectrons, and so minimize losses within the dynode chain. To minimize aberrations, the mirrors should be thin glass, which can be structurally reinforced outside of the beam envelope. Protected aluminum mirror coatings with > 90% reflectivity down to 200 nm are commercially available[42]. We propose to use 0.020” titanium for the particle entrance and exit windows, which is the same material used on the G0 spectrometer [43].

C_4F_{10} is very expensive, and so a recovery system is required. C_4F_{10} has excellent UV transmission characteristics (97%@170 nm) provided it is kept pure. A filter and cold trap

may be desirable additions to the gas recovery system, to maintain the required gas purity. Both oxygen and water absorb strongly below 200 nm, and should be kept below 0.1%. Residual nitrogen has an effect on the refractive index, and should be kept constant and below < 1%.

The right panel of Fig. 4.37 indicates the number of detected photoelectrons expected from a π^+ for a 70-cm radiator length. The C_4F_{10} transmission, mirror reflectivity, quartz transmittance, and PMT spectral characteristics, as well as possible optical misalignment, were all taken into account. The resulting π^+ detection inefficiency, assuming that an off-line cut is placed at < 1.5 photoelectrons to eliminate knock-on events, is less than 0.1% for all momenta between 3.4 and 10.3 GeV/c, and rises to a modest 0.3% at 11.0 GeV/c.

In conclusion, a heavy gas Čerenkov detector, utilizing a C_4F_{10} radiator with variable pressure between 0.4 and 0.95 atm., appears to be a practical way to obtain reliable π^+ / K^+ separation within the SHMS.

Transition Radiation Detector

The purpose of the transition radiation detector (TRD) is to separate electrons from pions. This is possible because ultra relativistic charged particles emit *transition radiation* (TR) in the form of x-rays when they traverse a dielectric boundary[44]. TRDs are composed of multiple modules stacked together where a single module contains a radiator and x-ray detector (i.e. multiwire proportional chamber). Each radiator is made up of many dielectric interfaces of low Z material to increase the TR yield. TRDs typically have a threshold of $\gamma = 1000$, hence only electrons will produce TR photons in the momentum range of the SHMS. In general, particle identification is accomplished either by examining the total energy deposited in the detector or by cutting on the number of high energy clusters (typically above 5–7 keV) deposited along the track. It has been shown that there is improvement in the particle separation if cluster counting is performed[45, 46]. This is because the number of clusters obeys a Poisson distribution while the total energy has a long Landau distributed tail. The pion rejection factor (PRF), which is inversely related to the pion efficiency, is largely dependent upon the the length of the detector, as shown in Figure 4.39 with smaller effects coming from the type of radiator, chamber, electronics and particle identification method[37].

The detector will be located between the heavy gas Čerenkov and the back hodoscope planes and will be about 60 cm long. To maximize the PRF, uniformly spaced foils of polyethylene would be close to ideal (lithium foils being ideal), but due to the relatively large active area of the detector ($110 \times 140 \text{ cm}^2$), carbon fibers or polyethylene foam will be considered. Using a fiber or foam radiator decreases the PRF by a factor of about 2 when compared to foils. The radiator will be 50 mm thick with a mean foil thickness of about 17 μm and a mean gap or pore size of about 200 μm . This corresponds on average to 230 foils per radiator which will produce about one detected TR x-ray per module. The x-ray detector will be a xenon filled longitudinal drift proportional chamber to facilitate cluster counting. Since xenon gas is expensive, the chamber gas will be recirculated and filtered. Figure 4.40 shows a sketch of a single TRD module and the pulse distribution. The longitudinal drift will be 20 mm and, if a 90% Xe/10% CO_2 gas mixture is used (drift velocity $\sim 25 \text{ mm}/\mu\text{s}$ for $E = 3 \text{ kV/cm}$), the maximum drift times will be about 0.80 μs . The proportional region

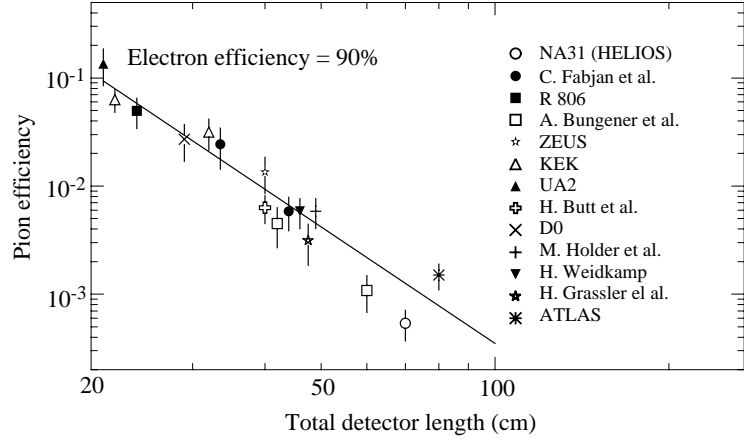


Figure 4.39: Pion Efficiency Measured (or Predicted) for different TRDs as a function of the detector length for an electron efficiency of 90%. (Figure from Ref. [37])

will be $8 \times 5 \text{ mm}^2$ (anode wires spaced by 5 mm). Monte Carlo simulations which include hadronic showers and δ -ray production will be needed to determine if this segmentation is sufficient. Special attention must be paid to the exit cathode plane to reduce bulging due to pressure changes and the “hydrostatic” pressure inside the chamber. The electronics on each anode wire will consist of a preamplifier, a shaping amplifier and an 8-bit flash ADC.

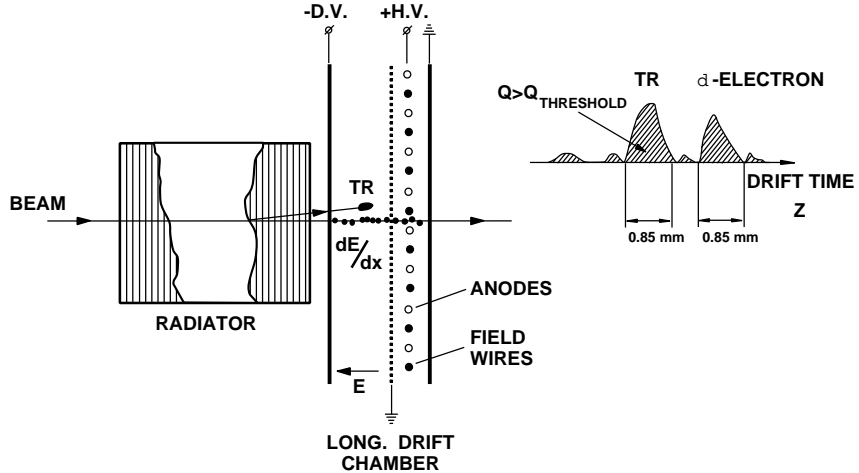


Figure 4.40: Single module with time expansion chamber (TEC) which includes a drift region and a proportional region. The output signals will consist of uniform dE/dx ionization with localized TR clusters and δ -ray clusters.

At least six modules will be used for the TRD with a total length of about 60 cm. At 90% electron efficiency, this will result in a PRF of about 200 - 300. At 95% electron efficiency, the PRF will reduce by a factor of 3 or 4, but if a higher rejection factor is needed, additional

modules could be used and/or a foil radiator could be used. Off-line analysis which includes more sophisticated statistical methods (i.e. likelihood) and an intelligent cluster threshold will also improve the PRF. This intelligent threshold will vary the threshold with drift time, thus taking advantage of the energy dependence of the photon's range in the chamber. Since the TR yield tends to saturate at $\gamma \sim 8000$, the PRF will be flat over the SHMS momentum range. The combination of the TRD, shower counter and a Čerenkov will be more than adequate to suppress any hadronic background encountered in the SHMS. Additionally, having three particle identification detectors will provide a better mechanism for systematic studies of the detector efficiencies.

Aerogel Čerenkov Counter

The aerogel detectors will be standard diffusion box type detectors consisting of a layer of silica aerogel in a diffuse reflective box, read out at the sides by large 5-inch PMTs. For the SHMS, a detector with a minimum active area of $110 \times 140 \text{ cm}^2$ is needed for full coverage of the beam envelope at the anticipated detector location, 2.3 m downstream from the focal plane (see Figs. 4.24, 4.23 and Ref. [36]). Thus, a detector could be 110 cm in x (bending or vertical) with 5 PMTs on each side and 140 cm in y (horizontal). Allowing for an up to 10 cm thick aerogel layer the entire box will be roughly 30 cm deep (in z direction).

The technology of aerogel detectors with a diffusion box and PMTs as light collectors is well established at Jefferson Lab. The Hall C detector with $n = 1.034$ yielded 19.3 photoelectrons for $\beta = 1$ particles [47]. The two Hall A detectors, A1 with $n = 1.015$ (9 cm) and A2 with $n = 1.055$ (5 cm), yielded 8 and 30 photoelectrons, respectively [48]. The significantly better performance of A2 is certainly due in part to the higher index of refraction. Additionally, it is believed to benefit from a higher photoelectron yield of the Photonis tubes used in this detector as opposed to the Burle tubes used in the A1.

Two more detectors are currently under design, one for the HMS and another for the hypernuclear spectrometer (HKS). The HKS detector explores the possibility of segmenting the detector along the focal plane and thus increasing the rate capability. This should also be considered for the SHMS detector, i.e. to ensure reliable performance at the very forward angle settings possible with this spectrometer. The design with 5 PMTs on each side would allow for 5 optically separated segments. Limiting individual segment rates to 1 MHz would result in a total rate capability of 5 MHz for particles above the Čerenkov threshold. To compensate for the dead areas introduced by segmentation, a second plane with the segments offset by half a segment width would be required.

As aerogel the materials SP15, SP30 and SP50 from Matsushita Electric Works is recommended. Matsushita's aerogel has a waterproof coating that makes it hydrophobic. This removes the need for baking (in fact baking will destroy the coating) and also increases transparency. A low cost 5-inch PMT (Photonis XP4572) has been successfully employed in the Hall A A2 detector and should also be considered for the detector proposed here. Fig. 4.41 shows the thresholds for these materials as a function of momentum.

The performance of the detector has been simulated with D. Higinbotham's Monte Carlo code [49]. With the standard parameters and $n = 1.015$ one gets 6 photoelectrons. This results in a detection efficiency of $> 99\%$ for a 1 p.e. cut and 88% for left-right coincidence of ≥ 1 p.e. The experience with the Hall A A2 and the HKS prototype suggest that this

simulation is a lower estimate. Therefore, it is expected that we will actually see closer to 10 photoelectrons and achieve a left-right coincidence efficiency close to 98%.

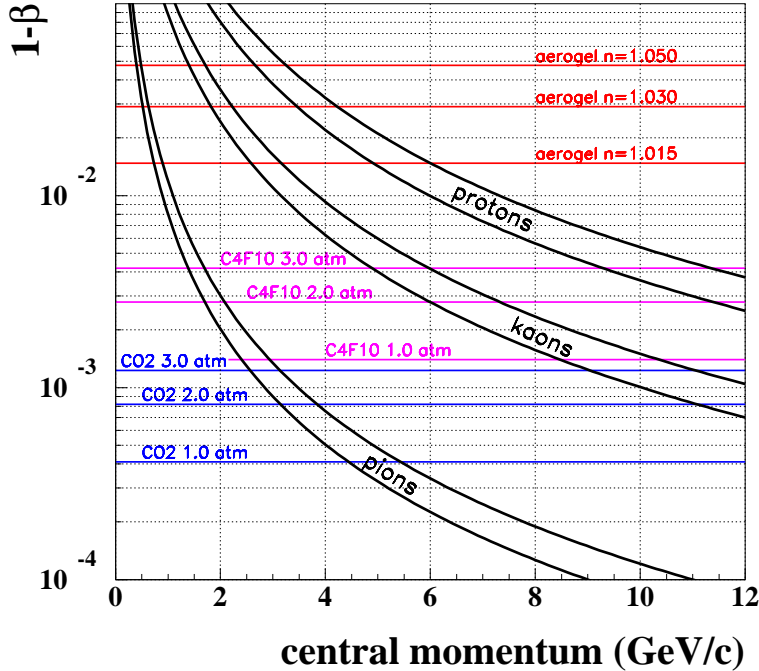


Figure 4.41: Hadron Velocity $1 - \beta$ as a Function of Momentum. For each particle a band is shown corresponding to a momentum acceptance of $\pm 10\%$. The horizontal lines show thresholds for different Čerenkov radiators.

4.3.5.4 Focal Plane Polarimeter

To measure the ratio of proton electric to magnetic form factor at $Q^2 > 12 \text{ GeV}^2$ using the recoil polarization technique, the focal plane polarimeter (FPP) which is being built for the HMS will have to be moved to the SHMS. The FPP is in effect two polarimeters in series, so there is a CH_2 analyzer followed by drift chambers and then an additional CH_2 analyzer followed by drift chambers. A drawing of where the FPP would fit into the SHMS detector package is shown in Fig. 4.42. The 2nd Čerenkov and aerogel/TRD would have to be removed.

4.3.5.5 Trigger, Data Acquisition, and Online Computing

Trigger

The focal plane trigger electronics used for the HMS and SOS has been designed to be flexible, fast and efficient at detecting particles. These triggers consist of requiring hits in a majority of the hodoscope planes combined with options to require or veto on signals from the various particle ID capable detectors in the focal plane hut. The SHMS trigger

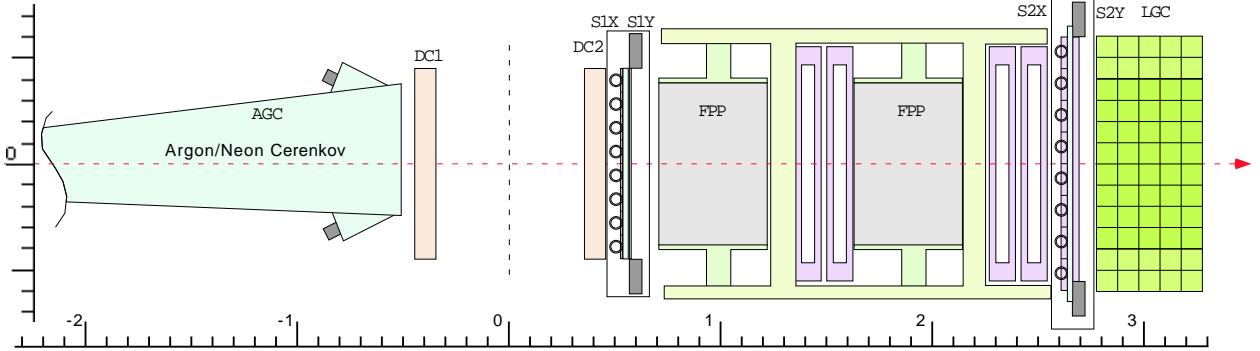


Figure 4.42: A Schematic of where the Focal Plane Polarimeter could fit into the SHMS Detector Package. There are two CH_2 analyzers, each followed by a set of drift chambers.

electronics will be similar to the HMS and SOS logic but there will be opportunities for increased sophistication in the trigger.

The design of the HMS and SOS triggers was in part driven by the desire to minimize the time to form the trigger, thus minimizing the amount of delay required for the TDC and ADC inputs from each PMT. With the use of common stop TDCs and ADCs such as those described below, triggers will not need to be formed as quickly. This will allow for the possibility of more sophisticated triggers and the use of computer controllable logic modules.

DAQ Electronics

The fine resolution (0.5 ns) TDCs used for the Hall C drift chambers are multihit common-stop models that do not require long cables to delay the signals until a trigger arrives. The absence of delay cables greatly simplifies the physical layout of the experimental apparatus and electronics. Furthermore, the commissioning of experiments and new experimental conditions is simplified. Such common-stop devices have not been available at the higher resolutions required for PMT based detectors, and no similar devices have been affordable for charge digitization. For PMT digitizers the inputs must be delayed by approximately 400 ns to wait for the formation of focal plane triggers and a coincidence between spectrometers. Recent advances, however, make it clear that multihit, buffered, common stop TDCs and ADCs of sufficient resolution will be available for the SHMS.

The JLab Physics Electronics Group is developing a 64/32 channel TDC based on the F1 chip [50]. When used in the 32 channel mode this TDC will have a least count of 60ps, yielding sufficient time resolution for any PMT based detector. The effort to develop this TDC is already well advanced and it is expected that the VME module being developed will be used by some experiments at JLab within the next few years. The per-channel cost of this TDC is expected to be comparable to that of common-start high resolution TDCs used now.

Standard ADCs operate by integrating the current on an input while a gate is present. Since this gate is generated by a trigger which can take many hundreds of nanoseconds to form, each ADC input must be delayed with long coaxial cables. The use of analog delay can be avoided by using a Flash ADC to continuously digitize the input and saving the data in

memory while waiting for the gate. When the gate arrives, the appropriate samples can be summed to produce a digital integration of the input. While this technique has been used, it is not in common use for situations with PMT pulses only a few tens of nanoseconds in width.

While affordable commercial Flash ADC modules are not available, indications are that either affordable modules will be available before the upgrade or that building suitable modules at JLab will be feasible. Flash ADC modules suitable for particle physics use, such as the Struck SIS3300, are available now. This 8 channel module which digitizes at 100MHz with a 12 bit Flash ADC would work well with detectors with wide PMT pulse shapes. However, the cost per channel is several times that of conventional ADCs, so the module would only be appropriate for prototyping and specialized applications.

As part of R&D efforts for the Hall D GlueX experiment, a single channel ADC prototype that uses a 250MHz 8bit Flash ADC chip has been designed. The key components of this design are inexpensive, so overall costs should be comparable to those of conventional ADC modules. Even though the 8 bit resolution is less than the 10 to 14 bits typically used in nuclear physics spectrometers, some resolution is recovered by the fact that a PMT pulse a few tens of nanoseconds wide will be sampled several times yielding better precision. An ADC based on this existing design is already good enough for the majority of the charge digitization required for the SHMS, but we note that higher resolution flash ADCs may be affordable at the time of the upgrade. The JLab electronics group is currently exploring development of a general purpose ADC module based on the GlueX flash ADC prototype.

A side-benefit of flash ADCs is that not only do they record pulse shape, but also pulse timing. Although it is unlikely that a flash ADC can obtain time resolutions as good as the 60ps of the F1TDC, sub nanosecond timing is feasible. This will allow moderate time resolution to be obtained for detectors such as Gas Čerenkov, Aerogel, TRD, and Lead Glass shower counters without additional discriminators or TDC modules.

Data Acquisition and Online Software

The philosophy of the data acquisition system for Hall C with the SHMS is that the DAQ should not be the limiting factor in the event rates that can be handled. Experience in Hall C has shown that factors other than DAQ, such as accidentals rates or singles rates on individual detectors, generally limit overall trigger rates to less than 10K events/second. With the front end TDC and ADC electronics discussed above, a DAQ system can be constructed that can handle event rates in excess of 10K/second with minimal deadtime. Other than the front end electronics, no technology advances are required in order to obtain these data rates. Future improvements in the speed and cost of networking, CPUs, and disk drives will only help to simplify the design of the DAQ system.

Data acquisition will continue to be managed by CODA[51]. CODA development over the next few years will include an emphasis on an on-line analysis farm as a part of CODA. With the upgrade we plan to add a moderate analysis farm. This will have two uses:

1. Real-time accumulation of diagnostic histograms
2. Data compression (background filtering, sparsification)

4.3.5.6 Stand-Alone (Third-Arm) Calorimeter

A large lead-glass calorimeter is planned to be used in experiments in Hall C with the present CEBAF 6-GeV machine. An approved experiment, GEP-III, will use the calorimeter to detect the scattered electron from the elastic $\vec{e}p$ reaction. This experiment will measure the ratio of proton electric to magnetic form factor at $Q^2 = 9$ GeV 2 by measuring the ratio of the transverse to longitudinal polarization of the outgoing proton in the elastic $\vec{e}p$ reaction. To cleanly identify elastic events, the scattered electron will be detected in a lead-glass calorimeter. This calorimeter is being constructed and is expected to be ready for the GEP-III experiment in 2005. The new calorimeter can be used in experiments to measure the ratio of proton electric and magnetic form factors at $Q^2 = 9\text{--}14$ GeV 2 , and to perform $\gamma\text{--}\pi^\circ$ production experiments. This new calorimeter is also planned to be used in real Compton scattering (RCS) experiments with 11-GeV beam energy which are extensions of experiments done with 6-GeV beam.

The calorimeter will consist of 1600-1700 lead-glass blocks. Two sizes of lead glass are used in the calorimeter. One set (which was used in the RCS experiment which ran in Hall A) has a frontal area 3.8x3.8 cm with length of 45 cm. The other set has a frontal area of 4.0x4.0 cm with length of 40 cm. The expected position resolution is 3-5 mm. The lead-glass calorimeter will have a frontal area of 2.7 m 2 and an aspect ratio of 2:1. The infrastructure for the calorimeter, such as platforms, cabling, and electronics, is planned to be usable for the experiments with 12-GeV beam. The electronics readout will be flexible. It will use active splitters for amplitude digitization of each channel and timing of the sums of 8 channels. The splitters will be designed to allow the full formation of a calorimeter trigger for experiments that need it, such as the RCS experiments.

Chapter 5

Ancillary Equipment

5.1 Beam Line

5.1.1 Overview

Beamline diagnostic systems will be unaffected by the upgrade, and the arc energy measurement should be making 0.1% measurements of the beam energy shortly after recommissioning. Solutions exist or will soon be implemented for all raster requirements at 12 GeV. However, systems based on large magnets, which were already pushing the envelope at 4-6 GeV maximum energy, will be severely impacted. In the case of the polarimeters, tight space limitations and high field requirements beg a superconducting solution. However, this would be prohibitively expensive. With cleverness and some sacrifice in capabilities, it should be possible to upgrade the polarimeters using relatively cheap resistive magnets.

In this chapter the nominal maximum beam energy in Hall C for the upgrade will be taken to be “12 GeV”.

5.1.2 Absolute Beam Energy Measurements at 12 GeV

The Hall C arc beam transport line has been used as a magnetic spectrometer to measure the beam energy between 0.5 GeV and 5.8 GeV. This is accomplished by temporarily retuning the arc optics from an achromatic mode to a dispersive mode. The arc consists of 8 dipole magnets run in series, each 3 m long. The absolute transverse positions and the incident angles of the beam at the entrance, middle, and exit of the arc are precisely measured by pairs of superharps (a wire scanner with absolute position readout). By adjusting the current of the magnet string, the beam trajectory is directed close to the centerline. The absolute beam energy is then simply related to the arc field integral (determined from a lookup table between magnet string current and field integral) plus modest corrections due to small angle and position deviations of the beam from the centerline. With an accurate survey of the arc bend angle, as well as an accurate lookup table, this technique routinely achieves its specified error of 0.1%. A cross-check using the presumably more accurate Hall A arc energy measurement finds a small systematic difference of only 0.05%.

In order for the arc dipoles to transport 12 GeV beam they must be converted from “C” to “H” style dipoles to reduce the amount of saturation at high energies. (Figure

5.1) Therefore, a complete rework, remap, reinstallion, resurvey, and recommissioning will be required prior to the restoration of absolute energy measurements with errors of 0.1%. No significant difficulty is anticipated for beam profile measurements (beam positions and orientations) at 12 GeV. Saturation effects appears to be less than 1%, so other than the need to cut off the field integrals slightly further from the magnet, there should be no problem recovering our usual accuracy for energy measurements of 0.1%.

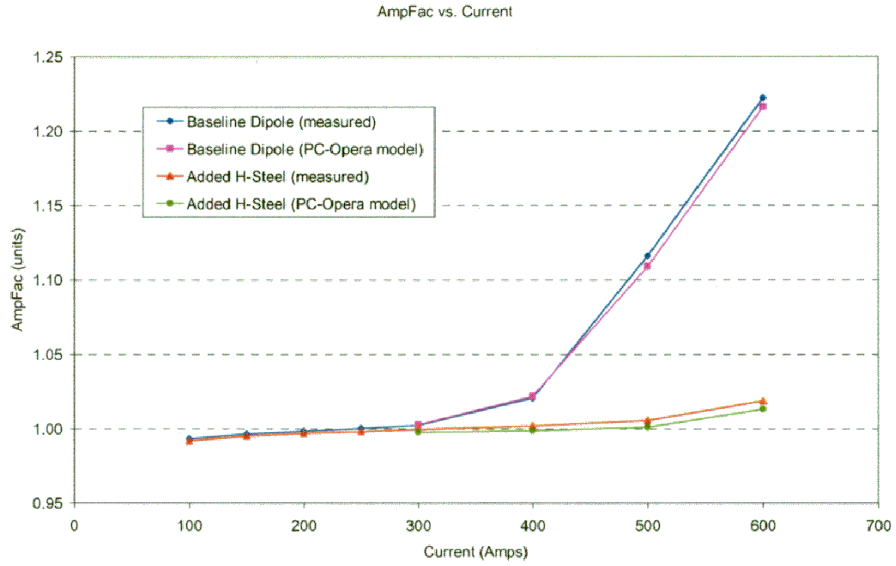


Figure 5.1: Renormalized Dipole Constant versus current for the existing “C” magnets (top two curves) and the reworked “H” magnets (bottom two curves). A momentum of 12 GeV/c corresponds roughly to 500A for “C” magnets. Saturation at 12 GeV/c in the “H” magnets will be less than 1%.

5.1.3 Beam Position and Current Monitoring at 12 GeV

Beam position measurements are usually made with stripline monitors which sense the beam’s microstructure. A limited number of resonant RF cavity beam position monitors, which have even greater position sensitivity than the stripline monitors, will be used in the G^0 and $Q_{weak}(proton)$ parity-violation experiments. Both types of instrumentation are based on RF techniques which are independent of the beam energy.

Resonant RF cavities are also used as a high bandwidth, high signal/noise relative monitors of the beam current. However, they must be calibrated using another device on the same beamline. For currents of $10 \mu\text{A}$ or higher, a wire-calibrated Unser monitor (an especially sensitive variety of Parametric Current Transformer) is used for absolute calibration. The Unser monitor is a null device which senses the DC magnetic field of the electron beam, independent of the energy of the beam. Due to the rather noisy output signal of the Unser monitor, the error of this calibration is limited to about 100 nA (rms) (ie, 1% at $10 \mu\text{A}$). At beam currents less than or equal to a few μA , the injector 5 MeV Faraday cup has been used to calibrate the RF beam current monitors in Hall C with an estimated 5% accuracy.

To summarize, all beam position and beam current measurements are completely transparent to the 12 GeV upgrade.

5.1.4 Beam Raster

Beam raster systems are used to limit the detrimental effects of localized beam heating in targets. These raster systems consist of air-core magnets driven by AC currents. The choice of location is often a compromise between wanting the largest deflection for the smallest field integral (ie, locating the raster magnets far upstream) and wanting to establish a raster pattern independent of the effects of focusing elements (ie, locating the raster magnets downstream of any quadrupoles). The raster R&D effort has been carried out by Chen Yan and consulting engineers. Raster technology developed for Hall C can be used in other Halls as well.

Three types of raster systems have been developed for Hall C:

Fast Raster

The so-called Fast Raster (FR) is used to minimize density changes in cryogenic targets. The frequency is rather high (about 20 KHz in both x and y), with a typical raster pattern used for experiments being a square of dimensions 2 mm x 2 mm. Adequate performance has been achieved using sinusoidal driving currents ($\leq 5\%$ density reduction at 100 μA), with most of the density changes occurring on the edges and corners of the pattern. The magnet driver for the Hall C FR system will be upgraded to produce a triangle waveform by the time the G^0 experiment begins running. (Figure 5.2) Not only will this produce a more uniform distribution with lower overall density changes, but the new driver has sufficient current to provide a 4.9 mm x 4.9 mm raster spot at 12 GeV/c beam momentum.

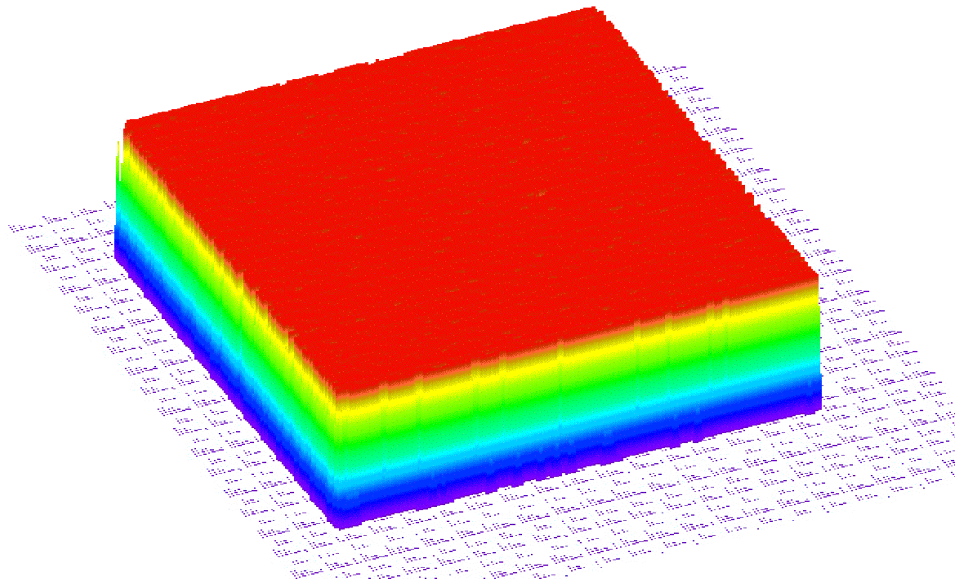


Figure 5.2: Uniformity of the New Fast Raster is shown in this plot of I_x versus I_y .

Slow Raster

The so-called Slow Raster (SR) is used to minimize depolarization in the UVA polarized proton or deuteron target. The pattern is a 2.5 cm diameter filled circle, redrawn at 1 Hz (synchronized to the helicity reversal). The present SR can provide a full-size raster pattern up to 6 GeV/c. Beginning 2003, a new SR system will be designed for 10-11 GeV/c operation.

Møller Raster

The Møller raster (MR) is used to minimize depolarization of electrons in the thin magnetized foil used in the Basel Møller Polarimeter. The raster pattern is a simple circle of 1 mm diameter redrawn at 100 Hz. This raster is already capable of operation at 12 GeV/c because the MR magnets are located far upstream, at the beginning of the 3C arc. The Møller polarimeter is located just beyond the end of the 3C arc. This is the only raster used in Hall C which has magnets located between the raster magnets and the raster target. Fortunately, the point-to-point focusing from the beginning to the end of the arc means the raster pattern is relatively unperturbed.

5.1.5 Møller Polarimeter

The Basel Møller polarimeter in Hall C is invaluable for its ability to make rapid and accurate (1%-level) measurements of the beam polarization. Invented by Ingo Sick and collaborators at the University of Basel, it is the most accurate electron beam polarimeter in the world, and represents a revolutionary leap forward in electron polarimetry. Without it, a Standard Model test such as the $Q_{weak}(proton)$ experiment could not be contemplated.

The polarimeter consists of a target and target solenoid, two quadrupole magnets, a collimator box and the detector system. The target solenoid is a superconducting magnet with a central field of 3 T directed parallel to the beam. It is used to polarize the valence electrons in a thin (10 μm) Iron foil perpendicular to the plane of the foil. The polarimeter is located at the beginning of the Hall C alcove.

Two resistive quadrupole magnets are used to keep the locations of the Møller target and detectors fixed regardless of the incident beam energy. Møller electrons are bent in the quadrupole fields and directed to the detector system which is positioned 11 m downstream of the target. Scattered electrons are detected in coincidence to exclude backgrounds from Mott scattering from Iron nuclei. The first quadrupole has an approximately 10 cm diameter bore and a physical length of about 30.5 cm. The second quadrupole is much larger, with a 25.4 cm diameter bore and physical length of 123 cm.

In its present configuration, the Basel polarimeter will operate to approximately 6 GeV/c. For operation at 12 GeV/c, either the magnet strengths or the drift lengths must double (or a bit of both). Since space must be reserved for a Compton polarimeter for the $Q_{weak}(proton)$ experiment, we will only consider upgrading the magnets. The second quadrupole will be most difficult to upgrade, since nearly everything about it is extreme: size, current draw, power consumption, cooling water pressure drop, and cooling water temperature increase. A superconducting replacement would cost millions of dollars.

The most likely upgrade scenario for the Basel Møller polarimeter is to retain the present quadrupole and power supply, and shim the pole tips. If the present aperture is decreased to 10 cm, then the increased gradient will allow operations over the range 6-12 GeV/c. (Figure 5.3) At the lower end of its energy range, the upgraded polarimeter will begin to lose scattered electrons in the shims due to the larger laboratory scattering angle for

Møller pairs. (All electron losses are accounted for in the Monte Carlo to obtain the correct acceptance-averaged analyzing power.) Therefore, below roughly 6 GeV/c, the shims would be swapped with a smaller set of shims which permit a larger aperture. The use of large shims may introduce significant non-quadrupole harmonics which have not yet been studied with TOSCA. In the worst case, the Basel polarimeter will operate up to 6 GeV/c, and polarimetry at higher energies would be carried out using the Compton polarimeter which is discussed in the next section.

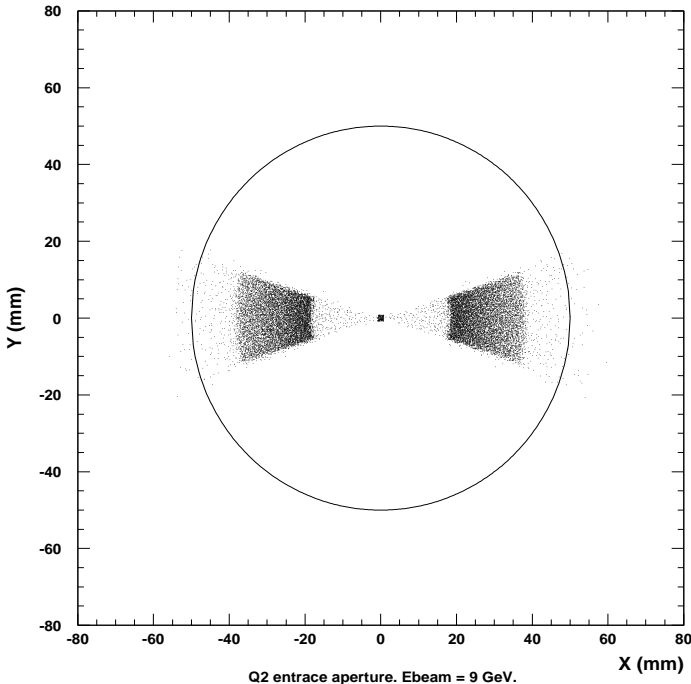


Figure 5.3: Scattered Electrons in the Møller Q2 Aperture for a Beam Energy of 9 GeV/c.

5.1.6 Compton Polarimeter

A Compton Polarimeter is required in order to continuously monitor relative polarization changes during the $Q_{weak}(proton)$ experiment in 2005-2006. Although that experiment will run at only 1.2 GeV, there is general agreement that the polarimeter should, if technically feasible, operate up to 6 GeV and be upgradeable to 12 GeV.

The most likely scenario for the first and second phases of the Compton polarimeter installation are the following:

- The Compton polarimeter will reside immediately downstream of the Møller polarimeter. It will operate at 1.2 GeV for the $Q_{weak}(proton)$ experiment, and its upper energy limit will be determined by present space constraints and the size of available resistive

magnets. To minimize expense and downtime, the existing beamline will be left intact as much as possible.

- For the 12 GeV upgrade, the Compton polarimeter length must be roughly doubled to avoid having to design and purchase superconducting magnets. This will necessitate a reconfiguration of the quadrupole triplet (on girders 3C18, 19, and 20) which focuses beam on the primary Hall C target. The primary target rasters may have to move further downstream.

5.1.7 Polarized Target Chicane

The UVa polarized target is operated with a substantial, fixed field integral of up to 1.53 Tesla-meters. Since the magnetic field axis is usually non-parallel to the beam direction, this is large enough to produce intolerable vertical deflections of a 4 GeV electron beam. Therefore, dipole magnets before and after the target are used to 1) steer the beam to the center of the target, and 2) direct the downstream beam to the dump. This “polarized target chicane” is an important item of existing Hall C infrastructure which it would be of great benefit to upgrade.

Beam transport through the existing Hall C chicane is tightly restricted due to the limited vertical apertures of the chicane magnets, their limited field integrals, and the beam pipe. Operationally, this means that the chicane must be surveyed and aligned whenever the target orientation changes, the beam energy changes, or when the target field is turned off for “straight-through” mode. These are time consuming operations which, when completed, require recommissioning of that section of the beamline. Given the potential high payoff and big investment in polarized target experiments, and the correspondingly smaller beam deflections at 12 GeV, it may be worthwhile and feasible to invest in a fixed, large aperture magnet system which does not require realignment.

Ideally, the existing system should be replaced with one that can:

- operate without need for realignment for a range of energies at the maximum standard target Bdl (~ 1.5 [T m] for 5.1 T at 90° to the beam).
- allow for polarity reversal of the target field for part of the above range.

For beam energies ≥ 6 GeV a fixed chicane with two upstream magnets centered at 9 m (bending down by $\theta = 2.2^\circ$) and 4.5 m (bending up by 2θ) from the center of the polarized target, a vertical aperture of 19 cm works, with a 1 cm clearance for a 1 cm radius rastered beam. This requires a beam pipe of ~ 6 ” diameter, to match the deflection at the entrance and exit of the second chicane magnet.¹ A tapered rectangular cross section pipe is an alternative that would accommodate both straight through (target off) and deflected beams. All apertures are proportionally reduced placing the chicane closer to the target. For comparison, the existing BZ1 magnet located 4.8 m from the target center is matched downstream to a 2.5” diameter circular beam pipe that cannot fit straight and deflected beams without adjustment.

For 11 GeV beams, the vertical deflection would be proportionally reduced to ~ 11 cm including raster and clearance. A vertical aperture of 30 cm for the second chicane magnet

¹If beam position measurements are required in this region, then new BPM’s such as large-stroke wire scanners must be developed.

would even allow for polarity reversal of the target field (first magnet bending up by 1.2°, second magnet bending down by 2.4°). The total aperture for polarity reversals increases up to \sim 38 cm at 6 GeV.

Without a downstream chicane, only one polarity (bending down) of the target would be possible below \sim 6 GeV, otherwise the deflected beam would end above the dump. For 6 GeV and above, a He filled beam pipe plus bag downstream of the target works well, especially since the polarized target operates with beam currents under 200 nA.

For energies below 6 GeV, experiment-specific reconfigurations of the system would still be required.

5.2 Target Systems and Infrastructure

5.2.1 Cryogenic Targets

The 12 GeV upgrade provides an excellent opportunity to improve the JLab high-power cryogenic target system for LH_2 , LD_2 , and cold Helium. While the original Hall C cryotarget cell design was largely based on targets built by John Marks for SLAC endstation A, JLab's much higher luminosity and throughput of experiments puts a premium on reliability and ease of alignment. Improvements to the motion mechanism, pumps, heat exchangers, and cells are desired. Fortunately, there is a critical mass of expertise at JLab to design the next generation of cryotargets.

One of the most visible design changes to the cryotarget system is to move the target cells vertically using components which reside completely inside vacuum. Connections for target gas and coolant will be made using stainless steel flex lines. This eliminates the need for the large bellows with its limited safe range of extension, and removes the nearly 1 ton of vacuum load that the lifter has to overcome. Lifter failure has been a frequent source of downtime in the existing design.

JLab cryotargets routinely operate at relatively high power (ie, 500 W or greater of beam power deposition). While the current target cells, heaters, pumps, and heat exchangers have proven adequate for this task, improvements on each of these components are desired. One focus for improvement is to remove the pump motor from the loop, thereby reducing the heat load to the target fluid and improving access to the motor in the event of failure. A second possibility is to use a centrifugal pump instead of the current axial type pump. Another is to develop a more efficient heat exchanger, principally by using a longer and more dense fin-tube. Some of these heat exchanger modifications have been tested satisfactorily under experimental conditions in Hall A. The goal of these design changes is to improve overall motor and pump efficiency, and increase the flow rate across the cell to reduce density changes due to beam heating. Many of these changes will be made to the existing Hall A and C cryotargets in an evolutionary manner even before the upgrade, while the $Q_{weak}(\text{proton})$ target may serve as a testbed for some of the more revolutionary changes.

The present target cell blocks and cells are attached with conflat style flanges. This allows for easy maintenance, flexibility in target setup (cell length changes of almost any size may be made in situ), and provides a nearly certain leak tight seal. When compared to soldered connections, these conflat style connections are clearly superior and will be an integral part

of the next-generation cryotarget design. Finally, there is hope that it will be possible to make the target cell entrance and exit windows from Beryllium in order to reduce window backgrounds. The current plan is to attach the Beryllium window to the aluminum tube. This technology exists and is employed in several thin windows currently used the Hall.

5.2.2 Solid Targets

It is natural for the solid target system to be integrated into the cryogenic target system: the solid “empty” target and optics alignment targets must be part of the cryotarget stack, and nearly every solid target experiment requires an LH_2 target for calibration. The solid targets can then be conductively (if expensively) cooled by the End Station Refrigerator via good thermal contact with the cryotarget stack. Unfortunately, the lack of vertical space between the beamline and the bottom of the present scattering chamber in Hall C means that the number, or vertical size, of solid targets has been strictly limited. Although there are several ways around this problem, experiments which require many solid targets have tended to rotate the cryotarget out of the beam, and employ a separate solid target ladder. This system has been an endless source of headaches (alignment, cooling, cryotarget rotation mechanism, and potential collisions between the cryotarget and the solid target ladder). The upgraded Hall C cryotarget would dispense with this separate solid target system, and create additional vertical space for solid targets by essentially creating a well in the bottom of the scattering chamber which fits into a newly machined cup in the top of the existing pivot. Rotation for the solid target ladder will still be available. This concept has been successfully used in Hall A since the beginning of operations.

5.2.3 Scattering chamber

A new scattering chamber is also needed to accommodate the full SHMS angle range. The scattering chamber will be constructed essentially as a heavy walled aluminum cylinder and have an outside diameter of \sim 60 inches. This is roughly 7 inches larger than the current chamber. It is assumed that all spectrometers will be in a horizontal plane. This allows for openings for each spectrometer to be \sim 8 inches high. The openings will be covered with thin aluminum windows. The properties of these windows are well known and should not pose any problems to the new design. A window opening that extends from -25° (beam left) to 90° (beam right) will accommodate both the HMS and SHMS full angular ranges. Most importantly this design limits the amount of material near the beam exit of the scattering chamber and allows for very small angles for both spectrometers ($< 5^\circ$). A second slot will be made from -45° (beam left) to -135° (beam right). The chamber will mount on the same flange on the pivot, however a small section of the pivot post will have to be bored out to receive the cup for the solid target ladder which extends below the cryotargets. The current design employs even larger arc sections for the spectrometer windows, therefore it is felt that the design will provide adequate structural strength.

5.2.4 Solid Polarized H and D Target

It has become evident that measuring both longitudinal and transverse asymmetries is a requirement in future spin physics studies. Solid polarized targets offer an attractive combination of both high luminosity and high radiation resistance for experiments requiring a nuclear spin-aligned target. The University of Virginia (UVA), along with the Polarized Target Group at Jefferson Lab, has installed and operated a solid polarized target in Hall C for three experiments to date.

The polarizing technique used is that of Dynamic Nuclear Polarization (DNP) [52]. The target material is placed in a strong, homogeneous magnetic field, and cooled to a temperature around 1K. At this temperature the energy of vibrations in the lattice is small compared to the splitting of the spin states of the nuclei due to the magnetic field. Microwave irradiation is then used to drive transitions in magnetic dopants that were introduced in the material prior to the experiment. As the spins of these dopants are flipped, hyperfine coupling to the spins of the nuclei can result in desired nuclear spin flips. The spin relaxation time of the dopants is typically on the order of microseconds, whereas that of the nuclei is on the order of minutes. As a result, the dopants relax back to their ground state and become available to couple to other, unflipped nuclei. This allows a low concentration of dopant to service the nuclei of an entire target sample. As the microwave irradiation continues, the polarization of the target sample builds until the rate of nuclear spin flips resulting from dopant transitions is balanced by the rate of nuclear relaxations back to the ground state.

The magnitude of polarization achievable is dependent on many factors – including the strength of the magnetic field, the temperature of the target material, and aspects of the microwaves used to drive the transitions – but is most dependent on the target material used and the details of its preparation.

Over three decades of research in the field have resulted in the development of a wide variety of suitable target materials. Those used in modern systems similar to the University of Virginia target typically yield proton polarizations greater than 90% and deuteron polarizations approaching 50%. In addition to the maximum achievable polarization, progress has been made in developing materials that are resistant to the damage caused by the experimental beam. Current materials can withstand on the order of 10^{17} particles per square centimeter before the cumulative radiation damage severely affects the polarization attained.

Upgrade of the CEBAF beam to 12 GeV will have little impact on the polarizing process discussed above, but some components in the Hall typically used with the target may need upgrading to continue to be of use in solid polarized target experiments.

The most important Hall system is the slow raster, which is used to distribute polarization-destroying radiation damage equally across the face of the target. A circular pattern is preferred in order to match the shape of the target cells, and a sweeping pattern that results in uniform charge per unit area is required. The maximum diameter needed is 2.5 cm, and the full pattern should be redrawn at a rate that is an integral multiple of the beam helicity flip rate. As discussed elsewhere in this document, such a system is under design.

The effects of the target magnetic field on spectrometer optics is another consideration. Event reconstruction is complicated by the fact that a) it is an extended target, 3 cm in length, b) the target field, which is typically non-parallel to the beam, bends the scattered particle before entry into the spectrometer, and c) the beam is rastered. Reconstruction is

therefore greatly aided by the use of an absolute beam position monitor near the target. A Secondary Emission Monitor, placed upstream of the target, was used for this purpose in past experiments.

Solid polarized targets are capable of operating at luminosities of $\sim 1 \times 10^{35}$ Hz cm $^{-2}$. This figure results from a combination of maximum beam currents ≤ 150 nA with effective target thicknesses of ~ 2.5 g/cm 2 for open geometry target magnet coils. The maximum currents are limited by the rate of polarization decay due to radiation damage, while the effective thicknesses are limited by the ~ 3 cm diameter of the uniform field region (required uniformity 1 part in 10^4) that can be obtained with split pair coil designs. For experimental setups that don't require open geometry coils, longer target cells in solenoidal fields can be used, with the target length limited only by the spectrometer acceptance.

5.2.5 Conceptual Design for a Polarized ${}^3\text{He}$ Target in Hall C

The study of polarization observables in processes such as meson electro-production is crucial for the extraction of the GPDs. A polarized ${}^3\text{He}$ target as an effective neutron target, would play a key role in any program to extract GPDs, which is one of the primary goals of the JLab 12 GeV energy upgrade [36]. We describe below the features of a polarized ${}^3\text{He}$ target for Hall C, which will have a thickness of $1.6 \times 10^{22}/\text{cm}^2$ and a polarization of 45 - 50 %.

The polarized ${}^3\text{He}$ target is based on the principle of spin exchange between optically pumped alkali-metal vapor and noble-gas nuclei[54]. The time evolution of the ${}^3\text{He}$ polarization can be calculated from a simple analysis of spin-exchange and ${}^3\text{He}$ nuclear relaxation rates [55]. Assuming the ${}^3\text{He}$ polarization $P_{{}^3\text{He}} = 0$ at $t = 0$,

$$P_{{}^3\text{He}}(t) = < P_{\text{Rb}} > \left(\frac{\gamma_{\text{SE}}}{\gamma_{\text{SE}} + \Gamma_R} \right) \left(1 - e^{-(\gamma_{\text{SE}} + \Gamma_R)t} \right), \quad (5.1)$$

where γ_{SE} is the spin-exchange rate per ${}^3\text{He}$ atom between the Rubidium (Rb) and ${}^3\text{He}$, Γ_R is the relaxation rate of the ${}^3\text{He}$ nuclear polarization through all channels other than spin exchange with Rb, and $< P_{\text{Rb}} >$ is the average polarization of a Rb atom. Our target will be designed to operate with $1/\gamma_{\text{SE}} = 6$ hours. The current target at Hall A has $1/\gamma_{\text{SE}} = 4$ hours. With the availability of high power laser diodes along with the ongoing and future efforts to study the the Rb polarization as a function of temperature, density and laser power we believe one can achieve $1/\gamma_{\text{SE}} = 6$ hours or better. Table 5.1 compares the parameters of this target with a current state-of-the-art target (E.g. the Hall A target).

A central feature of the target will be the sealed glass target cells, which will contain a ${}^3\text{He}$ pressure of about 15 atmospheres. As shown in Figure 5.4, the target cells will have two chambers, an upper chamber in which the spin exchange takes place, and a lower chamber, through which the electron beam will pass. In order to maintain the appropriate number density of alkali-metal (Rb) the upper chamber will be kept at a temperature of 170–200°C using an oven constructed of the high temperature plastic Torlon. With a density of 4×10^{20} atoms/cm 3 , and a cell length of 40 cm, the target thickness will be $1.6 \times 10^{22}/\text{cm}^2$.

In Hall A, the target cells have achieve $1/\Gamma_{\text{cell}}$ of 40-50 hours. We expect to construct and fill target cells of similar quality. These cells are constructed from aluminosilicate glass,

Parameters	Current Targets	New Target	Reason for Improvement
$1/\gamma_{SE}$ (hr)	4	6	Increased “usable” Laser Power ~ 100 W
Polarization (%)	40-45	45-50	improved $1/\gamma_{SE}$ systematic study of Rb polarization as a function of temperature and density
^3He density cm^{-3}	2.5×10^{20}	4.0×10^{20}	Higher ^3He pressure

Table 5.1: Comparison of Current State of the Art Targets with the Proposed Target

either Corning 1720 or GE 180. All tubing will be “resized.” This is a process in which the diameter of the tubing is enlarged by roughly a factor of 2 in order to ensure a smooth pristine glass surface that is free of chemical impurities. The cells will be baked at high temperature ($> 400^\circ \text{ C}$) for 4-7 days on a high vacuum system before filling. The Rb will be doubly distilled to minimize contaminants. The ^3He will be purified with a getter or liquid ^4He trap during filling. The cells will be filled to a high density of about 10 atm. ^3He by maintaining the cell at a temperature of about 20 K during the filling process. The length of the cell is 40 cm, and the diameter is 1.9 cm. The end windows are approximately 120 μm thick and the side walls are approximately 1 mm thick. The target is in an enclosure filled with helium. Helium gas was also used as cooling jets on the target windows to prevent electron beam overheating the target cell.

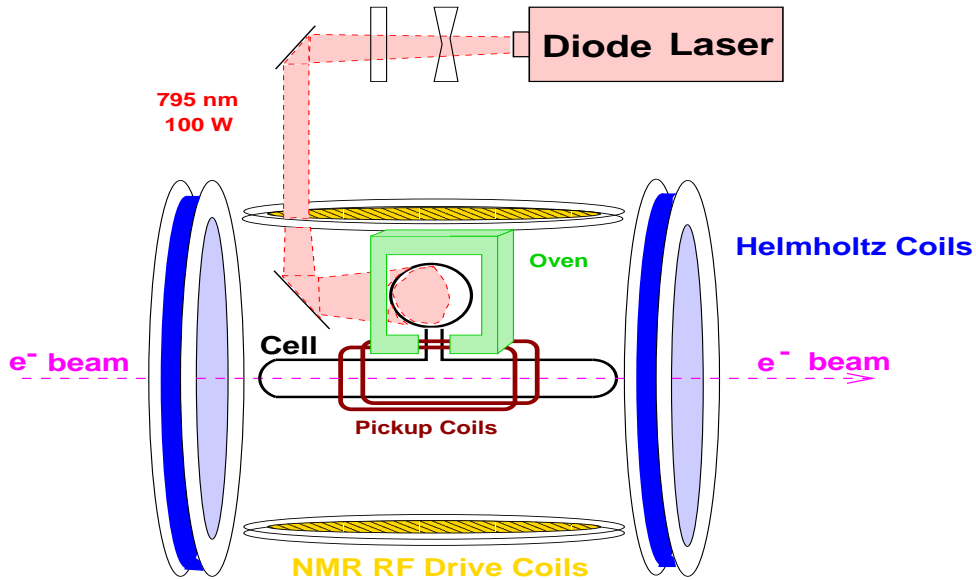


Figure 5.4: Schematic of the Spin-exchange Polarized ^3He Target. For clarity, only one set of Helmholtz coils is shown.

As mentioned above, approximately 100 Watts of “usable” light at 795 nm will be required. By “usable,” we essentially mean light that can be readily absorbed by the Rb. It

should be noted that the absorption line of the Rb will have a full width of several hundred GHz at the high pressures of ^3He at which the target will operate. Furthermore, since the target will operate with very high Rb number densities that are optically quite thick, quite a bit of light that is not within the absorption line-width is still absorbed. We can achieve this by using three 60 Watts diode lasers for the optical pumping in longitudinal directions and three diode lasers for pumping in the transverse direction. Recently even higher power diode-lasers have become available and it might be possible to achieve ~ 120 W of laser power from a single chip.

A beam of laser light coming out of the diode laser is unpolarized. A polarizing beam splitter can be used to linearly polarize the beam and then on passing it through a quarter wave plate, the laser light becomes circularly polarized. The circularly polarized laser light will be used to optically pump the Rb vapor in the pumping chamber to polarize the Rb atoms. These polarized Rb atoms then spin-exchange with ^3He gas to polarize the ^3He nuclei.

Polarimetry will be accomplished by two means. The polarization will be monitored using the NMR technique of adiabatic fast passage (AFP) [56]. The signals will be calibrated by comparing the ^3He NMR signal with that of water. The polarization will also be independently monitored by measuring the frequency shifts that the polarized ^3He nuclei cause on the electron paramagnetic resonance (EPR) lines of Rb atoms. Both methods were successfully used in Hall A in a number of experiments. Each method achieved a precision of 4% and two methods are in good agreement. The polarimeter can also be checked with a third (physics) method, by measuring the ^3He elastic asymmetry, since the ratio of the measure elastic asymmetry to the calculated elastic asymmetry (from the world elastic form factors) is proportional to the product of the beam and target polarization. However, such a method would only work at relatively low momentum transfer squared (Q^2).

The main components of the target include two pairs of large Helmholtz coils perpendicular to each other, which will be used to apply a static magnetic field of about 25 Gauss. In addition to establishing the quantization axis for the target, the coils are important for suppressing relaxation due to magnetic field inhomogeneities. The field direction can be rotated to any direction in the scattering plane. The NMR components in the target will include a set of RF driving coils, a separate set of pick-up coils, and appropriate electronics. The apparatus necessary for doing EPR polarimetry will include a small probe (housing a drive coil and a photodiode) and associated electronics. The polarimetry electronics will be controlled by a PC with LabView, which in turn will communicate with EPICS.

A target ladder will contain, in addition to the polarized ^3He cell, a reference cell. The reference cell is connected to a gas handling system and can be filled with different target gases (^3He , ^4He , N_2) at pressures range from 0 to 15 atmospheres. The target ladder can be moved into each target position, out of beam position and to the pick-up coil position.

An oven with hot air is used to heat up Rb to be in vapor state. It will be constructed from Torlon. The laser system will consist of 2-6 laser diode systems. There will also be several lenses, linear polarizers and quarter wave plates to circularly polarize the beam. The motion system control, the laser control, the oven and heater control and the temperature and pressure readout will all be done using the EPICS system.

5.2.6 General Hall Infrastructure

Existing Hall C infrastructure which can be applied to the upgrade includes AC power, Low Conductivity Water (LCW), high voltage and signal cables and their associated patch panels. There are 550 signal cables and 600 high voltage cables, all of which go to the second floor counting house. Approximately half of these will be available for the SHMS. There are approximately 100 Amps of “clean” power available for powering the SHMS detectors and 250 Amps of “dirty” power available in Hall C for powering potentially noisy motors, turbopumps, etc. The SHMS power supplies will require approximately 50 gallons per minute (GPM) of LCW which can easily be supplied using existing Hall C LCW.

In first approximation, the SHMS will require no upgrade to existing AC power, LCW, cables, or patch panels.

Bibliography

- [1] V.M. Braun A. Khodjamirian, M. Maul, Phys. Rev. D **61** (2000) 073004
- [2] O.C. Jacob and L.S. Kisslinger, Phys. Lett. **243B** (1990) 323
- [3] P.C. Tiemeijer and J.A. Tjon, Phys. Lett. **277B** (1992) 38
- [4] H. Ito, W.W. Buck, F. Gross, Phys. Lett. **287B** (1992) 23
- [5] P. Maris, P.C. Tandy, Phys. Rev. C **62** 055204
- [6] J. Volmer *et al.*, Phys. Rev. Lett. **86**, 1713 (2001)
- [7] W. Schweiger, Nucl Phys. Proc. Suppl. **108**, (2002) 242
- [8] J.P. Ralston and B. Pire, Phys. Rev. Lett. **61**, 1823 (1988); Phys. Rev Lett., **65** (1990), 2343
- [9] M.K. Jones *et al.*, Phys. Rev. Lett. **84** (2000) 1398; O. Gayou *et al.*, Phys. Rev. Lett. **88** (2002) 092301
- [10] S.S. Kamalov *et al.*, Phys. Rev. C **64** (2001) 032201
- [11] L. Tiator *et al.*, Submitted to European Physics Journal.
- [12] E. Bloom and F. Gilman, Phys. Rev. Lett. **25**, 1140 (1970)
- [13] I. Niculescu *et al.* Phys. Rev. Lett. **85**, 1182 (2000)
- [14] M. Arneodo *et al.*, Phys. Lett. **B364** (1995) 107
- [15] I. Niculescu, *et al.* Phys. Rev. Lett. **85**, 1186 (2000)
- [16] A. De Rujula, H. Georgi, and H.D. Politzer, Annals Phys. **103**, 315 (1977); A. De Rujula, H. Georgi, and H.D. Politzer, Phys. Lett. **64B**, 428 (1977)
- [17] D. Golgov, *et al.*, LHPC and TXL Collaborations, Phys. Rev. D **66**, 034506 (2002)
- [18] E.L. Berger, Proceedings, Workshop on Electronuclear Physics with Internal Targets, Stanford, CA (1987)
- [19] P.J. Mulders, hep-ph/0010199 (2000)

- [20] F.E. Close and N. Isgur, Phys. Lett. **509B**, 81 (2001)
- [21] A. Radyushkin, Phys. Lett. **380B**, 417 (1996); Phys. Rev. D **56**, 5524 (1997).
- [22] X. Ji, Phys. Rev. Lett. **78**, 610 (1997).
- [23] J. Collins, L. Frankfort, and M. Strikman, Phys. Rev. D **56**, 2982 (1997).
- [24] A. Radyushkin, Phys. Rev. D **58**, 114008 (1998).
- [25] A. Mukherjee et. al., Los Alamos preprint hep-ph/0205315
- [26] M. Burkardt, Phys. Rev. D **62**, 071503(R)(2000)
- [27] L.L. Frankfurt *et al.*, Phys. Rev. D **60**, 014010 (1999)
- [28] J. Arrington *et al.*, Phys. Rev. Lett. **82**, 2056 (1999)
- [29] X. Guo and J. Qiu, Phys. Rev. D **61**, 096003 (2000)
- [30] V.A. Dzuba, V.V. Flambaum and J.S.M. Ginges, hep-ph/0204134
- [31] G.P. Zeller *et al.*, (NuTeV Collaboration), Phys. Rev. Lett. **88** 091802 (2002)
- [32] Vector Fields Inc., 1700 N. Farnsworth Ave., Aurora, IL 60505
- [33] M. Berz, COSY INFINITY Version 7 Reference Manual, MSUCL-977 (1996), Michigan State University, East Lansing, MI 48824
- [34] D. Carey *et al.*, "Third Order TRANSPORT with MAD Input", Fermilab-Pub-98-310
- [35] N. Simicevic, "Design of a Čerenkov Counter for the Q-Weak Experiment", LATECH-CAPS-01-03A, March 12, 2001. Available in Public Access Papers area of <http://www.jlab.org/qweak/>.
- [36] "The Science Driving the 12 GeV Upgrade of CEBAF". Jefferson Lab, February 2001.
- [37] Particle Data Group, "Review of Particle Properties", Phys. Rev. D **66** (2002).
- [38] J. Arrington, Ph.D. thesis, California Institute of Technology, 1998.
- [39] W. Smythe, CEBAF Hall C SOS Cherenkov detector Handbook .(unpublished)
- [40] L. Sorrel, E155 Technical note 81. SLAC. 1999
- [41] Photonis Imaging Systems, www.photonis.com.
- [42] Lambda/Ten Optics, 7A Stuart Road, Chelmsford, MA 01824.
- [43] D. Beck *et al.*, G0 Experiment, (http://www.jlab.org/exp_prog/generated/apphal1c.html as viewed 26-JUN-2002)
- [44] V.L. Ginzburg and I.M. Frank, JETP **16** (1946) 15.

- [45] T. Ludlam *et al.*, Nucl. Instrum. Meth. **180** (1981) 413.
- [46] C. Fabjan *et al.*, Nucl. Instrum. Meth. **185** (1981) 119.
- [47] R. Mohring, Ph.D. thesis, University of Maryland, 1999.
- [48] L.Y. Zhu, Hall A data analysis workshop, Dec. 11-12, 2001.
 $(\text{http://www.jlab.org/}^{\sim}\text{lyzhu/work/dec01.ps.gz})$
- [49] D.W. Higinbotham, Nucl. Instrum. Meth. A **414** (1998) 332-339.
 $(\text{http://www.jlab.org/}^{\sim}\text{doug/cherenkov})$
- [50] G.Braun *et al.* “F1 - An Eight Channel Time-to-Digital Converter Chip for High Rate Experiments”, hep-ex/9911009.
- [51] JLab Data Acquisition Group, CODA, (<http://coda.jlab.org>)
- [52] A. Abragam and M. Goldman,”Principles of Dynamic Nuclear Polarization”, Rep. Prog. Phys. **41**, 395 (1978).
- [53] X. Ji, Phys. Rev. Lett. **78**, 610 (1997); Phys. Rev. D **55**, 7114 (1997); A.V. Radyushkin, Phys Lett, **B380**, 417 (1996); Phys. Rev. D **56**, 5524 (1997).
- [54] M. A. Bouchiat, T. R. Carver and C. M. Varnum, Phys. Rev. Lett. **5**, 373 (1960)
W. Happer *et al.*, Phys. Rev. A **29**, 3092(1984) P. L. Anthony *et al.*, Phys. Rev. Lett. **71**, 959(1993)
- [55] T.E. Chupp *et al.*, Phys. Rev. C **36**, 2244(1987) **A276**, 29(1989)
- [56] A. Abragam, *Principles of Nuclear Magnetism* (Oxford University Press, New York, 1961).

Appendix A

Detailed Cost Estimates

Appendix B

Project Timeline

Appendix C

List of Figures

2.1	The Magnetic Form Factor of the Nucleon-Delta Transition	4
2.2	Projections for Measurements of the π^+ Elastic Form Factor	7
2.3	Projections for Measurements of the $\gamma n \rightarrow \pi^- p$ Process at a Center-of-Mass Angle of 90°	8
2.4	Lowest Moments of the Structure Function Difference $\int_0^1 x^{n-2} (F_2^p - F_2^n) dx$	9
2.5	Phase Diagram for Nuclear Matter	11
2.6	The Running of $\sin^2 \theta_W$ Shown as a Function of Q	12
3.1	The π^+ Form Factor Including Recent Hall C Data	18
3.2	Scaled Cross Sections for $p(\gamma, \pi^+)n$ and $n(\gamma, \pi^-)p$	19
3.3	Existing and Approved JLab Measurements of $\mu G_{Ep}/G_{Mp}$	20
3.4	The Ratio of Electric Quadrupole to Magnetic Dipole Strength for the $p \rightarrow \Delta$ transition	21
3.5	Kinematic Regions Covered by Global Measurements of the Structure Function F_2	22
3.6	Projected Measurements of R and the Range in ϵ available for Rosenbluth Separations at $x = 0.8$	23
3.7	Duality Data from Hall C	24
3.8	Lowest Moments of the Structure Function Differences $\int_0^1 x^{n-2} (F_2^p - F_2^n) dx$ and $\int_0^1 x^{n-2} (g_1^p - g_1^n) dx$	26
3.9	Expected Uncertainties for an 11-GeV Measurement of $A_{ }$ in the $\vec{H}(\vec{e}, e')$ reaction at $Q^2 = 8$ (GeV/c) 2 in the nucleon resonance region.	27
3.10	Kinematic Coverage of the HMS-SHMS Combination for Meson Electroproduction	28
3.11	Deep Exclusive Scattering Processes that have been identified as providing a new window on the quark-gluon wavefunctions.	29
3.12	Projected measurements for wide angle Compton scattering as a function of $-t$, as compared to recent JLab data.	31
3.13	The Delta Resonance Transition Form Factor	32
3.14	The Projected Results for Target Asymmetry in the Process $en \rightarrow e' \pi^- p$ with a transversely polarized ${}^3\text{He}$ target	33

3.15 Transparency Data from BNL Compared to Recent and Projected Data from Hall C	34
3.16 An Example Measurement of Inclusive Electron Scattering from an Fe Target	35
3.17 The Phase Diagram for Nuclear Matter.	35
3.18 The Predicted Nuclear Transverse Momentum Broadening in Semi-Inclusive Pion Production.	37
3.19 The Running of $\sin^2 \theta_W$ Shown as a Function of Q^2	38
3.20 The Limits on C_{2u} and C_{2d} Listed by the Particle Data Group, SAMPLE, and the Proposed Experiment.	39
4.1 Sketch of the High Momentum Spectrometer	41
4.2 HMS Spectrometer Representative Data	42
4.3 Artist's Rendering of SHMS and HMS Spectrometers	45
4.4 SHMS Spectrometer Key Dimensions	46
4.5 Q1 Gradient Comparison along Z.	47
4.6 Magnetic Fields in Q1 at High Current.	48
4.7 Cut-Away View of QD30 Magnet	48
4.8 Magnetic Field Magnitude in QD30 Midplane	50
4.9 QD30 Yoke Saturation	51
4.10 QD30 B_y and Integral Field	51
4.11 QD30 Integral B_x/y	52
4.12 SHMS Pivot with Slider.	53
4.13 SHMS at 5 degrees. HMS at 10.5 degrees.	54
4.14 SHMS at 25 degrees. HMS at 10.5 degrees.	54
4.15 Hall C Pivot with SOS, SHMS, and HMS Attached	55
4.16 Track of Central Ray through Transition Spool	59
4.17 Rays Tracked through the SHMS by COSY for the SSA Tune	60
4.18 Polynomial Coefficients in the QD Magnetic Field Model	62
4.19 Rays Tracked through the SHMS by COSY for the LSA Tune	64
4.20 The Phase Space Acceptance for the LSA and SSA Tunes	67
4.21 Y_{tar} Acceptance	68
4.22 Particle Hit Density at $z = 0$ for Various Target Lengths	68
4.23 Particle Hit Density at Detector Locations for the SSA Tune	69
4.24 Particle Hit Density at Detector Locations for the LSA Tune	69
4.25 Resolutions at the Target vs. δ for the LSA Tune	70
4.26 Resolutions at the Target vs. δ for the SSA Tune	71
4.27 Block Diagram of SHMS Detector Arrangement.	73
4.28 Measured Residual Distributions in the SOS Wire Chambers	74
4.29 Block diagram of the SHMS Wire Chamber Assembly	75
4.30 Pion/Kaon Discrimination from dE/dx	75
4.31 Time of Flight Relative to Electrons vs. Momentum	76
4.32 Placement of the Scintillator and Čerenkov Hodoscopes	77
4.33 Summary of the SHMS Particle Identification Resolving Power	80
4.34 Linearity and Resolution of a Lead Glass Calorimeter	81
4.35 Electron – Pion Discrimination Power of a Lead Glass Calorimeter	82

4.36 Momentum Dependence of the Čerenkov Light Production Rate	83
4.37 Pressure and Photoelectron Yield for the C ₄ F ₁₀ Čerenkov	84
4.38 Schematic Design for the SHMS Heavy Gas Čerenkov Detector.	85
4.39 Pion Efficiency of TRDs as a Function of the Detector Length	87
4.40 TRD Module and Output Signals	87
4.41 Hadron Velocity $1 - \beta$ as a Function of Momentum	89
4.42 SHMS Detector Package using the Focal Plane Polarimeter	90
5.1 Renormalized Dipole Constants for the Existing and Upgraded Arc Dipoles .	94
5.2 Uniformity of the New Fast Raster: I_x versus I_y	95
5.3 Scattered Electrons in the Møller Q2 Aperture at 9 GeV/c	97
5.4 Schematic of the Spin-exchange Polarized ³ He Target	103

Appendix D

List of Tables

2.1	The Hall C Experimental Program at 12 GeV and the Associated Apparatus Requirements.	14
4.1	Summary of the HMS Performance	43
4.2	Q1 comparison between HMS at 1010 amps and SHMS at 1291 amps.	47
4.3	SHMS QD30 Magnet Parameters	50
4.4	Design Specifications for the SHMS	58
4.5	SHMS Optics Parameters for SSA and LSA Tunes	63
4.6	Sensitive Areas of the Detectors	73
4.7	Nominal Dimensions of the Hodoscope Elements	78
5.1	Comparison of Current State of the Art Targets with the Proposed Target	103

Appendix E

Projected Physics Results (available in Internal Report Only)